LBL-30170

Center for Advanced Materials

CAM

Cryogenic Mechanical Behavior of Vintage III Aluminum-Copper-Lithium Alloy 2090-T81

D. Chu
(M.S. Thesis)

December 1990

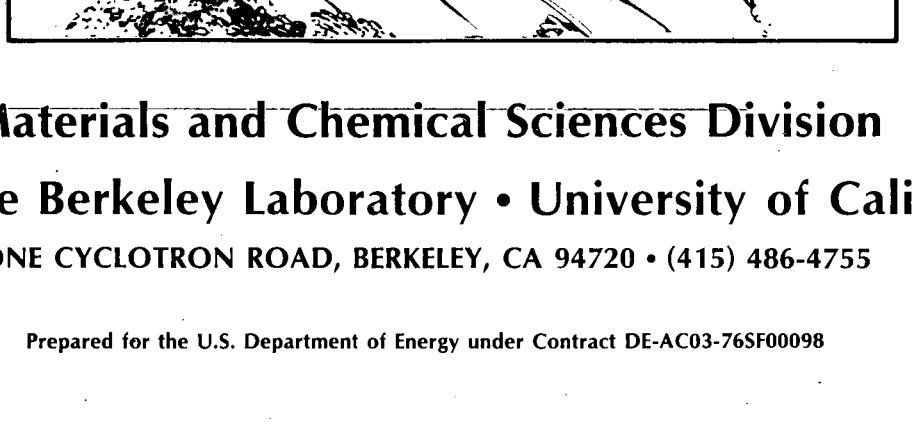

Materials and Chemical Sciences Division

Lawrence Berkeley Laboratory • University of California

ONE CYCLOTRON ROAD, BERKELEY, CA 94720 • (415) 486-4755

Prepared for the U.S. Department of Energy under Contract DE-AC03-76SF00098

DISCLAIMER

LBL30170

Cryogenic Mechanical Behavior of Vintage III Aluminum-Copper-Lithium Alloy 2090-T81

David Chu

Department of Materials Science and Mineral Engineering
University of California

and

Center for Advanced Materials
Materials Sciences Division
Lawrence Berkeley Laboratory
University of California
Berkeley, CA 94720

December 1990

This work was supported by the Director, Office of Energy Research, Office of Basic Energy Science, Materials Sciences Division of the U. S. Department of Energy under Contract No. *DE-AC03-76SF00098.*

Cryogenic Mechanical Behavior of Vintage III Aluminum-Copper-Lithium Alloy 2090-T81

David Chu

Master's Thesis

Abstract

The cryogenic mechanical properties of a 12.7 mm (0.5 in.) Vintage III 2090-T81 (Al-3.05Cu-2.16Li-0.11Zr in weight percent) plate material are studied. The results indicate that the through-thickness and in-plane anisotropies in the yield strength of Vintage I 2090-T81 are reduced in the Vintage III material by utilizing a partial recrystallization step during the thermomechanical processing, but at some cost to the elongation and cryogenic fracture toughness. Sharp discontinuities in the microstructure resulting from this thermomechanical treatment give rise to distinct differences in the variation of the work hardening behavior with temperature between those regions that undergo recrystallization and those that do not. In-plane properties are also affected by the wide variation in grain structure; the fully unrecrystallized region exhibit greater in-plane anisotropy than the pre-recrystallized region.

The lower elongations relative to Vintage I 2090-T81 observed in Vintage III 2090-T81 result from a decrease in work hardenability that appears to be associated with increased slip heterogeneity. The reduced cryogenic toughness is due in part to the disruption of the monolithic unrecrystallized grain structure previously observed in Vintage I 2090-T81. The results suggest that a fully unrecrystallized structure is essential for excellent cryogenic toughness.

Table of Contents

List of Figures

Introduction

Aluminum based alloys containing lithium are attractive structural materials due to their low density and high stiffness and strength relative to current high strength aluminum alloys.[1,2] Applications for these alloys were realized early in the aircraft industry where design studies have shown that reductions in weight density provide the most efficient means of increasing both weight savings and aircraft performance.[3,4,5] In general, a 3% reduction in density and a 5 to 6% increase in the modulus are associated with each weight percent addition of lithium (Figure 1).[6,7] As part of a continuing effort to develop these alloys, an aluminum-copper-lithium alloy designated 2090 was introduced by the Aluminum Company of America (Alcoa).[8] This alloy in the stretched and peak aged condition (-T81) is intended to replace the heavier aluminum-zinc alloy, 7075-T6, that is now used in commercial and military aircraft. Consequently, early alloy development efforts set out to match 2090-T81 coupon properties with those of 7075-T6. Under the auspices of a Navy cooperative test program, Alcoa contracted a number of aerospace firms and government agencies to test and evaluate the new alloy. During this period, work showed that 2090 also has an excellent combination of strength and toughness at cryogenic temperatures.[9-14] As a result, 2090-T81 and alternative aluminum-lithium alloys are projected to replace the aluminum alloy 2219-T87 that is currently used in cryogenic applications.[10,15] Several investigations are presently underway to assess the use of 2090 as a structural material for both aircraft and aerospace systems;[6] in particular, for applications such as fuselage skins, stringers, frames, and welded cryogenic tankage.[6,16]

Despite its initial promise, studies on 2090-T81 have revealed a number of problems. The one which has received the most critical attention is yield strength anisotropy.[17-20] This problem is directly related to the particular thermomechanical treatment used to produce the final product. The process is a proprietary one that includes a thermomechanical reduction into plate form, a solution heat treatment, a subsequent 6 to 8% stretch, and a final peak-age at 163°C for approximately 24 hours.[15] Initially designed to produce a high strength, fully unrecrystallized microstructure, the process results in a material which is highly textured and contains highly elongated grains.[8,9,12-15] This microstructural anisotropy can be seen in the optical micrograph of the 12.7 mm (0.5 in.) 2090-T81 plate shown in Figure 2 where the elongated grains result in a laminate-like morphology. As a consequence of this microstructural anisotropy, the tensile properties of the alloy tend to vary both in the plane and through the thickness.[17-20] The latter is defined by a variation in mechanical properties through the thickness of the final product form while in-plane anisotropy concerns such variations associated with the direction relative to the rolling direction of the plate at which the tests are performed. The processing of the commercial plate has been modified to minimize this anisotropy, leading to a new version of the plate that is designated "Vintage III" to differentiate it from the earlier material ("Vintage I").[20,21] The anisotropy and cryogenic properties of an example Vintage III plate are the primary subject of this work.

The yield strength of the first production 2090-T81 12.7 mm (0.5 in.) plate material (Vintage I) follows a parabolic profile through the thickness of the sheet with a maximum value near mid-thickness.[8,17,18,20,21] Differences of approximately 120 MPa (17 ksi)

between tensile samples tested at mid-thickness and tenth-thickness have been reported.[8] Vasudévan, et al.[17,18] attribute the change in yield strength primarily to the variation of the crystallographic texture induced by non-uniform rolling during processing. A plot of ODF (orientation distribution function) peak intensity of the Brass texture components versus through-thickness position shown in Figure 3 reveals a parallel relationship between the yield strength and the Brass hot-rolling texture component.[17] The strengthening phase T_1 (Al_2CuLi) has also been shown to play an important role in the through-thickness yield strength variation.[17,18] Other microstructural features including grain shape, lithium and copper in solid solution, and non-uniform quench rates are also cited as possible mechanisms.[17]

In addition to the through-thickness anisotropy, a drop in strength and subsequent increase in elongation are observed for off-axis tensile loadings (Figure 4).[8,16,19-21] The strong hot-rolled texture of Vintage I 2090-T81[19] and other aluminum-lithium alloys[22,23] has also been cited as the indirect cause of this in-plane anisotropy. Kim and Lee[19] propose that due to the strong brass component of the material, the subsequent stretch of the material produces a larger proportion of dislocations along those {111} slip planes which are favorably oriented to the stretch direction. Since T_1 nucleates heterogeneously as a platelet along {111} planes, a non-uniform distribution of these precipitates with respect to the four {111} variants results. The subsequent alignment of the favored slip planes containing the larger proportion of T_1 phase then dictates the dependence of subsequent deformation behavior with specimen orientation.

The anisotropic features discussed above are accompanied by an additional problem of poor short-transverse properties.[8,11,15,16] This problem can be best noted by the material's tendency to delaminate along the large planar grain boundaries normal to the short-transverse direction.[11,13-15,24] This phenomenon and its corresponding effect on the toughness of the material, particularly at cryogenic temperatures, has been studied at great length.[13-15,25,26] Venkateswara Rao, Ritchie, and coworkers[13,14] assert that the intergranular cracks perpendicular to the crack front and crack plane increase the fracture toughness by partially relaxing the stress triaxiality induced by an inherent plane strain condition. At 77K, the increase in the degree of splitting over that observed at 300K leads to a higher fracture toughness. Others claim that the improved work hardening behavior at cryogenic temperatures is more dominant in dictating the subsequent fracture toughness,[12,15,23] contesting that the effect of delamination is minimal compared to the magnitude of the toughness increase.[15] Low melting point impurity phases are also cited as possible sources for the fracture toughness increase.[27,28] No matter which answer reigns true, the engineering implications of delamination are still undesirable.

In response to the problems of anisotropy and delamination, Alcoa introduced the new modification of the alloy 2090 that is referred to as Vintage III 2090-T81.[20,21] This new vintage is projected to alleviate the problems of anisotropy and delamination associated with the earlier vintage. The main purpose of this study is to develop an understanding of the relationship between the microstructure, mechanical properties, and mechanical behavior of Vintage III 2090-T81.

Since the two vintages of 2090 have similar nominal compositions, any improvement in the mechanical isotropy of the alloys must be primarily due to changes in microstructure. As a precipitation hardened alloy, the microstructure of 2090-T81 can be considered on two levels: the intragranular structure and the intergranular or polygranular structure. The polygranular structure includes the distribution and orientation of grains: the grain size, shape, and crystallographic texture, whereas the intragranular microstructure includes the nature, size and distribution of the various precipitates present, and the initial dislocation structure. The polygranular structure is primarily determined by the thermomechanical processing the alloy has received, including ingot casting, homogenization and rolling. In contrast, the intragranular structure is determined by the final heat treatment: quench rate, aging temperature and aging time. The subsequent precipitate distribution of 2090 and other aluminum-lithium alloys has been studied extensively and is summarized in a number of articles within the proceedings of five international conferences.[29-33] Table I lists those precipitates which figure most prominently for 2090.

Since 2090 obtains its strength from precipitation hardening, its mechanical properties are correspondingly contingent on the precipitate phases present which themselves are synergistically linked to each other (i.e. an increase in T_1 volume fraction results in a decrease in the δ' volume fraction). Subsequently, the ability of the precipitates to improve the alloy's properties is directly dependent on the aging treatment.[8] Specifically for 2090-T81, this amounts to the aging time, aging temperature, and amount of stretch prior to aging. Previous work on 2090 and other aluminum-lithium alloys have, for the most part, optimized these parameters to prevent overaging and guarantee a homogeneous and effective distribution of precipitates, in addition to avoiding the nucleation of undesired equilibrium and other miscellaneous phases such as δ (AlLi), T_2 (Al_5CuLi_3) and θ'(Al_2Cu).[2,3,8,20,26-30] Any further significant improvement must therefore involve the thermomechanical processing of the material prior to aging. Modifications of this type directly affect the polygranular structure of the material. Changes in the hot-rolling parameters (rolling temperature, rolling speed, and percent reduction per pass) can lead to a large range of different grain structures and crystallographic textures.[23]

In lieu of the above discussion, it is not surprising that the differences between Vintage I and Vintage III 2090-T81 lie predominantly among the intergranular or polygranular features. This work strives to develop an understanding of the effects incurred by the modification of these features in the microstructure of the Vintage III 2090-T81 alloy and how these modified features affect the material's cryogenic properties and anisotropic behavior.

Experimental Procedure

The material investigated in this study was a Vintage III 2090 plate that was provided by Alcoa in the form of a 12.7 mm (0.5 in.) plate in the -T81 condition, solution heat treated, stretched and peak-aged. This temper is also referred to as -T8E41 in earlier publications. The nominal composition ranges for 2090 in weight percent are tabulated in Table II. Actual compositions for both Vintage I[9,12,15] and Vintage III materials were determined by atomic absorption spectroscopy and are also shown in Table II.

The as-received microstructure was examined by optical and transmission electron microscopy (TEM). Optical samples were polished to 0.05 μm and etched using Keller's reagent (2.5% HNO_3, 1.5% HCl, 0.5% HF (40%), balance H_2O) for approximately 30 seconds. TEM samples were prepared by mechanically grinding to 0.25 mm (0.010 in.) and punching 3 mm disks. The discs were electropolished at 18-20 volts with the double jet technique at -30°C in a 4:1 mixture of methanol and nitric acid.

Mechanical tests were done at one of four temperatures; 300K (room temperature), 200K (dry ice and alcohol), 77K (liquid nitrogen), and 4K (liquid helium). Tests were performed in servo-hydraulic testing machines equipped for cryogenic testing. Flat tensile specimens were used so that the various microstructures through the plate thickness could be tested individually. To characterize the through-thickness anisotropy of the material, tensile test specimens were cut parallel to the rolling direction (longitudinal) at five levels, as illustrated in Figure 5: mid-thickness (T/2), quarter-thickness, top and bottom (T/4 and 3T/4), and tenth-thickness, top and bottom (T/10 and 9T/10). Characterization of the in-plane anisotropy was accomplished by extending the test matrix to include additional off-axis tensile test specimens: 45° from the rolling direction at each of the five levels, and perpendicular to the rolling direction (long-transverse) at mid-thickness and both quarter-thickness positions. Figure 6 shows a schematic of the position and orientation of the off-axis tensile specimens relative to the original plate material. All sides of the tensile specimen gage were polished to 600 grit prior to testing to minimize any effect from notch sensitivity. Selected samples were polished further to 0.05 μm to facilitate the observation of slip relief patterns on the surface after testing. Additional information on the through-thickness anisotropy was obtained by means of microhardness samples machined every 1.27 mm (0.05 in.) from the top surface to the bottom surface and tested using a 50 gram load.

All tensile tests were conducted in displacement control. This was chosen over strain control to avoid jumps in the displacement upon splitting and subsequent stress relaxation. Displacement rates corresponded to strain rates of approximately 2.5×10^{-4} per second within the plastic range. Specimen elongation was monitored by placing a strain gauge along the gage length. Engineering stress and strain data was collected via computer and reduced prior to further computation. The data were then converted to true stress (σ) and strain (ε) values. The instantaneous strain hardening rate, $\partial\sigma/\partial\varepsilon$, was calculated by means of a sliding five-point fit to the parabolic relation $\sigma = A\varepsilon^n$, where A is the stress at unit strain and n is the strain hardening exponent which varies with the amount of deformation.[34,35] The raw data collected from tensile specimens tested at 4K were smoothed prior to the strain hardening calculation in order to reduce the scatter resulting

from the serrated yielding behavior associated with adiabatic heating of the specimen.[36] The analysis of the tensile tests include comparisons of the values of true stress, true strain, and strain hardening rate and their relationships to one another under the various test conditions. Strain hardening curves are presented in two forms; as a function of true stress and true strain. Both types of plots are compared, respectively, with one another. Systematic trends in the strain hardening rate with the various testing conditions are investigated.

Overlay plots of the true stress, σ, and strain hardening rate, $\partial\sigma/\partial\varepsilon$, as a function of the true strain, ε, illustrate the stability of plastic deformation and the relative ductility at failure. Such plots were used by Glazer, et al.[12,15] to study the macroscopic tensile behavior of 2090 and 2091. Geometric instability in tension occurs when the strain hardening rate equals the true stress ($\partial\sigma/\partial\varepsilon = \sigma$).[37] Upon the satisfaction of this relation, the increase in stress due to the decrease in cross-sectional area exceeds that due to work hardening. Deformation is then no longer stable and necking begins. The difference, $\partial\sigma/\partial\varepsilon - \sigma$, is a measure of the instantaneous stability of plastic deformation. The value of the difference at failure can be used to distinguish between cases of premature or brittle fracture ($\partial\sigma/\partial\varepsilon > \sigma$) and failure due to the macroscopic geometric instability ($\partial\sigma/\partial\varepsilon \leq \sigma$).

Since strain is a not a thermodynamic variable and cannot be used to describe the state of a given material, it is common to plot the work hardening rate, $\partial\sigma/\partial\varepsilon$, versus the true stress, σ, rather than the true strain, ε. Simple theories relate the product $\sigma(\partial\sigma/\partial\varepsilon)$ to the inverse of the dislocation mean free path and the true stress, σ, to the dislocation density.[38] Such plots are utilized to separate and identify the effect of temperature on the microscopic development of work hardening for tensile specimens under various testing conditions. Plots of this form, shown in Figure 7, exhibit a line of zero slope in the idealized case, where the increase in dislocation density is compensated by a corresponding decrease in the dislocation mean free path. In this study, the line of zero slope is referred to as the region of stable deformation and is defined by the two inflections which border it. Deviations from this plateau represent increased localization of slip within the material.

The fracture toughness of the Vintage III 2090-T81 plate was measured by determining K_{Ic} values from measured J_{Ic} values for standard 12.7 mm (0.5 in.) thick compact tension specimens with W = 50.8 mm (2.0 in.) according to the 1987 ASTM Standard E813, using the single specimen compliance technique. The specimen is illustrated in Figure 8. J_{Ic} tests were selected since it was not possible to perform valid K_{Ic} tests in all cases and to allow the direct comparison of toughness values obtained from research work on the earlier vintage.[12-15] Tests were conducted for three orientations (L-T, T-L, L-45°), as depicted in Figure 9, each at three different test temperatures (300K, 77K, 4K) so as to correspond to tensile data. A study of the extent of secondary splits perpendicular to the crack plane was also conducted by sectioning L-T J_{Ic} specimens within a few millimeters of the fatigue precrack perpendicular to both the crack plane and crack propagation direction. The resulting profile was then polished and etched in the same manner as optical samples to reveal the fracture surface profile and the splits that extended into the specimen. Fracture surfaces of both tensile and compact tension specimens were examined by scanning electron microscopy. This analysis also served as an additional means to obtain grain morphology data.

Experimental Results: Microstructure

The grain structures of both Vintage I and Vintage III 2090-T81 are shown in Figure 10. Two things to note are the larger grain size associated with the more recent vintage and the large grain size variation with respect to the position within the plate. The grains in the earlier vintage are highly elongated with a mean grain size of approximately 2000 x 400 x 25 μm throughout the material.[15] In contrast, the grain size in Vintage III 2090-T81 ranges from approximately 3500 x 800 x 50 μm at mid-thickness to as great as 10000 x 800 x 300 μm at quarter-thickness.

A more in-depth optical survey reveals that this trend of increasing grain size is not monotonic. Figure 11 shows the microstructure through a series of optical micrographs which incorporates the top portion of the plate material, mid-thickness to the surface. The wide range of grain sizes observed is also accompanied by a wide range of grain morphologies. Relatively thin grains with a healthy distribution of subgrains are found at mid-thickness of the plate whereas a region consisting of much larger grains with very few subgrain features is observed near quarter-thickness. The transition between the two grain morphologies is abrupt as highlighted in Figure 12. The discrete change suggests that the material was partially recrystallized at some point during the thermomechanical processing. Toward the surface, a slight decrease in grain size and a return of subgrain features is noted. In contrast to the elongated grains expected in a hot-rolled material, the grains at the surface are equiaxed with an average diameter of approximately 500 to 1000 μm. The inability to resolve these grains in the other two planes indicates that this layer is relatively thin. The increased contrast obtained from these grains relative to the rest of the plate suggests that this equiaxed layer may be the result of surface recrystallization upon the final solution heat treatment.[39]

Despite the wide range of microstructures observed, little to no differences were found in the distribution of strengthening precipitates. TEM micrographs taken at mid-thickness and both quarter-thickness positions, shown in Figure 13, reveal a homogeneous distributions of both δ' and T_1 at both positions. No embrittling δ precipitate phase was observed in the bright field images of selected samples. Thorne et al.[40] have reported a lithium depletion zone induced by the surface recrystallization discussed above. However, a TEM investigation at the surface revealed no significant decrease in the volume fraction of δ' or T_1.

Experimental Results: Mechanical Properties

Tensile Properties

Tensile properties measured from Vintage III 2090-T81 longitudinal, 45°, and long-transverse tensile specimens are summarized in Tables III through V, respectively. Corresponding plots of the measured tensile properties versus position and temperature are shown in Figures 14 through 16. Values obtained by Glazer et al.[15] for Vintage I 2090-T81, 7075-T6 and 2219-T87 in the longitudinal orientation are tabulated in Table VI for comparison. For the majority of Vintage III 2090-T81 tensile specimens, the reduction in the cross-sectional area was minimal. A few exceptions to this trend occurred for tensile specimens taken at 3T/4 and 9T/10 where the combination of intergranular delamination and partial fracture produced large area reductions within the material still intact and, subsequently, exaggerated total elongations. Uniform elongations remained unperturbed by this behavior and remained valid parameters for comparison.

Strength and uniform elongation values measured for Vintage III 2090-T81 at mid-thickness in the longitudinal orientation increase with decreasing temperature. This trend is similar to what is observed for the earlier vintage as shown in Figure 17. Although the level of the temperature induced strength increase is lower for the Vintage III material, the degree of the strength increase is similar. The improvement trend of the uniform elongation measured for Vintage III 2090-T81 at mid-thickness parallel that exhibited by its predecessor except at 4K where Vintage I 2090 exhibits roughly twice the elongation of Vintage III 2090. The dual drop in both strength and elongation observed in the Vintage III material relative to the Vintage I material is unusual; an inverse relation between the two is more common.

The strengths and uniform elongations measured for longitudinal tensile specimens taken at T/4 and 3T/4 plate positions increase with decreasing temperatures, similar to that observed for mid-thickness specimens of the same orientation. Figure 18 shows that this increase occurs, however, at a much lower strength level. The strengths at both quarter-thickness positions are approximately 15% lower than those at mid-thickness at all temperatures. Drops of this magnitude have also been observed for Vintage I 2090-T81.[8,9,12,15,17,18,20,21] In addition, an asymmetry of mechanical properties can be noted. T/4 specimens exhibit a large jump in uniform elongation between 300K and 200K whereas a similar jump does not occur for 3T/4 specimens until lower temperatures (Figure 18c). The elongation values for both quarter-thickness specimens at 300K are extremely low, ranging from 1 to 3%. Composite plots of σ and $\partial\sigma/\partial\varepsilon$ versus ε, which will be shown and discussed later, reveal that this drop in elongation occurs due to the absence of a region of stable deformation. Overall, lower values of strength and elongation are measured for Vintage III 2090-T81 tensile specimens when compared to Vintage I 2090-T81 at the corresponding position and orientation (Tables III and VI).

Strength increases observed for longitudinal specimens taken at T/10 and 9T/10 with decreasing temperature parallel those observed for specimens taken at the quarter-thickness positions immediately adjacent (Figure 19). In particular, a stall in the increase of strength between 300K and 77K can be seen at T/10, similar to that observed for T/4

tensile specimens. In contrast, the elongation data increases only between 300K and 200K prior to a drop at 4K and 77K for T/10 and 9T/10 tensile specimens respectively. This pattern is indicative of a ductile to brittle transition, as confirmed by work hardening plots. Analysis of the fracture surface, however, suggests that the transition occurs only within the region of material containing equiaxed grains directly below both surfaces. This observation will be discussed later in more detail.

A secondary check of the through-thickness yield strength anisotropy was performed by means of microhardness measurements, the results of which are plotted in Figure 20. A good correlation is observed between measured hardness values and measured tensile strengths (Figure 14): the drop in the yield strength near quarter-thickness corresponds to a similar drop in the measured microhardness values. Microhardness values also reveal that the center of symmetry of mechanical properties does not coincide with the geometric center of the plate. The shift of the center of symmetry away from the geometric center is approximately 1.0 to 1.5 mm (0.05 in.) toward the bottom of the plate. Hardness measurements performed on the equiaxed grains residing on both surfaces are considerably lower than those associated with the rest of the plate.

The variation in strengths and uniform elongations measured for 45° tensile specimens through the thickness of the plate generally follow those observed for longitudinal tensile specimens (Figure 14 and 15). The range within which these variations occur, however, is considerably less compared to the longitudinal orientation; 40 MPa (5.7 ksi) for both the yield and ultimate strengths of 45° tensile specimens measured at room temperature. Similar to the longitudinal orientation, the 45° tensile specimens exhibit an increase in strength with decreasing temperature, although predominantly at a lower overall strength level for mid-thickness and tenth-thickness (Figures 21 and 22). Quarter-thickness 45° tensile specimens follow this trend, but at near equivalent values compared to that measured for longitudinal tensile specimens. Measured tensile elongations at 45° are also predominantly lower than their longitudinal counterparts (Figure 23). The uniform elongation values, however, do not increase monotonically with decreasing temperatures as do the tensile properties of longitudinal tensile specimens. By far, the most surprising result from the 45° tensile tests is the drop in elongation occurring from 200K to 77K for 45° tensile specimens at all levels of the plate. Work hardening plots indicate that tensile specimens tested at this set of conditions fail before the satisfaction of the necking criterion.

Similar to 45° tensile specimens, a minimum in the uniform elongation at 77K is also observed for long-transverse tensile specimens at mid-thickness, falling from 2.9% at room temperature to 1.2% at 77K (Figure 24c). At quarter-thickness, the long-transverse uniform elongations fall below 1% at all temperatures. This is in contrast to the other two orientations where an increase in the uniform elongation from mid-thickness to quarter-thickness is observed (Figures 14 and 15). However, the shape of the through-thickness strength profile observed for both longitudinal and 45° tensile specimens is preserved for long-transverse specimens; the long-transverse specimens show a higher overall stress level relative to both longitudinal and 45° tensile specimens. The range of the strength variation through the thickness increases slightly from the variation measured for 45° tensile specimens (40 MPa, 5.7 ksi) to 45 MPa (6.4 ksi) at room temperature, where it is

assumed that the greatest variation in strength occurs between mid-thickness and quarter-thickness, similar to that observed for both longitudinal and 45° tensile tests. Compared to Vintage I 2090-T81, both strengths and elongations measured for long-transverse oriented tensile specimens are considerably lower (Tables V and VI).

In order to examine the issue of in-plane anisotropy, the results of Tables III through V can be replotted as a function of tensile orientation as illustrated in Figures 25 through 27. With few exceptions, the results show a consistent drop in both the yield strength and ultimate strength at 45° at all levels of the material. The magnitude of this drop, however, varies with each through-thickness position. Mid-thickness tensile samples reveal the most dramatic drop, ranging from 35 MPa (5 ksi) to 70 MPa (10 ksi) between longitudinal and 45° orientations, respectively. Tenth-thickness samples exhibit a similar range. In contrast, quarter-thickness specimens do not drop by more than 25 MPa (3.5 ksi) for all test temperatures.

Fracture Properties

Any relationship between tensile and fracture properties are made increasingly difficult by the extent of the through-thickness anisotropy. Unlike the tensile properties, which can be measured for a given position in the thickness, fracture properties incorporate the entire thickness of the plate. As a result, measured toughness values are not only a result of the interplay between the intergranular and intragranular microstructures, but also of the state of stress throughout the material. Table VII summarizes the calculated K_{Ic} values for the three orientations and three temperatures. The toughness shows an improvement between 77K and 4K for L-T and T-L oriented specimens while L-45° K_{Ic} values exhibit a slight drop in toughness. A plot of the temperature dependence of the measured fracture toughness at the three orientations is shown in Figure 28. The anomalous drop in the measured fracture toughness between 77K and 4K exhibited by the L-45° specimens is coincident with the equally anomalous drop in 45° tensile elongation at 77K (Figure 23): the maximum L-45° K_{Ic} value at 77K corresponds to the minimum 45° uniform elongation value at the same temperature.

Whereas the fracture toughness increases from the L-T to the L-45° orientation, followed by a similar decrease to the T-L orientation for Vintage I 2090-T81, the fracture toughness values for Vintage III material, with the exception of those obtained at 77K, drop slightly at 45° and continue to drop at the T-L orientation. This difference is illustrated in Figure 29. Included in Table VIII are the respective toughness values for both 7075-T6, Vintage I 2090-T81 and 2219-T87.[8,15,20,21] Figure 30 replots the data of Tables III, VI, VII, and VIII as a graph of strength versus toughness along with the standard set of aerospace aluminum alloys at room temperature. Although Vintage III 2090-T81 does not fare well with its predecessor at cryogenic temperatures, its toughness is still superior to 7075-T6, the alloy 2090 was originally designed to replace.

Experimental Results: Mechanical Behavior

Tensile Behavior

Overlay plots of both $\partial\sigma/\partial\varepsilon$ and σ versus ε obtained from longitudinal tensile specimens taken at mid-thickness for all four test temperatures are shown in Figure 31. In all cases, failure occurs when the true stress is approximately equal to the instantaneous work hardening rate. Despite the fact that the intersection of σ and $\partial\sigma/\partial\varepsilon$ are well delineated at 300K and 200K only, it is clear that failure in tension occurs near the point of geometric instability and is not due to a premature brittle fracture. A comparison of the work hardening curves shows an increase of the work hardening rate with decreasing temperature (Figure 32). This increase retards the onset of geometric instability and results in improved measured uniform elongation values at lower temperatures. These trends are similar to those observed for Vintage I 2090-T81 and have been linked with increased stable deformation prior to fracture at low temperatures.[12,15]

Plots of $\partial\sigma/\partial\varepsilon$ versus σ shown in Figure 33 confirm the data above, indicating that both the stress and work hardening rate at the beginning of the region of stable deformation increases with decreasing temperature. These trends are consistent with other studies including those concerned with Vintage I 2090-T81.[15] Kocks[41] has linked this increase in work hardening with the increasing stress required to produce deformation, since thermally activated slip processes, such as cross-slip and dislocation climb, are not operative at lower temperatures. The increase in work hardening with decreasing temperature is accompanied by an increase in slip homogeneity as evidenced in Figure 33 by the approach to zero slope of the region of stable deformation. However, a comparison of the strain hardening behavior of the two vintages shows that the region of stable deformation for Vintage III 2090-T81 initiates at a higher value of the work hardening rate for all temperatures (Figure 34), differing by as much as 1500 MPa at 4K.

Similar to mid-thickness tensile specimens, failure of T/4 and 3T/4 specimens occur at approximately the instability point at all test temperatures (Figure 35). The work hardening rate increases steadily from 300K and 4K at mid-thickness whereas the work hardening rate at quarter-thickness exhibits a stall between 200K and 77K (Figure 36). A comparison between mid-thickness and quarter-thickness specimens shows that the work hardening rate for quarter-thickness specimens is notably lower at all test temperatures as indicated in Figure 37. A simultaneous decrease in the yield and ultimate strengths results in quarter-thickness uniform elongations similar in value to mid-thickness specimens at 200K and 77K. The disproportionate jump in the work hardening rate at 4K relative to the strength at quarter-thickness then results in a superior uniform elongation. At 300K the low elongation values measured result from the absence of a region of stable deformation (Figure 36).

A number of tensile specimens taken at 3T/4 and 9T/10 exhibited intergranular delamination prior to final fracture. Engineering stress-strain plots do not highlight the phenomenon since the measured strain value are invalid after splitting and subsequent strain relaxation of the specimen. However, plots of engineering stress versus displacement shown in Figure 38 do illustrate this splitting behavior. Note that the specimen continues

to elongate for a measurable amount before final fracture occurs. This type of behavior is indicative of a partial fracture of the material, where the remaining material intact continues to resist a load.

Composite plots of $\partial\sigma/\partial\varepsilon$ and σ versus ε for longitudinal tensile specimens taken at tenth thickness are shown in Figure 39. It is readily seen that specimens tested at 77K and 4K fail in the brittle mode prior to reaching the instability point. A comparison plot of the work hardening curves reveals a significant increase in the early part of work hardening between 77K and 4K (Figure 40). Increases in the instantaneous work hardening result in greater uniform elongation values for both mid-thickness and quarter-thickness tensile specimens. Hence, it is likely that if the interference of the brittle mode is suspended, a similar improvement in the uniform elongation will be observed for tenth-thickness specimens. It is clear that this potential for an improved elongation is hindered by the brittle mode (Figure 39).

As mentioned earlier, analysis of the fracture surface suggests that the mode change occurs only within the region of material containing equiaxed grains directly below both surfaces. To ascertain whether this mode change is the direct cause of the premature failure, additional longitudinal specimens were machined centered at eighth-thicknesses (T/8 and 7T/8). These tensile samples were thinned to 1.4 mm (0.055 in.) so that the specimens incorporated material from 0.9 mm (0.035 in.) to 2.3 mm (0.090 in.) from both surfaces. This specification effectively eliminated the region of equiaxed grains.

Tensile properties measured for these specimens at 4K are listed in Table IX. The superior elongations measured leave no doubt that the equiaxed grains undergo a ductile to brittle transition. Measured yield and ultimate strengths correlate well with similar values from both quarter-thickness and tenth-thickness positions immediately adjacent (Figure 41). Note that the combination of strength and elongation, particularly at T/8, is comparable to that of mid-thickness specimens at cryogenic temperatures. Figure 42 shows a comparison plot of $\partial\sigma/\partial\varepsilon$ versus σ for the eighth-thickness, mid-thickness and quarter-thickness longitudinal tensile specimens at 4K. Note that the T/8 curve resembles the mid-thickness curve while the 7T/8 curve resembles the quarter-thickness curve. The similarity in tensile behavior between the two pairs extends to the tensile properties (Table III and IX).

Work hardening plots for long-transverse tensile specimens taken at mid-thickness, shown in Figure 43, show failure prior to the instability point at all temperatures. The greatest elongation value is exhibited at 300K, failure occurring earlier with decreasing temperature. Quarter-thickness specimens fare more poorly as failure occurs immediately after yielding for all temperatures (Figure 44). Measured elongations for both mid-thickness and quarter-thickness specimens confirm this early brittle failure mode (Table V).

Failure modes observed for 45° tensile specimens taken at mid-thickness are highly temperature dependent, as illustrated in Figure 45. At 200K, the necking criterion is satisfied, whereas at 77K, it is clearly not. At both 300K and 4K, failure occurs near the point of instability. Fracture in all cases occurs along the grain boundaries normal to the long-transverse direction indicating that these grain boundaries provide a lower energy

fracture path than those normal to the longitudinal direction (Figure 46). This fracture behavior is not unusual since the texturing of grains are linked more strongly between grains along the rolling direction rather than those adjacent to each other. An improvement in the work hardening curve occurs from 300K to 200K, where the instability point is reached. At 77K, however, a drastic degradation in the mechanical behavior is exhibited as failure occurs much earlier than at both the 300K and 200K conditions. The work hardening improvement then continues between 77K and 4K. This odd behavior suggests two deformation processes which dominate the higher and lower temperatures, respectively. This anomaly also appears to affect the ensuing fracture toughnesses measured for L-45° J_{Ic} specimens (Figure 28). Quarter-thickness tensile specimens at the 45° orientation highlight this anomaly again where the a clearly brittle failure mode intrudes at 77K (Figure 47). In nearly all cases, the work hardening curve for 45° tensile specimens taken at quarter-thickness is observed to extend farther, thus resulting in a slightly greater uniform elongation value compared to mid-thickness, 45° tensile specimens. Plots of the work hardening rate versus true stress shown in Figure 48 shows that this increase in elongation results from a slightly improved region of stable deformation for quarter-thickness specimens: the slope of the region of stable deformation is shallower for quarter-thickness specimens.

The overall difference in mechanical behavior between mid-thickness and quarter-thickness is best highlighted by a comparison between the work hardening behaviors of longitudinal and 45° specimens. Figure 49 illustrates the decrease in the deformation homogeneity which occurs at 45°, where the region of stable deformation in the $\partial\sigma/\partial\varepsilon$ versus σ plot is significantly steeper for the 45° specimens compared to longitudinal tensile specimens at mid-thickness. In contrast, a comparison of $\partial\sigma/\partial\varepsilon$ versus σ plots between the longitudinal and 45° tensile specimens taken at quarter-thickness reveal similar characteristics at all temperatures but 77K (Figure 49). This difference is most dramatic at 4K (Figure 49d).

Slip Line Observations

Slip relief patterns taken from mid-thickness and quarter-thickness tensile specimens tested at 77K are shown in Figure 50. A coarser slip distribution prevails at T/2. The greater amount of continuous slip across grain boundaries at T/2 suggests a greater degree of texture or alignment among the grains at mid-thickness. A change in the slip direction from grain to grain is more obvious at quarter-thickness. A corresponding comparison at 300K reveals a similar difference in grain misorientation. In contrast to the 77K observations, however, a coarser slip distribution is now associated with the quarter-thickness position. This difference is coincident with the absence of a region of stable deformation discussed in the previous section.

Fracture Behavior

The most prominent result obtained by fracture surface observations is the absence of a change in the primary fracture mode, and thus the state of stress, with tempearture in the longitudinal orientation. Figure 51 shows the fracture surfaces at mid-thickness of Vintage III 2090-T81 J_{Ic} specimens for the three test temperatures. The ductile fracture

mode consists primarily of transgranular shearing connected by splitting along planar grain boundaries parallel to the load axis. Previous work on Vintage I 2090-T81 exhibit a similar preservation of this ductile mode.[12,15] Similar features can be seen at the subgrain level along with a few regions of ductile rupture, the latter being dominant at 300K and disappearing at cryogenic temperatures. The fracture surface at quarter-thickness and tenth-thickness reveals similar results but on a larger scale (Figure 52 and 53).

As demonstrated by the longitudinal tensile specimens taken at eighth-thickness, the low uniform elongation values are due to the region of equiaxed grains near the surface and suggests a change in the fracture mode. Since the thickness of this region is approximately only 500 μm, it is not surprising that a general fracture analysis reveals no change (Figure 53). A fracture surface study of the tensile specimens is more revealing. Figure 54 shows that the brittle fracture mode at the surface intervenes near 77K. The effect of this mode change results in a premature fracture within the equiaxed grains. Figure 55 shows that this fracture extends only as far as the end of this region of equiaxed grains at which point the large planar boundaries associated with the elongated grains directly below arrests any further crack progress. Elimination of this near surface microstructure lead to greater elongations as discussed earlier.

The similar fracture surface features provides another mean, in addition to optical microscopy, to determine the variation of the microstructural character throughout the thickness of the plate. Returning to Figures 51 through 53, it is apparent that the grain size is significantly larger at the quarter-thickness position than at mid-thickness. The absence of subgrains at quarter-thickness is also reverified. In agreement to the optical study, the T/10 fracture surfaces reveal a return of subgrain features. The degree of through-thickness variations exemplified by both yield strengths and microhardness values is further emphasized by the fracture surfaces observed at the 9T/10 position (Figure 56), where the extent of subgrain features is much greater than its counterpart (T/10).

Fracture profiles of Vintage III 2090-T81 L-T J_{Ic} specimens reveal the intergranular splitting that occurs perpendicular to both the crack plane and crack propagation direction (Figure 57). Figure 58 shows that splitting occurs predominantly along the large planar grain boundaries parallel to the rolling plane of the material. This observation has also been made for Vintage I 2090-T81.[11,13-15,24] Glazer[15] has reported on the frequency of such secondary splits for Vintage I 2090-T81 both quantitatively and qualitatively; an average split spacing of approximately 0.5 mm is measured for splits of 0.2 mm or greater with a maximum split depth of 0.9 mm at 77K. A qualitative optical study on the splitting behavior of Vintage III 2090-T81 reveals a wider spacing between splits. More importantly, the deepest splits observed in the Vintage III material are roughly three times the depth of its predecessor. Unlike Vintage I 2090-T81, where a definite increase in splitting is observed at 77K, the splitting behavior is more or less equivalent at the three test temperatures. The surface of a split from a tensile specimen, shown in the micrographs of Figure 59, reveal a rough topology produced by the tearing of the grain boundaries. A number of light colored particles can be seen throughout the entire surface. Through energy dispersive spectroscopy (EDS), these particles were determined to contain a high concentration of iron. The average weight percentages measured by EDS suggest that the

inclusions are Al_7Cu_2Fe particles. This insoluble phase is common among the aluminum-copper alloys.[42] A comparison between Figures 51 through 53 and 59 reveals that the grain boundaries contain a greater density of the Al_7Cu_2Fe particles suggesting the segregation of this phase toward the grain boundaries during thermomechanical processing. The formation of this phase may also contribute to a significant reduction in the amount of available copper for the formation of the T_1 strengthening phase during subsequent heat treatments[43] hence lowering the achievable strength.

T-L J_{Ic} specimens exhibit a flatter fracture profile as demonstrated by Figure 60. The flatness of the fracture plane suggests that this orientation is more susceptible to crack propagation along the grain boundaries normal to the long-transverse direction. The low uniform elongation values measured for long-transverse tensile specimens and their brittle mode of failure corroborate this observation. The long-transverse grain boundaries thus provide a low energy path by which failure can occur. Crack propagation in L-45° J_{Ic} specimens can be seen to deflect towards this same low energy path. As a result, fracture toughness values measured for L-45° J_{Ic} specimens are higher than those measured for T-L specimens. Suresh[44,45] has shown that crack deflection raises the apparent plane strain fracture toughness of a J_{Ic} specimen. The crack deflection observed for L-45° specimens, however, does not compensate for the easier crack propagation along the long-transverse boundaries at 300K and 4K and results in a lower fracture toughness than those measured for L-T specimens. An anomaly arises for fracture toughness values measured for L-45° J_{Ic} specimens tested at 77K. A maximum in the fracture toughness is linked to a minimum in the uniform elongation. The effect of the increased brittleness observed for 45° tensile specimens at 77K (Figures 23,45, and 47) can be seen in the fracture surface of L-45° J_{Ic} specimens (Figures 61 and 62). The fracture surfaces at 77K at both mid-thickness and quarter-thickness of L-45° J_{Ic} specimens reveal more shear features than those observed at 300 and 4K suggesting that plane stress deformation is easier at 77K. This anomaly is discussed below.

Discussion

Vintage III 2090-T81

It is readily observable that the wide range of microstructures gives rise to a number of differing mechanical responses. The optical study strongly indicates that Vintage III 2090-T81 in the form of a 12.7 mm (0.5 in.) plate is partially recrystallized early in the rolling process. The distinct break seen in the micrograph of Figure 12 separates two distinct regions of the plate material. The thinner grains are those which remain unrecrystallized while the thicker grains are recrystallized grains which have undergone further rolling. Bull and Lloyd[46] have noted a similar structure in aluminum-lithium alloys undergoing low overaging temperatures. Variations in the mechanical properties and mechanical behavior discussed above corroborate with this hypothesis. In particular, a parallel is observed in the manner in which work hardening improves in the longitudinal orientation with decreasing temperature between mid-thickness Vintage III 2090-T81 tensile specimens and tensile specimens taken from the fully unrecrystallized Vintage I material (Figure 34). This improvement trend differs considerably from the work hardening behavior observed for Vintage III tensile specimens taken at quarter-thickness (Figure 37). By far the strongest evidence procured by tensile tests is the dependency of the in-plane anisotropy on the through-thickness position. The in-plane strength anisotropy associated with Vintage I 2090-T81 is effectively eliminated in the Vintage III material at the quarter-thickness positions (Figures 25 through 27). This result is consistent with other studies that have shown that recrystallized grain structures exhibit better in-plane properties than unrecrystallized structures.

The principal difference between unrecrystallized and recrystallized grain structures resides in the degree of grain boundary misorientation.[47] Recrystallization softens the intense texture developed within rolled aluminum alloy products. Although an increase in isotropy in the plane is achieved, the subsequent side effect is the increase in grain boundary misorientation. When the grain size is small, a recrystallized grain structure is beneficial as the grain boundaries become effective barriers to shorter slip bands. Above a critical grain size, however, the combination of large misorientations and longer slip bands produce stress concentrations which are not easily alleviated by the transfer of slip.[41,48] This effect may increase the incidence of intergranular fracture and result in lower fracture toughness. This behavior becomes more notable at cryogenic temperatures as evidenced by the low fracture toughness of recrystallized aluminum-lithium alloys.[15,16] Unrecrystallized structures, such as Vintage I 2090-T81, alleviate this stress concentration by reducing the degree of grain misorientation and thus accommodating slip continuity across grain boundaries.[47] These structures increase the probability of higher energy transgranular fracture and improved cryogenic toughness. However, the directionality associated with unrecrystallized structures results in improvement only in one orientation, namely parallel to the rolling direction. It is important to note that despite the excellent correlation between the observed microstructural differences between mid-thickness and quarter-thickness and their respective in-plane tensile properties, Vintage III 2090-T81 can still be classified as an unrecrystallized structure. The term 'recrystallized structure' is more often reserved for those materials which undergo recrystallization during the final aging process. However, it

is observed in this study that even a recrystallization event prior to the final aging process does significantly influence the properties and behavior of the final product.

As mentioned above, this influence can best be seen in the mechanical behavior of test specimens taken at differing positions and orientations. Longitudinal quarter-thickness specimens exhibit decreased work hardening rates at all test temperatures relative to mid-thickness specimens (Figure 37). Additionally, the manner by which the work hardening rate improves with decreasing temperature is also indicative of the significant difference between recrystallized and fully unrecrystallized grain structure. 45° tensile tests provide evidence of a partially recrystallized structure. Tensile specimens taken at mid-thickness exhibit a larger drop in yield and ultimate strengths from the longitudinal to 45° orientation compared to the quarter-thickness position (Figures 25 and 26). The improvement in yield strength isotropy at quarter-thickness strongly suggests a less intense texture. This isotropy is further demonstrated through plots of $\partial\sigma/\partial\varepsilon$ versus σ where 45° quarter-thickness tensile specimens exhibit similar initial work hardening characteristics within the region of stable deformation to longitudinal quarter-thickness specimens (Figure 49). In contrast, the work hardening behavior of 45° mid-thickness tensile specimens deviate considerably from the work hardening behavior of their longitudinal counterparts.

The brittle failure mode of long-transverse tensile specimens (Figures 43 and 44) and the flatter fracture profile of T-L J_{Ic} specimens (Figure 60) indicate a weaker long-transverse grain boundary (those grain boundaries normal to the long-transverse direction) relative to longitudinal grain boundaries. This assertion is consistent with the lower uniform elongation values measured for long-transverse tensile specimens taken from quarter-thickness compared to values for long-transverse tensile specimens taken from mid-thickness; the larger long-transverse grain boundaries lead to a more brittle structure. The weakness of the long-transverse grain boundaries suggests that the process of texturing during rolling is associated more with those grains which lie on a concurrent line parallel to the rolling direction and those immediately below. The lesser interaction between grains which lie adjacent to each other allow both to evolve towards the same texture, but individually.

One of the more surprising differences in mechanical behavior observed is the drop in elongation at 77K for 45° tensile specimens. Figure 63 replots Figures 23 and 28 to illustrate the monotonic increase in both fracture toughness and uniform elongation for the longitudinal orientation. In contrast, 45° oriented test specimens exhibit a drop in elongation at 77K that is linked to a maximum in the fracture toughness (Figure 64). The dramatic difference between the two orientations can be related to the distribution of T_1 precipitates. Recall that the thermomechanical treatment of 2090 includes a stretch parallel to the rolling direction prior to aging. This stretch produces dislocations along preferred {111} planes. Since this stretch occurs only along one direction, the number of activated {111} planes will be either one or two. T_1 precipitates then nucleate heterogeneously along these planes. The high degree of texture and hence grain alignment already existing in the hot-rolled 2090 plate results in a high degree of alignment of {111} planes among the grains and thus produces a inhomogeneity in the distribution of T_1 precipitates among the different variants. Following a similar scenario, Kim and Lee[19] have hypothesized that for

a significant range of off-axis orientations, those slip planes containing the greater distribution of T_1 precipitates are no longer preferred. As a result, deformation is made easier as slip is able to cut through the less densely T_1 populated planes.

It is apparent that the difference in slip resistance between the longitudinal and 45° orientation allows a second process of deformation to occur. The effect of this phenomenon can be seen in Figures 61 and 62 where the J_{Ic} fracture surfaces reveals an overall cleaner fracture surface at 77K. This behavior at 45° of test specimens at cryogenic temperatures poses a number of questions regarding the source of the alternate mode of deformation observed at 77K. Recall from Figures 57 and 58 that intergranular splitting occurs throughout the range of test temperatures. Qualitative analysis does not show any significant differences in the depth of the splits with temperature. However, at 77K and 4K, the number of smaller splits can be seen to increase. Tensile tests reveal that at 77K, failure occurs at a higher work hardening rate than at other temperatures; well before the satisfaction of the necking criterion and the intervention of stress triaxiality.

The majority of existing models for strain-controlled fracture predict proportional increases in the toughness with increases in other deformation properties, namely the yield strength, elongation, and the work hardening rate in the absence of a fracture mode change.[49-52] This relation is contingent on the preservation of a single fracture mode within the temperature range of interest.[15,26] In the longitudinal and L-T orientation, where the preservation of a ductile fracture mode is observed (Figures 31 and 35), such a scaling exists, where the fracture toughness, strength, and elongation at mid- and quarter-thickness all increase with decreasing temperature (Figures 17 and 63). In contrast, 45° tensile tests exhibit a drop in the elongation at 77K whereas the fracture toughness increases to a maximum. Figures 45 and 47 indicate that failure at 77K occurs in a brittle mode before the satisfaction of the necking criterion. This change in fracture mode can also be observed at the fracture surface, where a greater amount of shear dominates at 77K (Figures 61 and 62). When such a change in the primary fracture mode occurs in response to a change in the test temperature, it will dominate the fracture toughness response. As such, the relation between the fracture toughness and tensile behavior based on strain-controlled fracture models are no longer stringent.

The change in fracture mode observed between 200K and 77K for the 45° orientation results in a non-parallel behavior of the elongation and fracture toughness. Although the nature of this intruding fracture mode was not studied, the observed results suggest that the question of *when* splitting occurs plays a significant role. Consider that splits are observed at 77K and that these splits are not of decreased depth or number relative to the other test temperatures (Figures 57 and 58). The early failure of tensile specimens suggest that these splits must form well before plane strain conditions dominate. Consequently, plane stress conditions are preserved. The fracture surface of 45° J_{Ic} specimens tested at 77K (Figures 61 and 62) reveal a greater degree of shear planes relative to L-T J_{Ic} specimens also tested at 77K (Figures 51 and 52). The presence of more shear type features suggest that the L-45° J_{Ic} specimens, by virtue of splitting early, are able to utilize essentially undeformed laminates under plane stress conditions. At 4K the dispersion of these shear planes and greater amount of plane strain type fracture features

then indicate that splitting occurs comparatively later. This may be explained by the improved deformation behavior at 4K within the grains which retards the production of large stress concentrations at the grain boundaries and inhibits splitting. Upon splitting, the individual laminates have already developed a strong dislocation structure and hence cannot fully utilize the plane stress state.

This pronounced anomaly in splitting behavior at 77K is not unique and has been seen for Vintage I 2090-T81 also.[15] In particular, tensile tests exhibited more extensive splitting at 77K. The conditions required for the occurrence of splitting are difficult to define. A literature search through the research work on steels by Glazer[15] has established the need for highly elongated grains with large planar grain boundaries. Splits are then caused by intense slip at these boundaries. The softer texture associated with the Vintage III material may contribute to the production of such intense slip. For Vintage III 2090-T81, Al_7Cu_2Fe impurities along the large planar boundaries resulting from a high iron concentraion also appear to be a strong contributing factor (Table II). During the thermomechanical processing of the plate, these impurities segregate towards the planar grain boundaries. Due to the large grain size of the Vintage III material, the total grain boundary area is decreased and a significant increase in the area density of the iron-containing particulates results. Both the decrease in the texture and the increase in grain boundary impurities may explain the deeper splits found in the Vintage III material compared to its predecessor. This reasoning is corroborated by the Vintage III material where Figure 58 shows that the deepest splits occur at the regions containing the largest grains and hence smallest amount of grain boundary area.

The improvement in yield strength anisotropy both through the thickness and in the plane of Vintage III 2090-T81 is significant. However, these improvements come at the cost of the overall ductility and fracture toughness of the material. Additionally, the delamination behavior of the material is worse. Although the spacing between splits appear to be greater in the Vintage III material, the depth of the splits are three to four times longer. Despite these latter shortcomings, the fracture toughness values at cryogenic temperatures are still comparable to those measured for 2219-T87 with the same improvement in strength as originally presented in the Vintage I material. With the additional benefit of the reduced anisotropy, Vintage III 2090-T81 has demonstrated limited success. The strongest antagonist to this success is the delamination behavior which, observing the deeper splits, implies a much weaker short-transverse grain boundary. As a consequence, greater care must be taken in understanding the limits of this alloy.

Vintage III 2090-T81 versus Vintage I 2090-T81

Whereas Vintage I 2090-T81 acquires its through-thickness anisotropy primarily from a parallel variation in texture, wide variations in the polygranular microstructure appear to be an equally dominant reason for the anisotropy associated with the more recent vintage. The results indicate that the longitudinal yield strength anisotropy through the thickness of Vintage I 2090-T81 12.7 mm (0.5) in.) plate is reduced in the Vintage III material. Unlike the monotonic drop in yield strength observed from mid-thickness to the surface in the earlier vintage, Vintage III 2090 exhibits a minimum near both quarter-

thickness positions bordered by maxima at mid-thickness and the two surfaces (Figure 65). The result is a strength variation of no more than approximately 100 MPa (15 ksi) at room temperature in the longitudinal yield strength through the thickness, a 15% reduction in the 120 MPa (17 ksi) difference of the earlier vintage. The yield strength anisotropy in the plane of the plate is also reduced in the Vintage III material. This improvement, however, only occurs within selected levels of the plate, namely at quarter-thickness (Figure 66). At mid-thickness, within the range of fully unrecrystallized material, no significant improvement is observed.

Despite the improvements in the yield strength anisotropies, uniform elongations reveal a significantly lower ductility in the Vintage III alloy. The poorer deformation properties of the alloy are a direct product of the degradation in work hardening ability relative to Vintage I 2090-T81. As demonstrated in Figure 34, the region of stable deformation for Vintage III 2090-T81 initiates at a higher stress level and decreases at a more rapid pace. The two factors combined indicate that Vintage III 2090 exploits its work hardening ability earlier in the course of the tensile test as compared to its predecessor. The rapid decrease in this work hardening may then be due to subsequent hardening insufficient to overcome the inherent softening mechanisms of the material. At 300K, this effect is less obvious.

The differences observed between the two vintages are directly related to differences in the thermomechanical processing received by the two vintages. As mentioned above, strong evidence supports the hypothesis that the Vintage III material is partially recrystallized during the thermomechanical processing. Though a partial recrystallization event occurs during the rolling process, there is no means to determine when in the process this event actually transpires. It is apparent by the elongated nature of the grains at quarter-thickness that the material undergoes further deformation after the recrystallization event. Since aluminum alloys are known to develop texture early in the rolling process, the post-recrystallization deformation would have to be relatively light to avoid nullifying the effect of recrystallization.[53] This reasoning would explain the larger grain size observed for the Vintage III material as subsequent exposure to high temperatures with little deformation allows unrestricted grain growth.

It is apparent that Vintage III 2090 attempts to mix the features of recrystallized and unrecrystallized structures. In this way, both the through-thickness and in-plane anisotropies may be lessened without loss to the cryogenic strength-toughness combination. Despite the non-ideal result, the strength-toughness combination is still superior to the current aerospace aluminum alloy 2219-T87 (Figure 30). The data accumulated in this study strongly imply that a fully and monotonic unrecrystallized grain structure as observed in Vintage I 2090-T81 is necessary to obtain excellent cryogenic fracture toughness. A similar conclusion is arrived at by Starke and Lin[48] for aluminum alloy 2020 where the poor ductility and fracture toughness are associated with a partially recrystallized structure. As discussed earlier, aluminum-lithium alloys with recrystallized structures exhibit poor cryogenic toughness[15,16] while those with unrecrystallized structures, such as Vintage I 2090-T81, exhibit improved cryogenic properties.[9,12,15] It is evident that the various polygranular microstructures observed in Vintage III 2090-T81

give rise to varying degrees of toughness and ductility. The large grains associated with the quarter-thickness position are thus expected to exhibit lower toughness at cryogenic temperatures due to a softened texture, thereby lowering the overall toughness of the material as compared to Vintage I 2090-T81.

The complex microstructure of Vintage III 2090-T81 can be compared to a laminated composite. As such, the mechanical properties as a whole are strongly influenced by the properties of the constituent materials, their distribution,and the interaction among them. Consequently, caution must be taken since the reduction in the thickness of the original alloy through machining will nullify the improvements in isotropy found in this vintage.

Summary and Conclusion

The mechanical properties and mechanical behavior of Vintage III 2090-T81 in the form of a 12.7 mm (0.5 in.) plate are strongly influenced by the layered laminate-like grain structure. This grain structure can be regarded on two levels: the elongated grains found throughout most of the material provides one mode of layering while the variation in the thickness of the elongated grains provide the other. The evidence summarized below indicates that this wide spectrum of microstructures is produced by a partial recrystallization during the thermomechanical processing prior to the final solution heat treatment and aging.

The yield strength through-thickness profile exhibits minima near the quarter-thickness positions with maxima at the center and near both surfaces. This variation is an improvement over the parabolic profile of the earlier vintage. Overall, the through-thickness anisotropy is reduced by 15% at room temperature. In a similar manner, improvement in the in-plane anisotropy is also observed but is restricted to certain locations in the plate thickness. This sensitivity to plate position also results from the partial recrystallization, where the in-plane anisotropy is essentially eliminated within the pre-recrystallized region at quarter-thickness. In contrast, the region of fully unrecrystallized grains at mid-thickness do not show any significant improvement over the Vintage I material in the in-plane anisotropy. The strong differences between mid- and quarter-thickness positions are further exemplified by their fracture and deformation behavior. In particular, the manner in which the work hardening behavior varies with temperature is strongly linked with the through-thickness position.

Although the modified thermomechanical processing of Vintage III 2090 does improve the yield strength isotropy, the dramatic increase in the depths of the short-transverse splits that occur in J_{Ic} specimens indicates a significantly weaker short-transverse grain boundary. This is believed to be the result of a high concentration of iron-containing impurities that tend to segregate toward the large planar grain boundaries and a less intense texture. The deeper splits do not appear to significantly affect the longitudinal properties of Vintage III 2090. However, the weaker short-transverse grain boundaries is believed to be partly responsible for the change in the primary fracture mode observed at 77K in the 45° orientation.

Despite the numerous shortcomings of Vintage III 2090-T81, measured fracture toughnesses at room to cryogenic temperatures are still superior to or at least comparable to both 7075-T6, the material originally to be replaced by 2090, and 2219-T87, the alloy projected to be replaced by 2090 in aerospace systems. Additionally, the Vintage III material provides roughly the same superiority in strength as its predecessor.

Overall, the differences in mechanical properties between mid- and quarter-thickness positions are a direct consequence of the partial recrystallization process. This thermomechanical procedure also provides the differences observed between Vintage III and Vintage I 2090-T81, and is particularly noticeable in the measured fracture toughnesses. The disruption of the monolithic unrecrystallized structure originally observed in Vintage I 2090-T81 is believed to be the primary cause of the loss in cryogenic toughness. This demonstrates the necessity for a fully unrecrystallized structure in order to attain superior cryogenic toughness.

Acknowledgements

First and foremost, I wish to thank the Alcoa Technical Center for supplying the material for this work, Jin Chan for his assistance in cryogenic testing, and Shelly Miyasato for her assistance in the TEM study. Without their contributions, this work would never have taken place.

This work was jointly supported by the Director, Office of Energy Research, Office of Basic Energy Science, Material Sciences Division of the U.S. Department of Energy under Contract No. DE-AC03-76SF00098. I was also supported under a National Science Foundation Graduate Fellowship for the entire period of this work.

In addition to those mentioned above, there are numerous people who have contributed in many ways, both directly and indirectly, big and small. I would like to thank those who by way of their involvement in the realm of aluminum-lithium alloys have helped in my initiation into graduate student life: Judy Glazer, Stephanie Verzasconi, Ralph Sawtell, Roger Emigh, Anne Sunwoo, and more recently, Shelly Miyasato and Trey Bradley. Special thanks are due to Judy Glazer for bringing me through the ranks of respect and especially for perpetually inciting my "love" for research. Enough thanks cannot be given to Bill Morris who through his support and constant belief in my ability has made my graduate career at Berkeley so far an overwhelming success.

Finally, I would like to thank my parents for their support throughout the entire course of my education and more importantly for instilling in me the desire to do to the best of my ability, to live to the fullest that life offers, and to laugh as often as possible.

References

1. E.S. Balmuth and R. Schmidt: *Aluminum-Lithium Alloys*, T.H. Sanders, Jr. and E.A. Starke, Jr. eds., TMS-AIME, New York, NY, 1981, pp. 69-88.

2. G.H. Narayanan, B.L. Wilson, W.E. Quist, A.L. Wingert: Technical Report D6-51411, The Boeing Company, Seattle, WA, August, 1982.

3. R.E. Lewis, D. Webster, and I.G. Palmer: Final Report, USAF Contract F33615-77-C-5186, Technical Report No. AFML-TR-78-102, July 1978.

4. I.F. Sakata: Final Report, NASA CR-165820, NASA Contract NAS1-164634, 1982.

5. J.C. Ekvall, J.E. Rhodes, G.G. Wald: *Design of Fatigue and Fracture Resistant Structures*, ASTM STP 761, American Society for Testing and Materials, 1982, pp. 328-341.

6. E.A. Starke, Jr., T.H.Sanders, Jr., and I.G. Palmer: *J. of Metals*, 1981, pp. 24-33.

7. K.K. Sankaran,and N.J. Grant: *Aluminum-Lithium Alloys*, TMS-AIME, Warrendale, PA, 1981, pp. 205-227.

8. R.J. Bucci, R.C. Malcolm, E.L. Colvin, S.J. Murtha, and R.S. James: Final Report NSWC TR 89-106, Aluminum company of America, Alcoa Center, PA, September, 1989.

9. J.Glazer, S.L. Verzasconi, E.N.C. Dalder, W. Yu, R.A. Emigh, R.O. Ritchie, and J.W. Morris, Jr.: *Adv. Cryogenic Eng.*, vol. 32, 1986, pp. 397-404.

10. J.Glazer, J.W. Morris, Jr., S.A. Kim, M.W. Aushi, and H.M. Ledbetter: *AIAA Journal*, vol. 25, pp. 1271.

11. C. Dorward, *Scripta Metall.*, vol. 20, 1986, pp. 1379-1383.

12. J. Glazer, S.L. Verzasconi, R.R. Sawtell, and J.W. Morris, Jr.: *Metall. Trans. A*, 1987, vol. 18, pp. 1695-1701.

13. K.T. Venkateswara Rao, W. Yu, and R.O. Ritchie, *Metall. Trans. A*, 1989, vol. 20, pp. 485-497.

14. K.T. Venkateswara Rao, F.H. Hayashigatani, W. Yu, and R.O. Ritchie, *Scripta Metall.*, vol. 22, 1988, pp. 93.

15. J. Glazer: Ph.D. Thesis, LBL-27607, Berkeley, CA, July 1989.

16. W.E. Quist, and G.H. Narayanan: *Treatise on Materials Science and Technology: Aluminum Alloys - Contemporary Research and Applications*, A.K. Vasudévan and R.D. Doherty, eds., vol. 31, Academic Press, Inc., SanDiego, CA, 1989, pp. 219-254.

17. A.K. Vasudévan, W.G. Fricke, Jr., R.C. Malcolm, R.J. Bucci, M.A. Przystupa, and F. Barlat: *Metall. Trans. A*, vol. 19, 1988, pp. 731-732.

18. A.K. Vasudévan, W.G. Fricke, Jr., M.A. Przystupa, and S. Panchanadeeswaran: *Eighth International Conference on Textures of Materials*, J.S. Kallend, and G. Gottstein, des., pp. 1071-1077, TMS, Warrendale, PA, 1988.

19. E.W. Kim and N.J. Lee: *Aluminum-Lithium Alloys V*, T.H. Sanders, Jr. and E.A. Starke, Jr., eds., Materials and Component Engineering Publications, Ltd., Birmingham, England, 1989, pp. 809-816.

20. R.S. James and R.J. Bucci: Lessons Learned - Aluminum-Lithium Alloy Development, ALCOA, Alcoa Technical Center, PA, 1989.

21. R.J. Rioja, B.A. Cheney, R.S. James, J.T. Staley, and J.A. Bowers: *Structure-Property Relationships in Al-Li Alloys: Plate and Sheet Products*, ALCOA, Alcoa Technical Center, PA, 1989.

22. M. Peters, J. Eschweiler, and K. Welpmann: *Scripta Metall.*, vol. 20, 1986, p. 259.

23. M.J. Bull and D.J. Lloyd: *Aluminum-Lithium Alloys III*, C. Baker, P.J. Gregson, S.J. Harris, and C.J. Peel, eds., The Institute of Metals, London, England, 1986, pp. 402-410.

24. R. Crooks and J.R. Porter: MRS Publications, Pittsburg, PA, 1988.

25. J.W. Morris, Jr. and J.Glazer: LBL-25254, Berkeley, CA, 1988.

26. J. Glazer and J.W. Morris, Jr.: *Aluminum-Lithium Alloys V*, T.H. Sanders, Jr. and E.A. Starke, Jr., eds., Materials and Component Engineering Publications, Ltd., Birmingham, England, 1989, pp. 1471-1480.

27. D. Webster: *Aluminum-Lithium Alloys III*, C. Baker, P.J. Gregson, S.J. Harris, C.J. Peel, eds., The Institute of Metals, London, England, 1986, pp. 602-609.

28. D. Webster: *Metall. Trans. A*, vol. 18, 1987, pp. 2181-2193.

29. Aluminum-Lithium Alloys I, T.H. Sanders, Jr. and E.A. Strarke, Jr., eds., TMS-AIME, Warrendale, PA, 1981.

30. Aluminum-Lithium Alloys II, T.H. Sanders, Jr., and E.A. Starke, Jr., eds., TMS-AIME, Warrendale, PA, 1984.

31. Aluminium-Lithium Alloys III, C. Baker, P.J. Gregson, S.J. Harris, and C.J. Peel, eds., The Institute of Metals, London, England, 1986.

32. Fourth International Aluminium Lithium Conference, G. Champier, B. Dubost, D. Miannay, and L. Sabetay, eds., Journal de Physique, Colloque C#, supplement au n°9, Tome 48, September, 1987.

33. Aluminum-Lithium Alloys V, T.H. Sanders, Jr. and E.A. Starke, Jr., eds., MCE Publications Ltd., Birmingham, England, 1989.

34. R.W.K. Honeycombe: *The Plastic Deformation of Metals*, 2nd ed., Edward Arnold, London, England, 1984, p. 231.

35. J.E. Hatch: *Aluminum: Properties and Physical Metallurgy*, ASM, Metals Park, Ohio, 1984, p. 110.

36. D.T. Read and R.P. Reed: *Adv. Cryo. Eng.*, vol. 26, 1980, pp. 91-101.

37. R.W.K. Honeycombe: *The Plastic Deformation of Metals*, 2nd ed., Edward Arnold, London, England, 1984, p. 457.

38. H. Mecking: *Work Hardening in Tension and Fatigue*, A.W. Thompson, ed., TMS-AIME, New York, NY, 1975, pp. 67-88.

39. J.E. Hatch: *Aluminum: Properties and Physical Metallurgy*, ASM, Metals Park, Ohio, 1984, p. 122.

40. N. Thorne, A. Dubus, J.M. Lang, F. Degreve, and P. Meyer: *4th International Aluminum-Lithium Conference*, G. Champier, B. Dubost, D. Miannay, and L. Sabetay, eds., Journal de Physique, 1987, vol. 48, colloque C3, pp. 521-526.

41. U.F. Kocks: *Trans. ASME: J. Eng. Matls. Tech.*, 1976, vol. 98 pp. 76-85.

42. J.E. Hatch: *Aluminum: Properties and Physical Metallurgy*, ASM, Metals Park, Ohio, 1984, p. 70.

43. W.A. Dean: *Aluminum, Vol. I*, K.R. Van Horn, ed., ASM, Metals Park, Ohio, 1967, pp. 163-208.

44. S. Suresh: *Metall. Trans. A*, vol. 14, 1983, pp. 2375-2385.

45. S. Suresh: *Metall. Trans. A*, vol. 16, 1985, pp. 249-260.

46. M.J. Bull and D.J. Lloyd: Aluminum-Lithium Alloys III, C. Baker, P.J. Gregson, S.J. Harris, and C.J. Peel, eds., The Institute of Metals, London, England, 1986, pp. 402-410.

47. E.A. Starke and W.E. Quist: *AGARD Conference Proceedings No. 444 - New Light Alloys*, AGARD, Essex, England, 1989.

48. E.A. Starke, Jr. and F.S. Lin: *Metall. Trans. A*, 1982, vol. 13, pp. 2259-2269.

49. G.G. Garrett and J.F. Knott: *Metall. Trans. A*, 1978, vol. 9, pp. 1187-1201.

50. R.O. Ritchie and A.W. Thompson: *Metall. Trans. A*, 1985, vol. 16, pp. 233-248.

51. R.O. Ritchie, W.L. Server, and R.A. Wulaert: *Metall. Trans. A*, 1979, vol. 10, pp. 1557-1570.

52. K. Jata and E.A. Starke, Jr.: *Metall. Trans. A*, 1986, vol. 17, pp. 1011-1026.

53. W.D. Rooney, J.M. Papazian, E.S. Balmuth, R.C. Davis, and P.N. Adler: *Aluminum-Lithium Alloys V*, T.H. Sanders, Jr. and E.A. Starke, Jr., eds., Materials and Component Engineering Publications, Ltd., Birmingham, England, 1989, pp. 799-808.

Phase	Composition	Crystal Structure	Morphology and Habit Plane
δ'	Al_3Li	$L1_2$ (fcc)	spherical or on β' surface
β'	Al_3Zr	$L1_2$	spherical
T_1	Al_2CuLi	hexagonal	plate, {111]

Table I: Important Strengthening Phases in Aluminum-Copper-Lithium Alloy 2090-T81.

Element	2090 (composition range)	Vintage III 2090-T81*	Vintage I 2090-T81*
Al	bal	bal	bal
Cu	2.4-3.0	3.05	2.86
Li	1.9-2.6	2.16	2.05
Zr	0.08-0.15	0.12	0.12
Fe	0.12	0.08	<0.02
Others	<0.05	<0.01	<0.02

* *As received.*

Table II: Compositions in Weight Percent of Aluminum-Copper-Lithium Alloy 2090-T81.

Through Thickness Position	Temperature (K)	Yield Strength MPa (ksi)	Ultimate Strength MPa (ksi)	Uniform Elongation (%)†
T/10	300	520 (75.4)	561 (81.3)	4.1
	200	524 (76.0)	532 (77.2)	---*
	77	521 (75.6)	571 (82.8)	5.5
	4	623 (90.3)	671 (97.3)	3.7
T/4	300	460 (66.7)	481 (69.8)	1.9
	200	459 (66.5)	501 (72.7)	6.9
	77	465 (67.4)	510 (73.9)	8.3
	4	504 (73.1)	578 (83.9)	9.6
T/2	300	517 (75.0)	551 (79.9)	4.5
	200	550 (79.7)	596 (86.4)	5.1
	77	567 (82.3)	638 (92.6)	6.9
	4	581 (84.3)	759 (110.1)	9.2
3T/4	300	421 (61.0)	446 (64.7)	1.4
	200	455 (66.0)	483 (70.0)	2.4
	77	473 (68.6)	506 (73.4)	3.8
	4	492 (71.3)	583 (84.6)	13.6
9T/10	300	428 (62.1)	468 (67.9)	5.7
	200	463 (67.2)	513 (74.4)	7.6
	77	514 (74.6)	552 (80.0)	1.9
	4	541 (78.4)	627 (90.9)	2.8

* *Elongation measurement invalidated due to extensive splitting during testing.*

† *Values obtained from initial gauge length of 32mm (1.25 in.)*

Table III: Longitudinal Tensile Properties of Vintage III 2090-T81 at Various Positions and Test Temperatures.

Through Thickness Position	Temperature (K)	Yield Strength MPa (ksi)	Ultimate Strength MPa (ksi)	Uniform Elongation (%)†
T/10	300	434 (63.0)	485 (70.4)	2.1
	200	437 (63.4)	481 (69.8)	1.7
	77	478 (69.3)	509 (73.8)	1.3
	4	514 (74.5)	572 (82.9)	2.5
T/4	300	435 (63.1)	483 (70.0)	2.6
	200	429 (62.2)	490 (71.0)	4.4
	77	463 (67.1)	510 (74.0)	2.3
	4	481 (69.7)	563 (81.6)	4.7
T/2	300	459 (66.5)	514 (74.6)	2.5
	200	476 (69.1)	534 (77.4)	3.1
	77	516 (74.9)	576 (83.5)	2.2
	4	542 (78.6)	635 (92.1)	4.3
3T/4	300	419 (60.8)	475 (68.9)	4.0
	200	440 (63.8)	491 (71.2)	3.7
	77	473 (68.6)	515 (74.7)	2.0
	4	487 (70.6)	583 (84.6)	6.3
9T/10	300	425 (61.7)	479 (69.5)	3.1
	200	431 (62.5)	478 (69.3)	2.5
	77	472 (68.4)	509 (73.8)	1.7
	4	501 (72.7)	563 (81.6)	3.0

† *Values obtained from initial gauge length of 32mm (1.25 in.)*

Table IV: 45° Tensile Properties of Vintage III 2090-T81 at Various Positions and Test Temperatures.

Through Thickness Position	Temperature (K)	Yield Strength MPa (ksi)	Ultimate Strength MPa (ksi)	Uniform Elongation (%)†
T/4	300	477 (69.2)	496 (71.9)	0.6
	200	495 (71.8)	514 (74.5)	0.9
	77	530 (76.8)	558 (80.9)	0.6
	4	542 (78.6)	586 (85.0)	0.7
T/2	300	519 (75.3)	579 (84.0)	2.9
	200	532 (77.2)	595 (86.3)	1.8
	77	583 (84.6)	632 (91.7)	1.2
	4	612 (88.8)	689 (99.9)	1.8
3T/4	300	475 (68.9)	490 (71.1)	0.4
	200	485 (70.3)	514 (74.6)	0.7
	77	522 (75.8)	548 (79.5)	0.6
	4	553 (80.2)	576 (83.6)	0.6

† *Values obtained from initial gauge length of 32mm (1.25 in.)*

Table V: LongTransverse Tensile Properties of Vintage III 2090-T81 at Various Positions and Test Temperatures.

Alloy	Temperature (K)	Yield Strength MPa (ksi)	Ultimate Strength MPa (ksi)	Uniform Elongation (%)†
Vintage I 2090-T81 T/2	300	535 (77)	565 (82)	5.0
	200	--	--	--
	77	600 (87)	715 (104)	7.0
	4	615 (89)	820 (119)	17.0
Vintage I 2090-T81 T/4*	300	455 (66)	490 (71)	5.5
	200	475 (69)	525 (76)	5.5
	77	525 (76)	625 (91)	14.0
	4	540 (78)	655 (95)	17.0
7075-T6	300	505 (73)	600 (87)	11‡
	200	545 (79)	620 (90)	11
	77	635 (92)	705 (102)	9
	4	770 (112)	830 (120)	8
2219-T87	300	385 (56)	465 (67)	12‡
	200	--	--	--
	77	460 (67)	575 (84)	14
	4	510 (74)	675 (98)	15

* *No distinction is made between top and bottom sections of the plate.*

† *Values obtained from initial gauge length of 32mm (1.25 in.)*

‡ *Values denote total elongations.*

Table VI: Longitudinal Tensile Properties of Vintage I 2090-T81, 7075-T6, and 2219-T87 at Various Positions and Test Temperatures (After Glazer, ref. 15).

Orientation	Temperauture (K)	Fracture Toughness K_{Ic} MPa$\sqrt{m}$ (ksi$\sqrt{in}$)
L-T	300	31 (28)
	77	42 (38)
	4	45 (40)
L-45°	300	31 (28)
	77	43 (39)
	4	42 (38)
T-L	300	22 (20)
	77	27 (25)
	4	39 (35)

Table VII: Fracture Toughness Properties of Vintage III 2090-T81 at Various Orientations and Test Temperatures.

Temperature (K)	Fracture Toughness, K_{Ic} MPa$\sqrt{m}$ (ksi$\sqrt{in}$)			
	Vintage III 2090-T81	Vintage I 2090-T81*	7075-T6*	2219-T87*
300	31 (28)	34 (31)	33 (30)	36 (33)
77	42 (38)	57 (52)	29 (26)	43 (39)
4	45 (40)	72 (65)	--	48 (44)

* *After Glazer, ref. 15.*

Table VIII: Fracture Toughness Values of Vintage III 2090-T81, Vintage I 2090-T81, 7075-T6, and 2219-T87 at Various Test Temperatures.

Through Thickness Position	Yield Strength MPa (ksi)	Ultimate Strength MPa (ksi)	Uniform Elongation (%)†
T/8	588 (85.3)	673 (97.6)	6.4
7T/8	465 (67.5)	543 (78.8)	10.9

† *Values obtained from initial gauge length of 32mm (1.25 in.)*

Table IX: Longitudinal Tensile Properties of Vintage III 2090-T81 at eighth-thickness and tested at 4K.

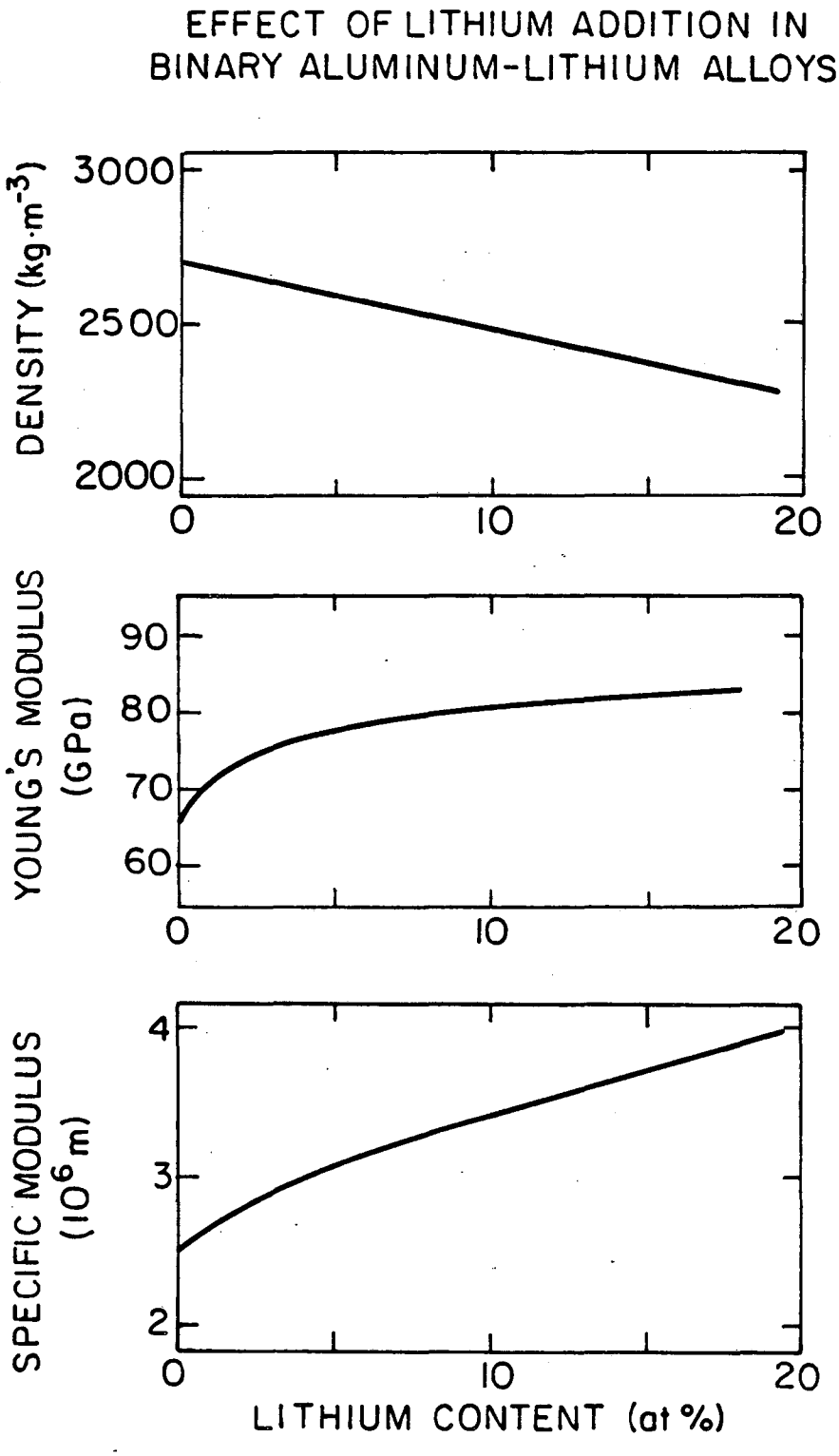

Figure 1: Plot of the effect of lithium content on the density, elastic modulus and specific modulus of aluminum alloys. (XBL 844-6938)

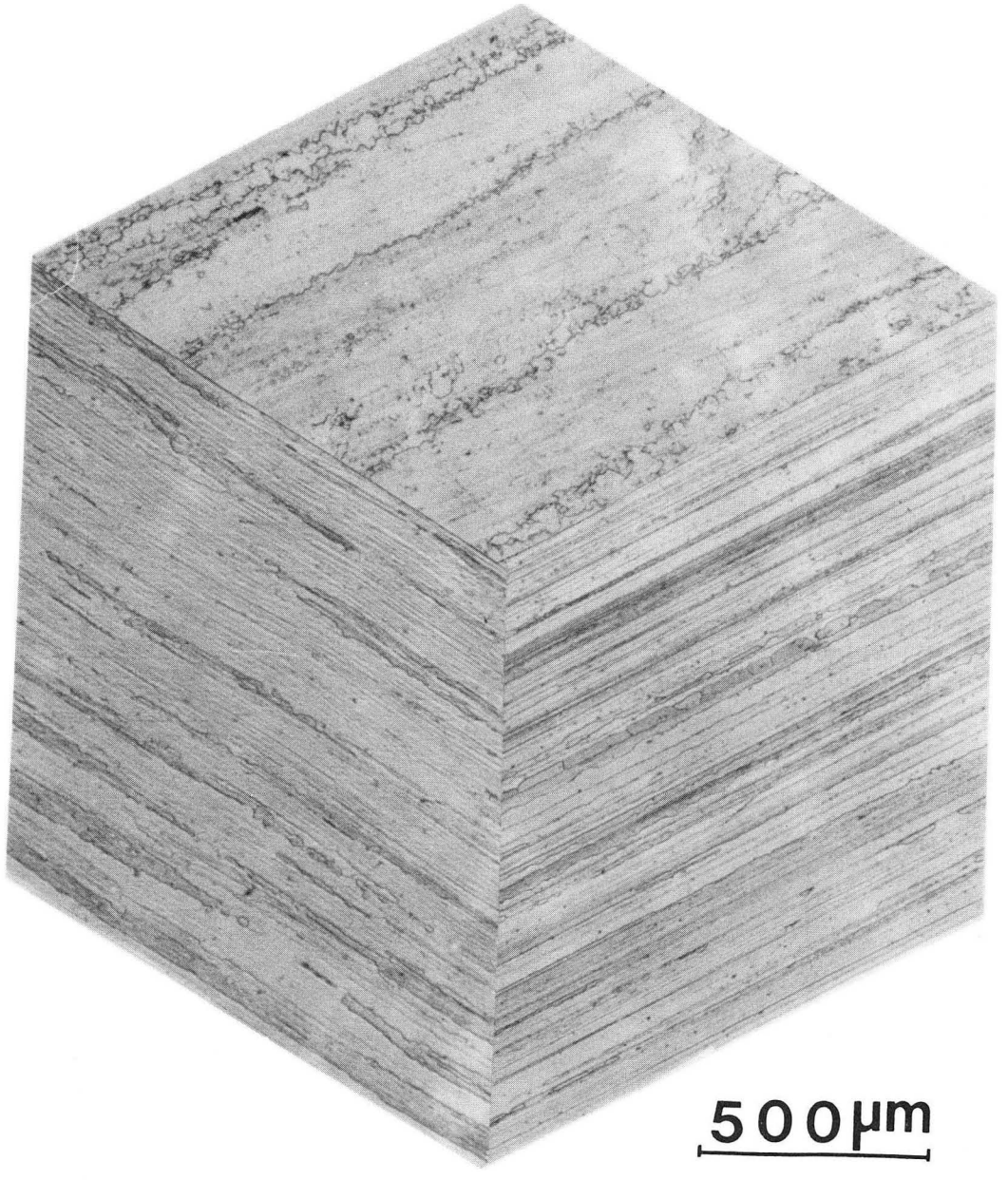

Figure 2: Composite optical micrograph showing the grain structure of Vintage I 2090-T81. (XBB 857-5875)

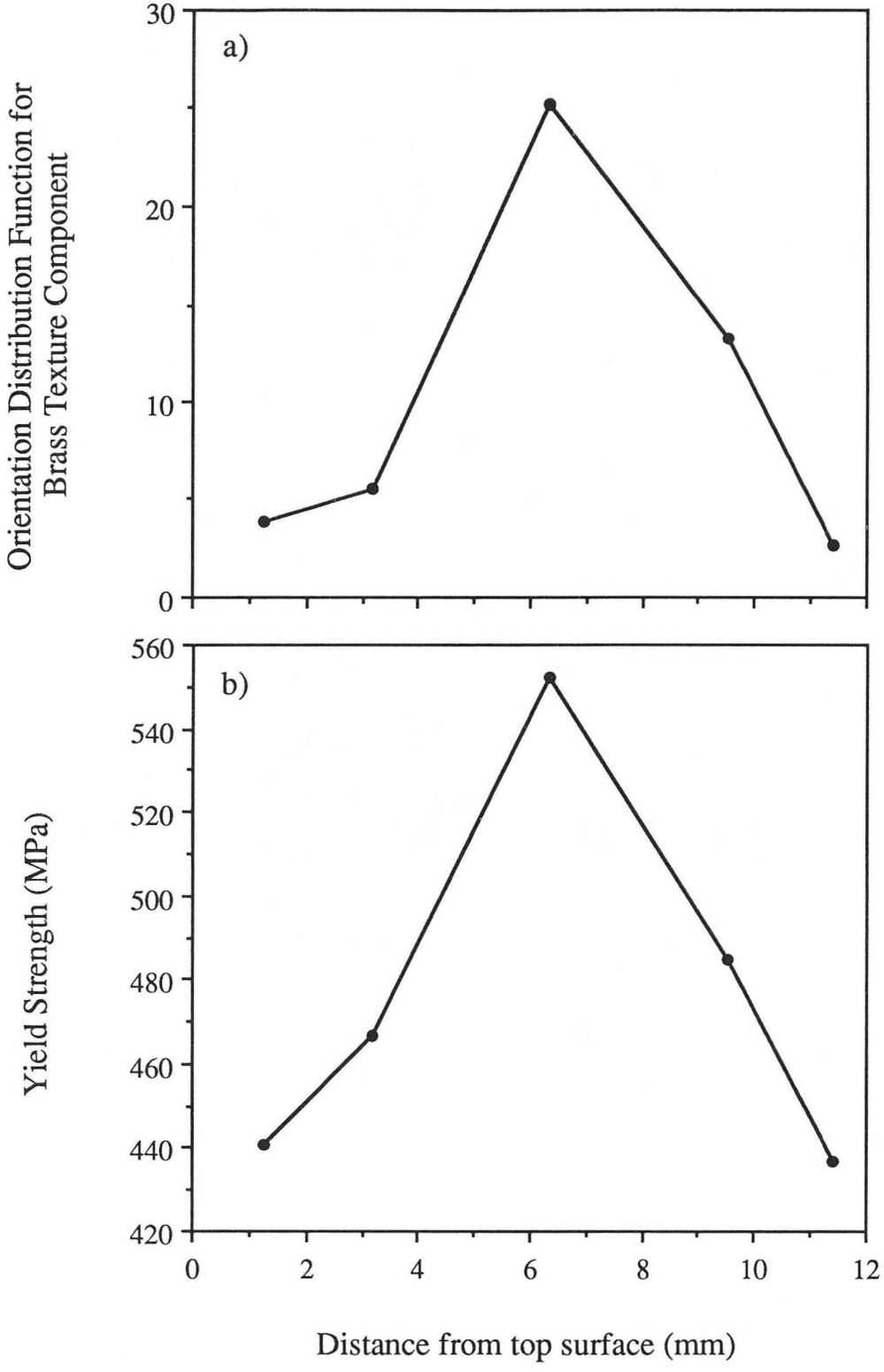

Figure 3: Plot of a) Orientation Distribution Function for Brass texture component and b) yield strength versus through-thickness position for Vintage I 2090-T81 (After Vasudevan, et al., ref. 17).

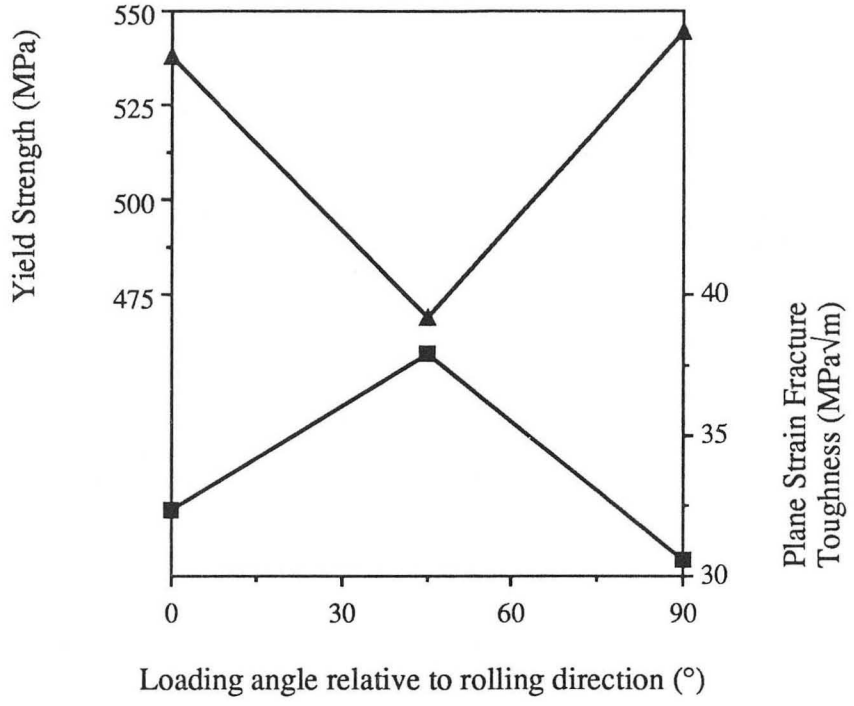

Figure 4: Plot of yield strength and plane strain fracture toughness versus in-plane orientation for Vintage I 2090-T81 (After Bucci, et al., ref. 8).

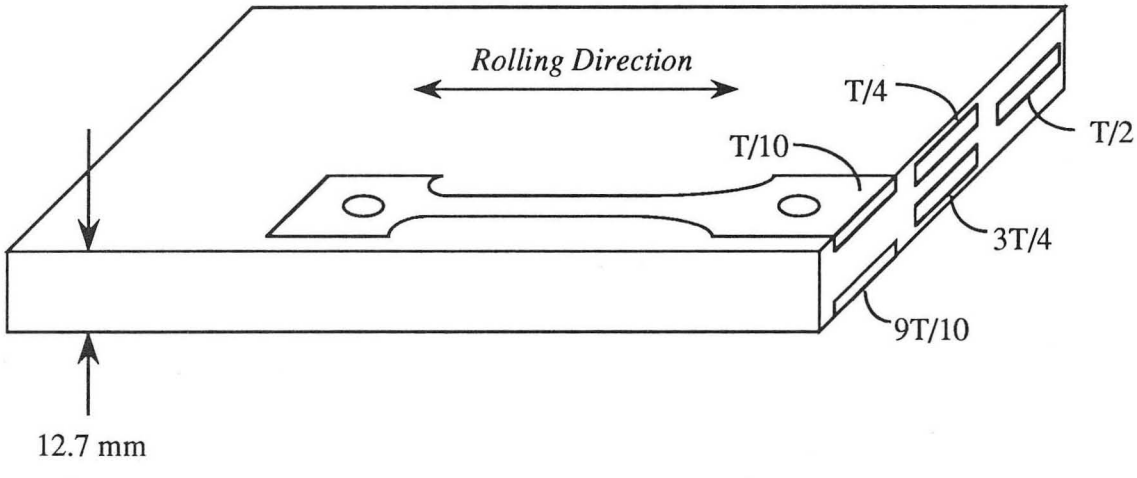

Figure 5: Schematic illustration showing the position of the through-thickness tensile specimens relative to the original plate material.

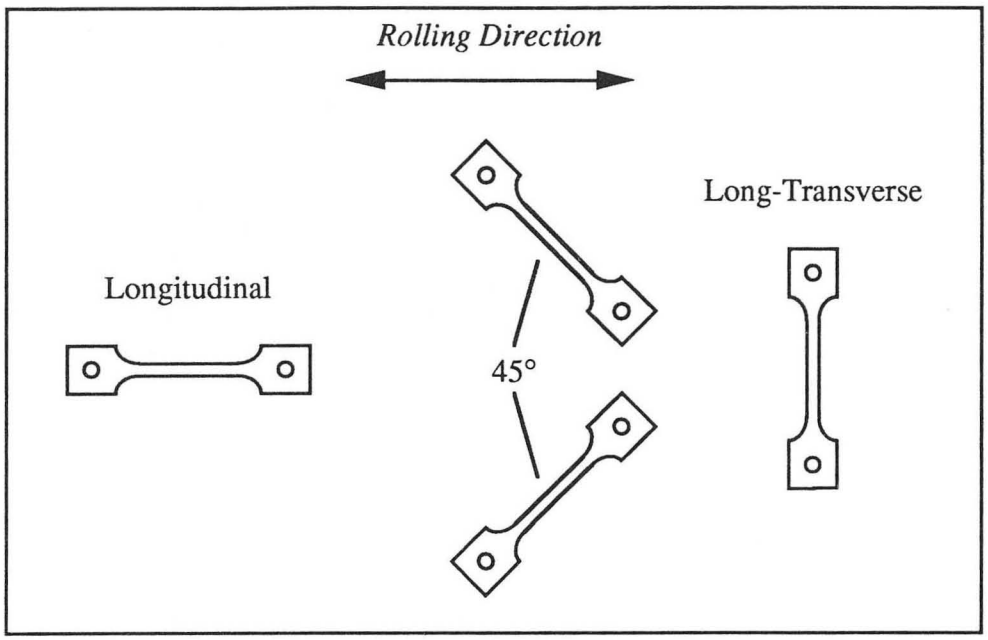

Figure 6: Schematic illustration showing the orientation of the in-plane tensile specimens relative to the original plate material.

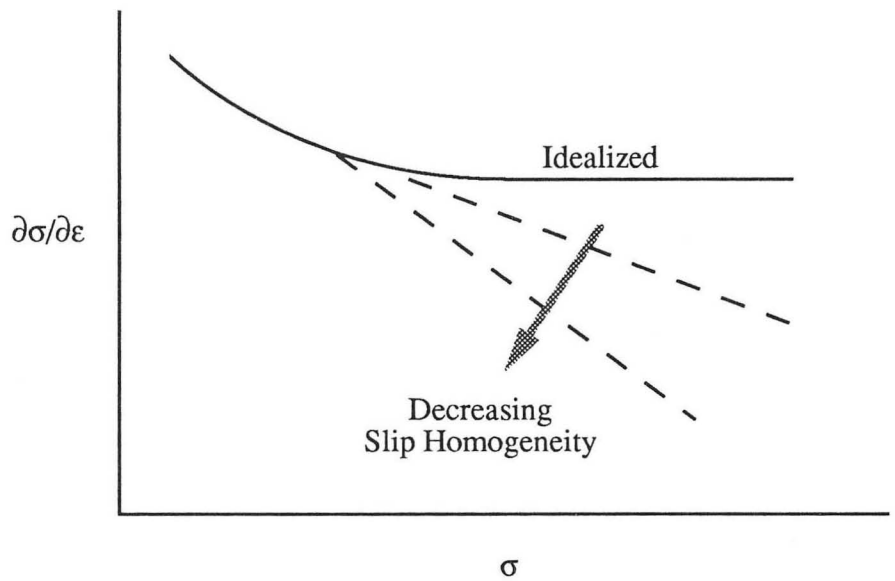

Figure 7: Schematic illustration of the idealized work hardening beahvior as a function of true stress σ for polycrystals shown in bold (After Mecking, ref. 38). Dotted line shows the conceptual deviation from zero slope of the region of stable deformation resulting from a decrease in deformation homogeneity.

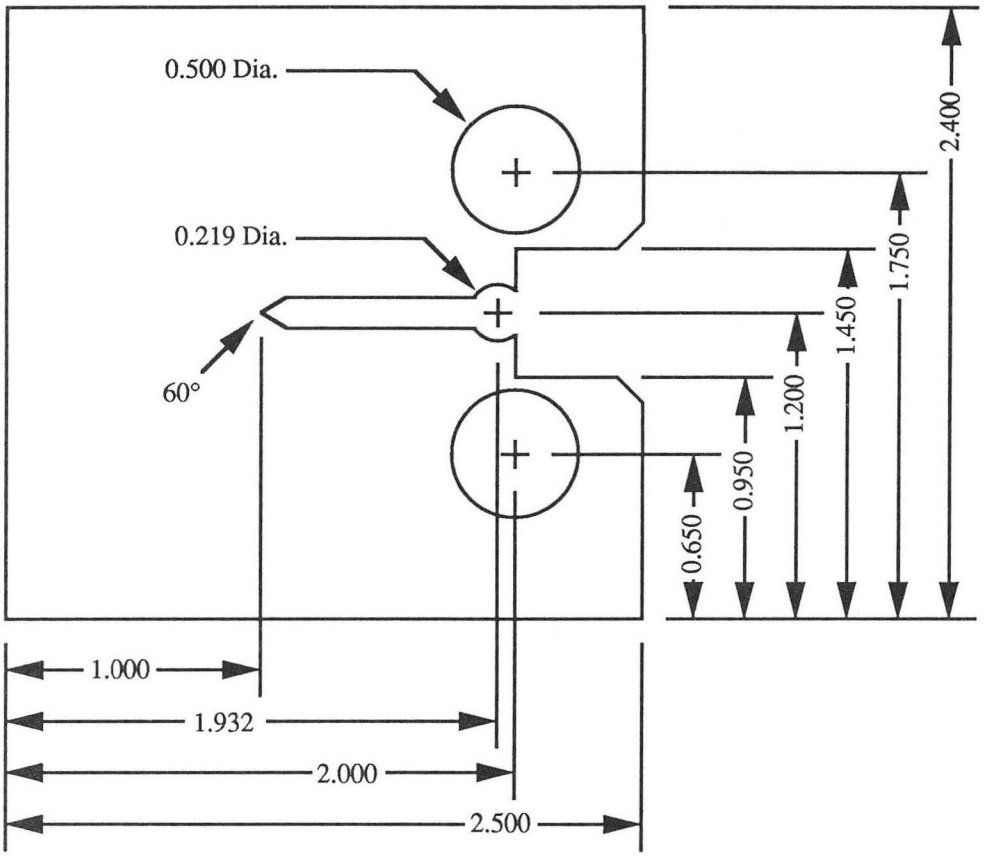

Figure 8: Schematic illustration showing the specifications of the J_{Ic} specimen. All dimensions are in inches.

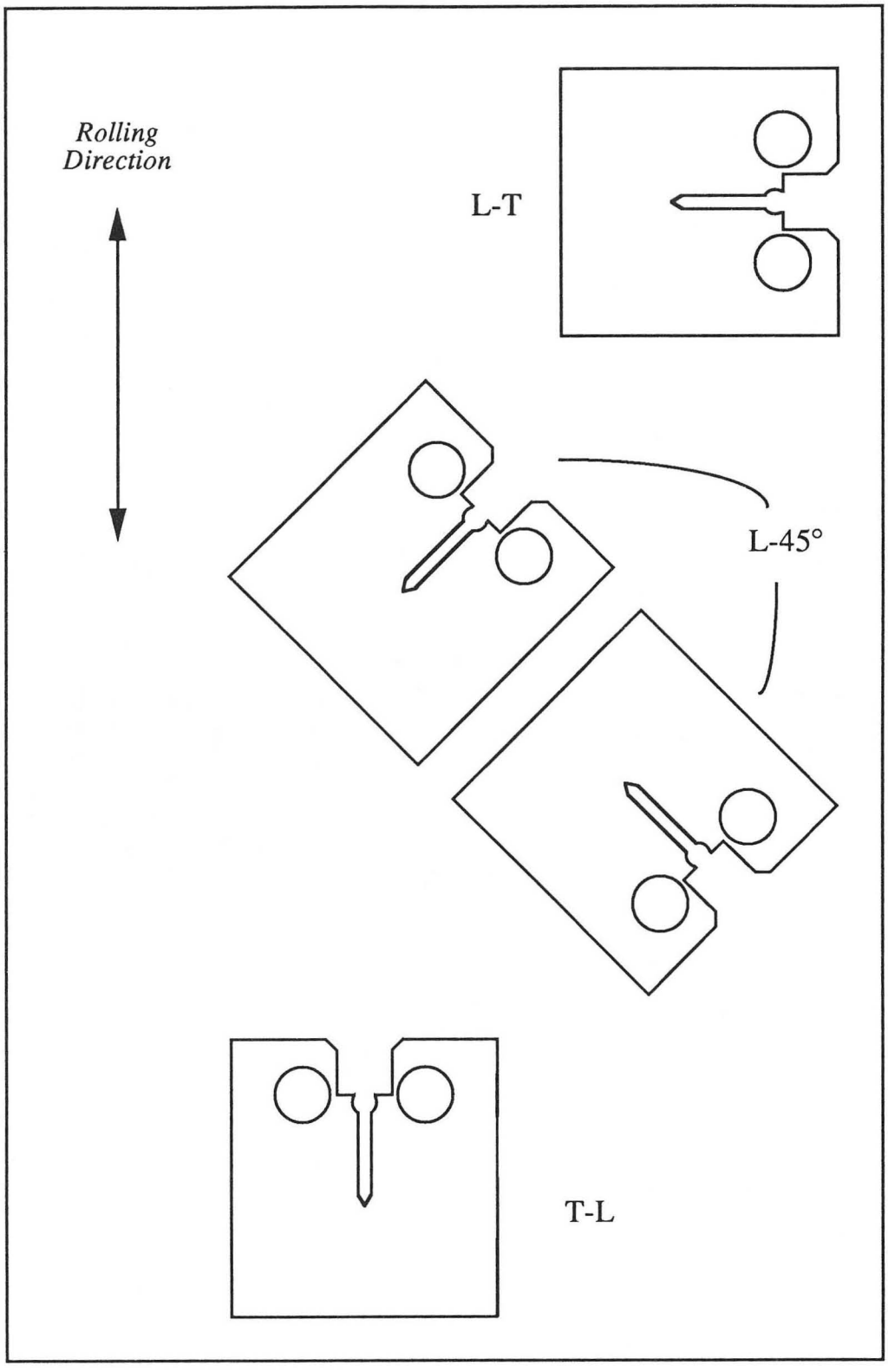

Figure 9: Schematic illustration showing the orientation and designation of J_{Ic} specimens relative to the original plate material.

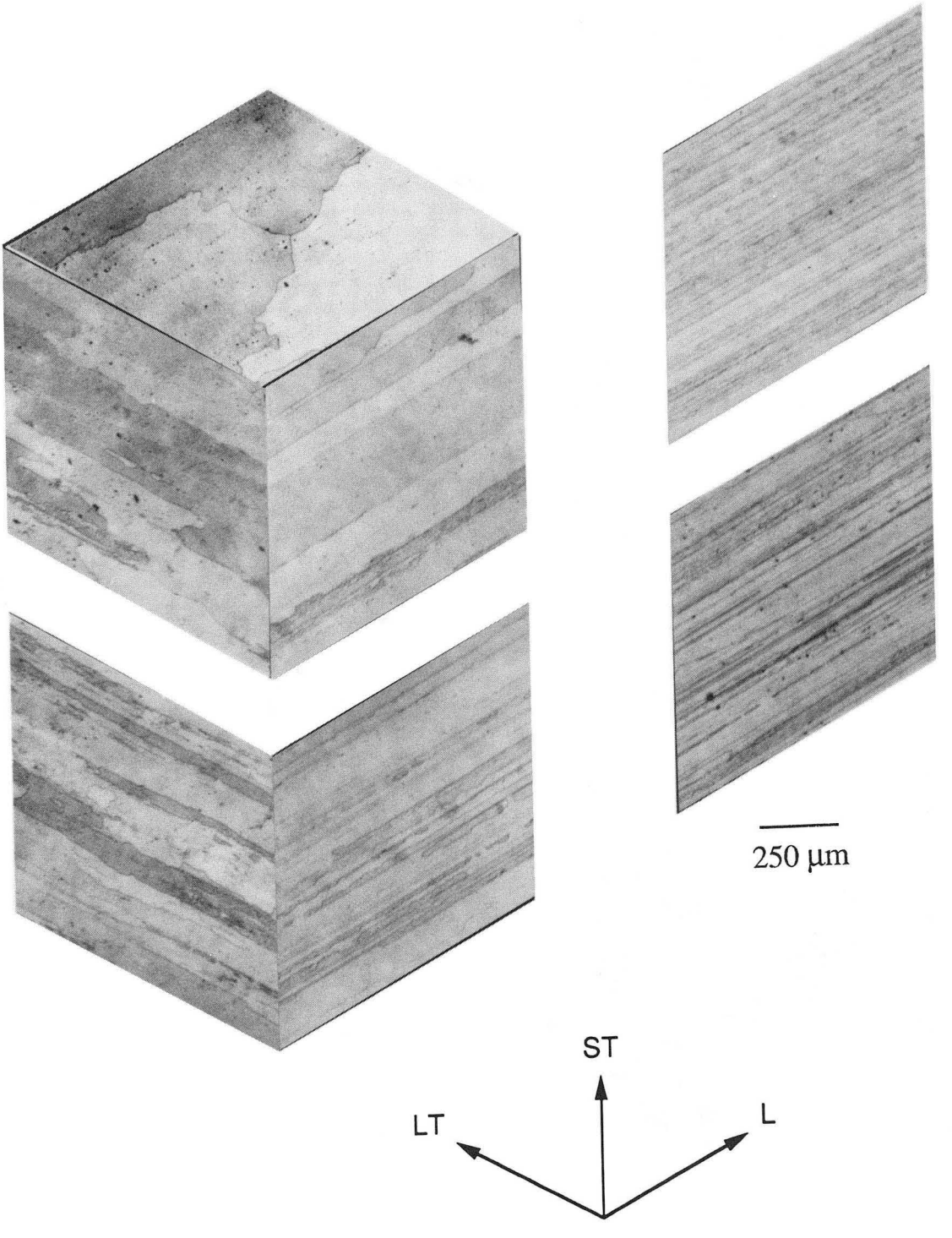

Figure 10: Optical micrographs comparing the microstructures of Vintage I (on right) and Vintage III 2090-T81 (on left). Upper micrographs are taken at quarter-thickness, lower micrographs at mid-thickness. Note the larger grains and greater variation in grain size of the Vintage III material. (XBB 898-6771)

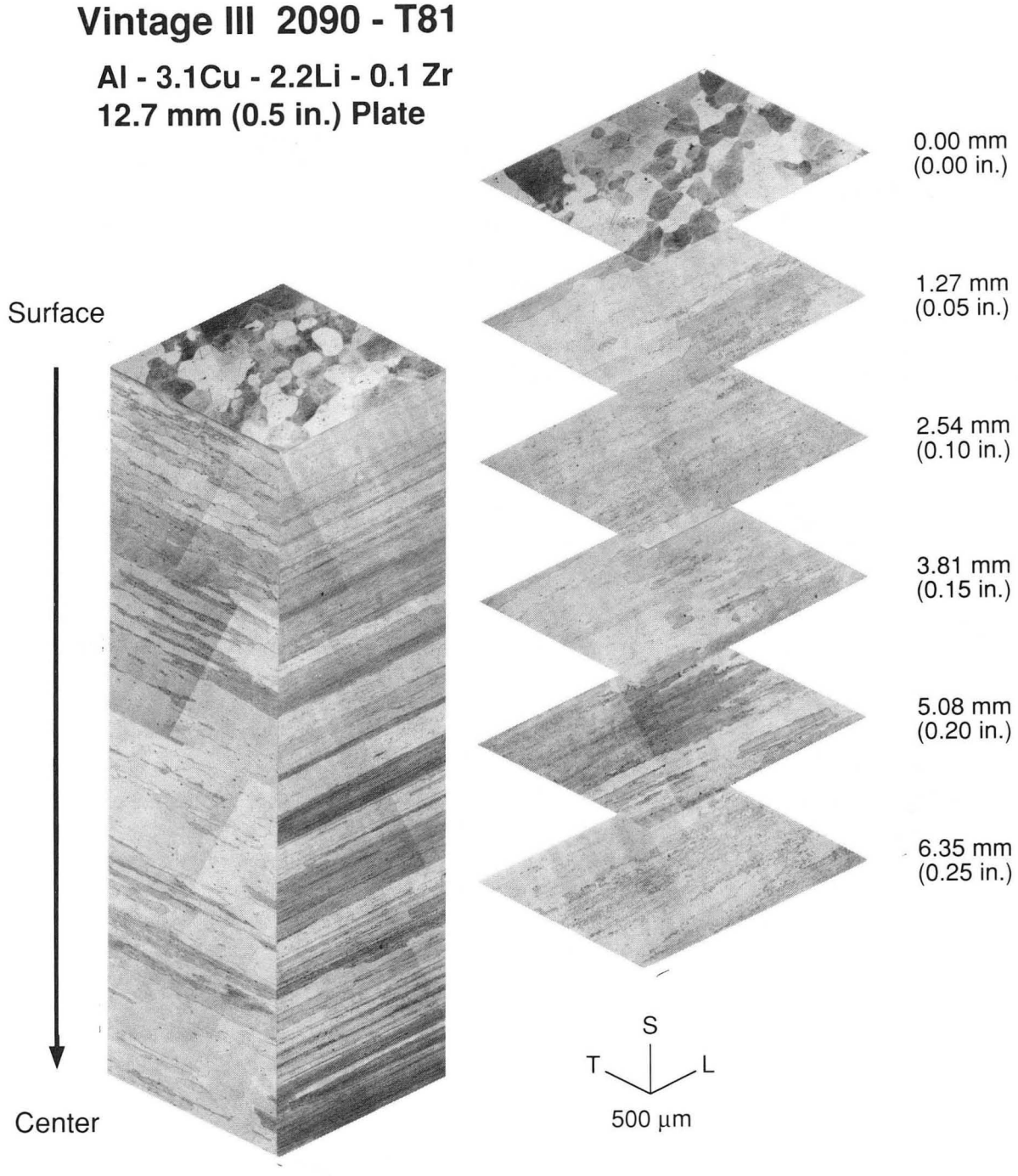

Figure 11: Optical micrographs showing the microstructure from the top surface to mid-thickness of Vintage III 2090-T81. (XBB 902-882)

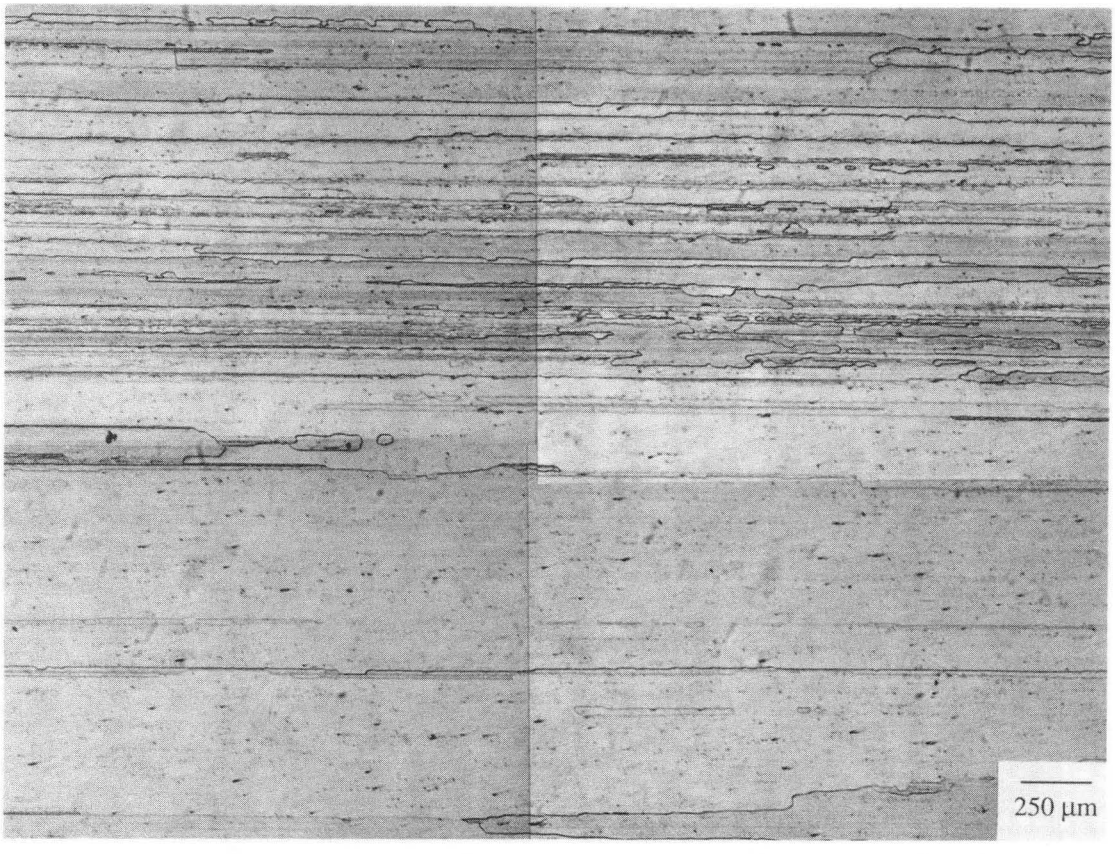

Figure 12: Optical micrographs showing the boundary between relatively thin grains near mid-thickness and thicker grains below. (XBB 906-5007)

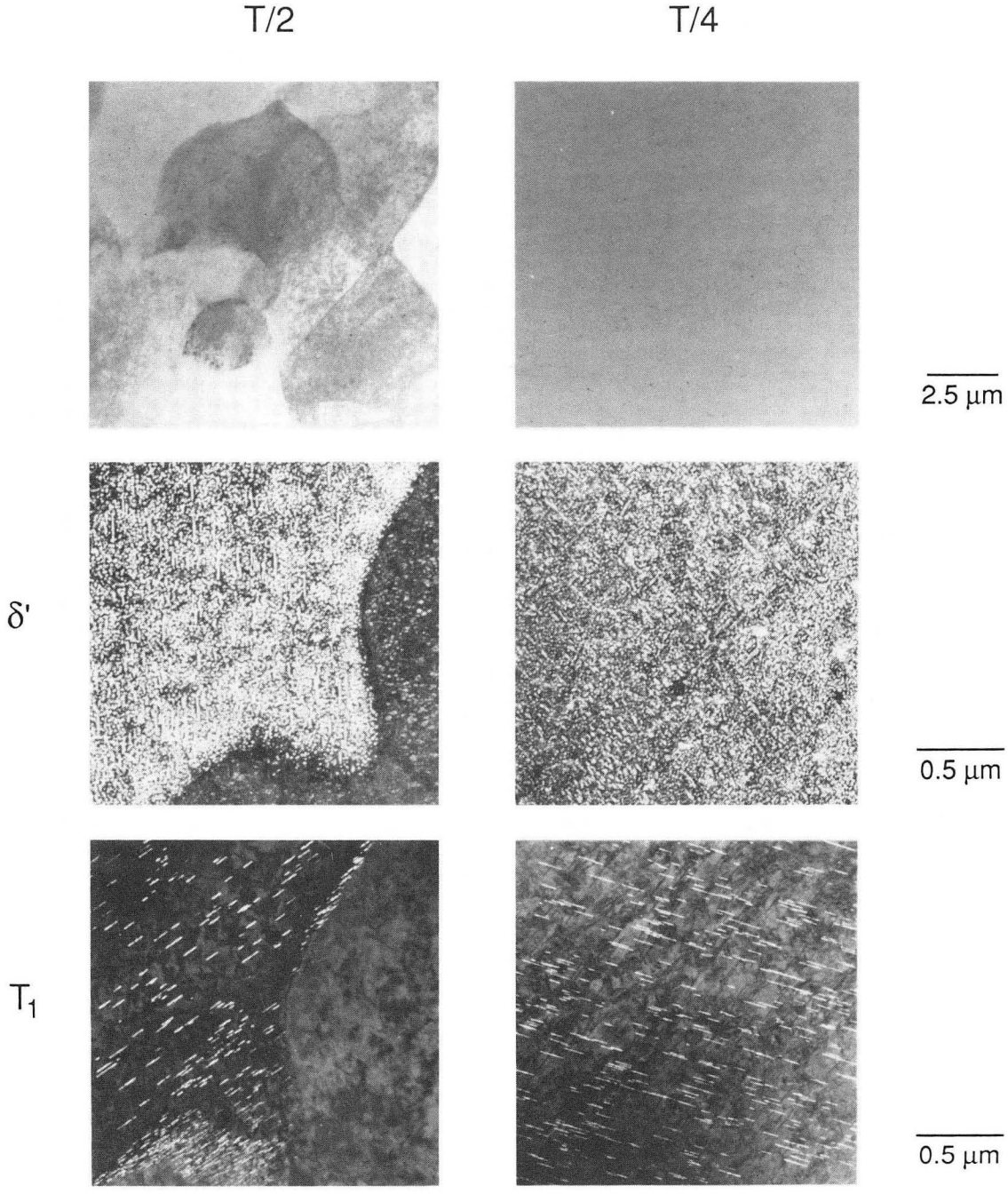

Figure 13: Bright field transmission electron micrographs (top) and dark field images showing the distribution of δ' and one variant of T_1. (XBB 902-1151)

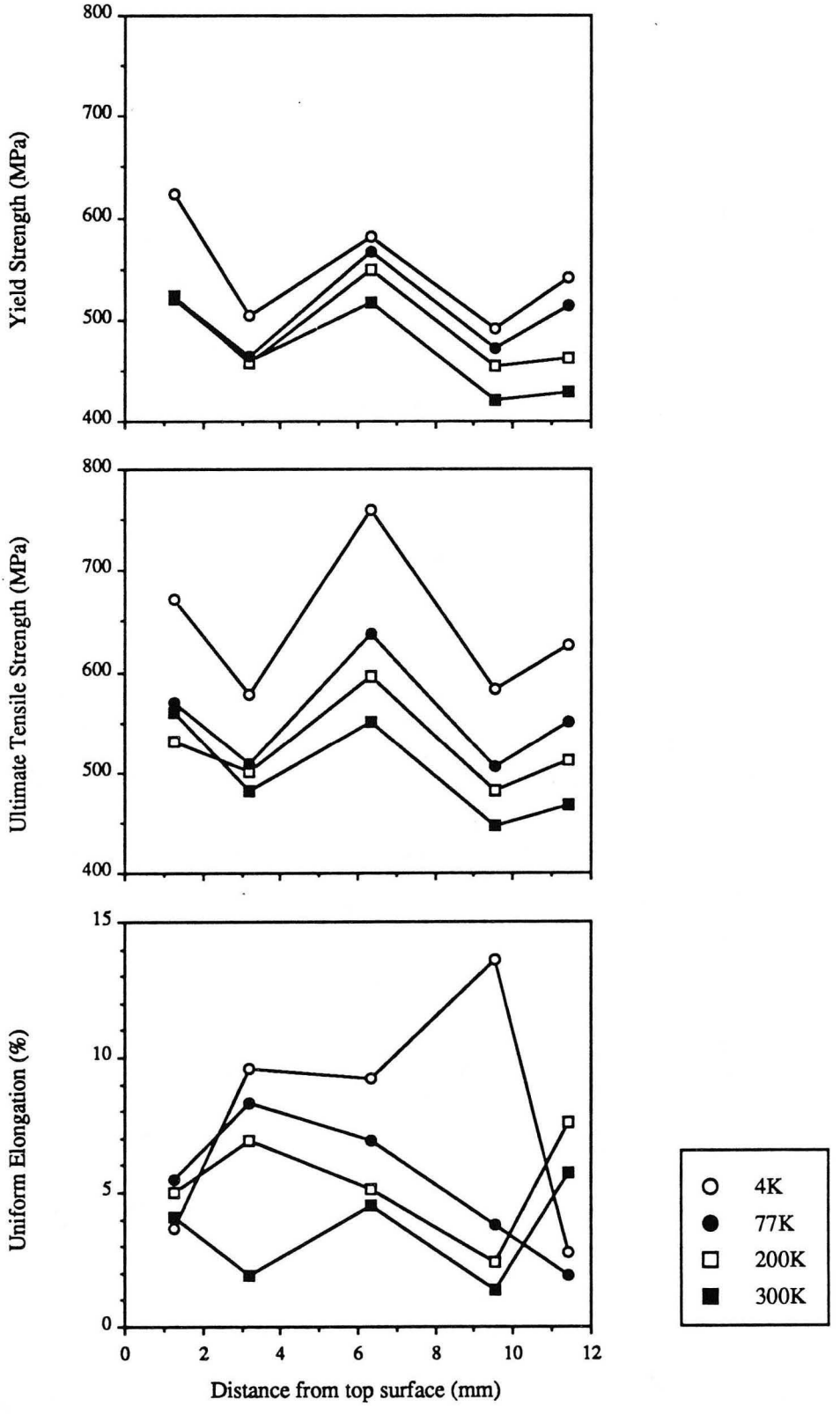

Figure 14: Variation of the a) yield strength, b) ultimate tensile strength, and c) uniform elongation with through-thickness position for Vintage III 2090-T81 longitudinal tensile specimens.

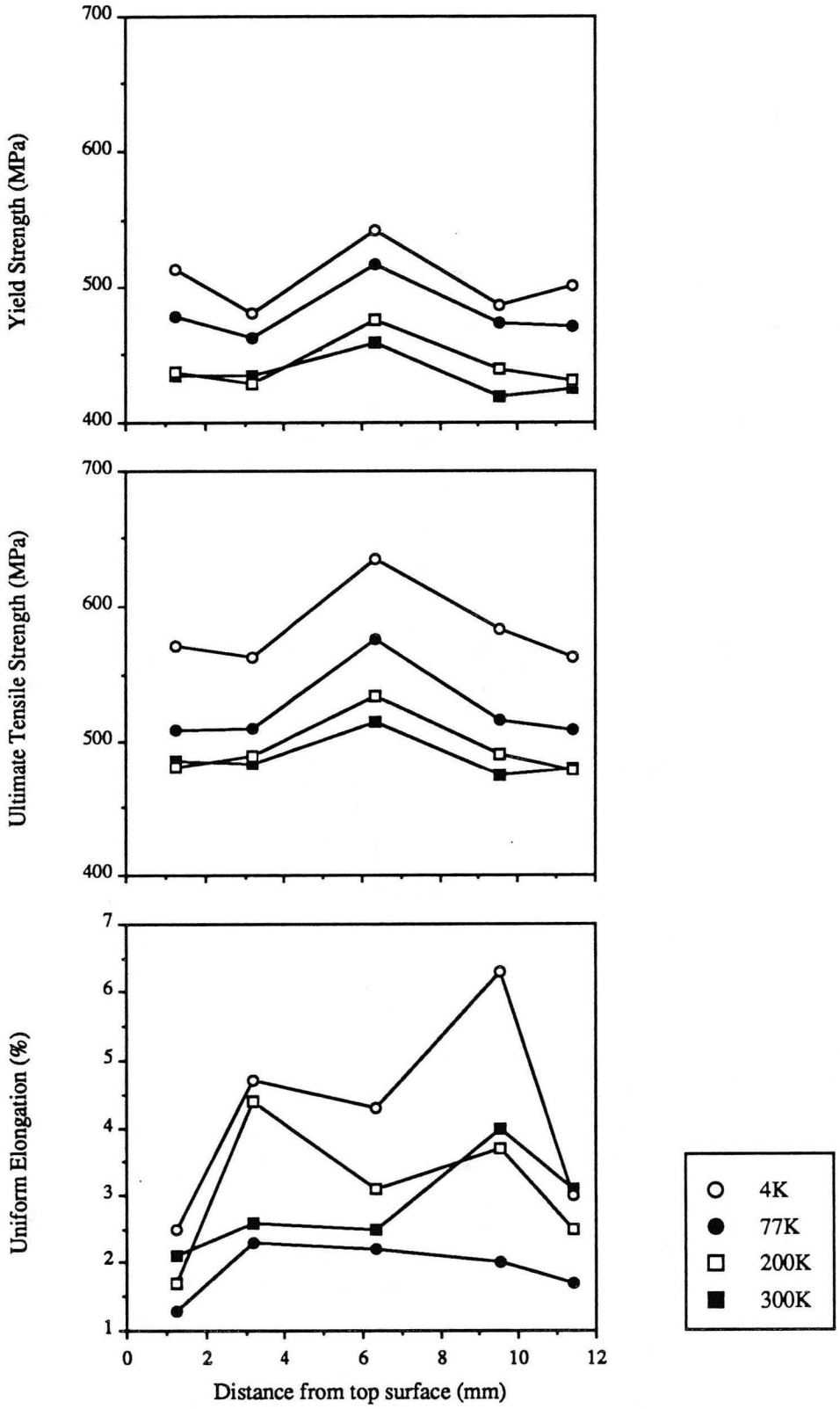

Figure 15: Variation of the a) yield strength, b) ultimate tensile strength, and c) uniform elongation with through-thickness position for Vintage III 2090-T81 45° tensile specimens.

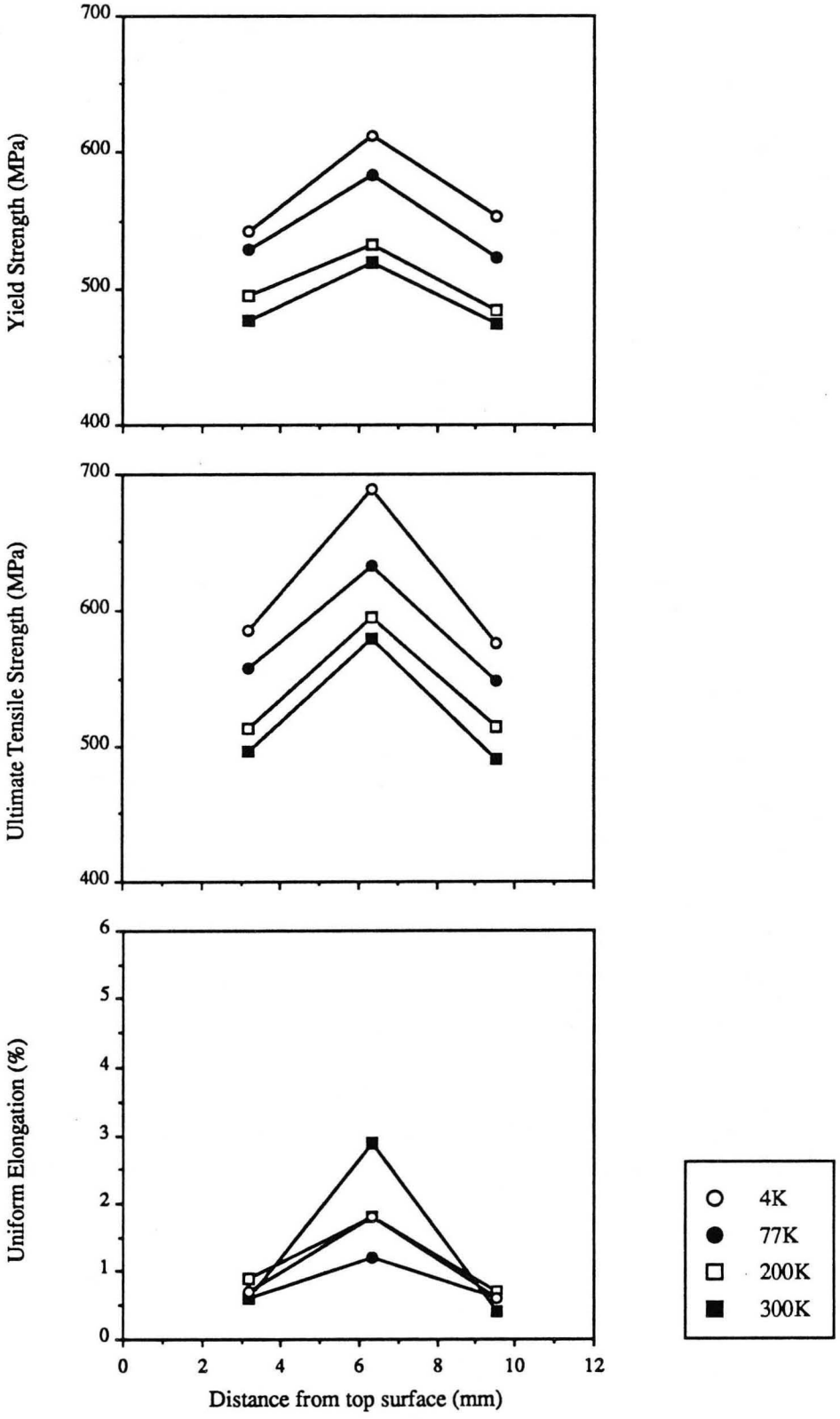

Figure 16: Variation of the a) yield strength, b) ultimate tensile strength, and c) uniform elongation with through-thickness position for Vintage III 2090-T81 long-transverse tensile specimens.

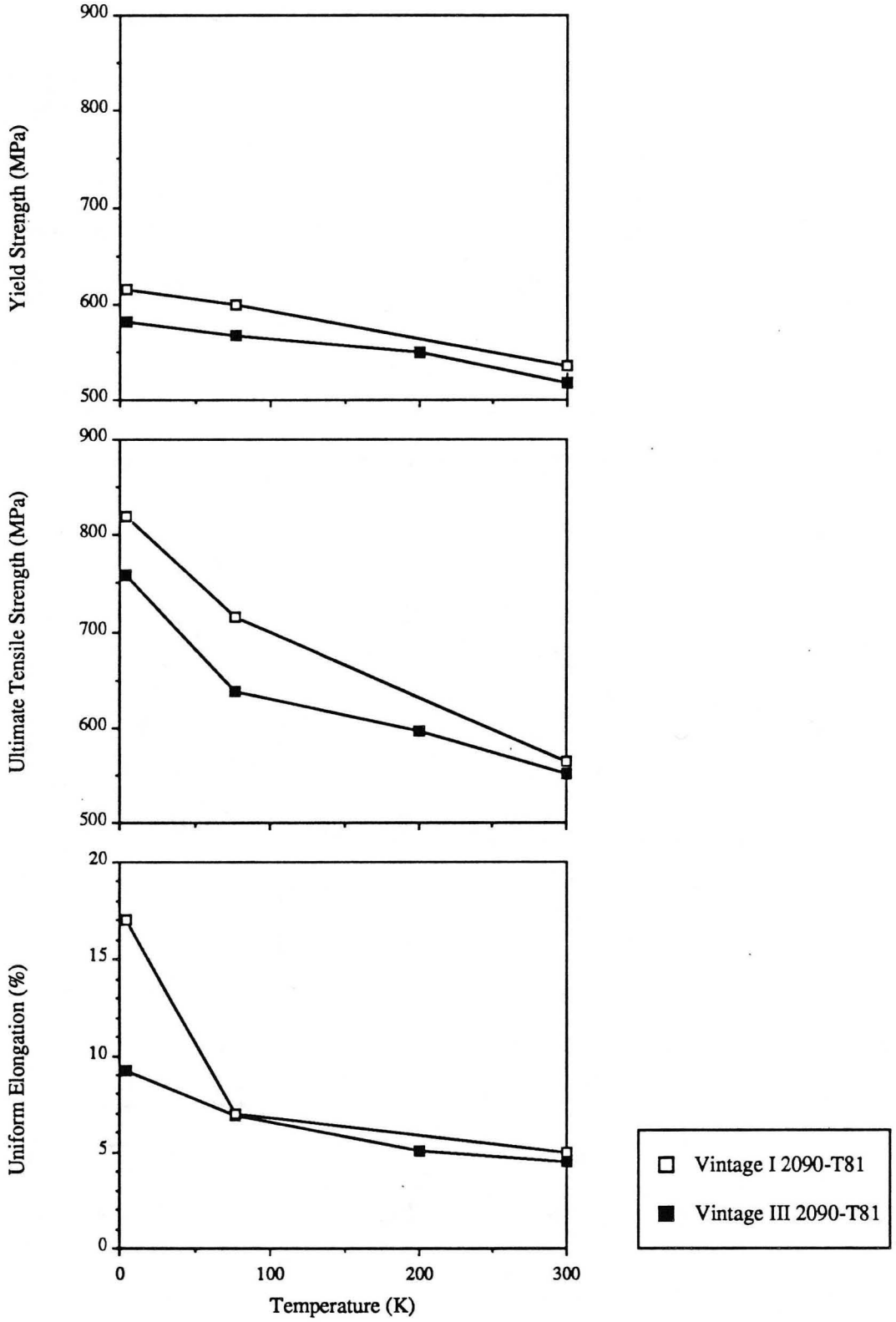

Figure 17: Comparison of the a) yield strength, b) ultimate tensile strength, and c) uniform elongation as a function of temperature for Vintage I and Vintage III 2090-T81 longitudinal tensile specimens taken at mid-thickness.

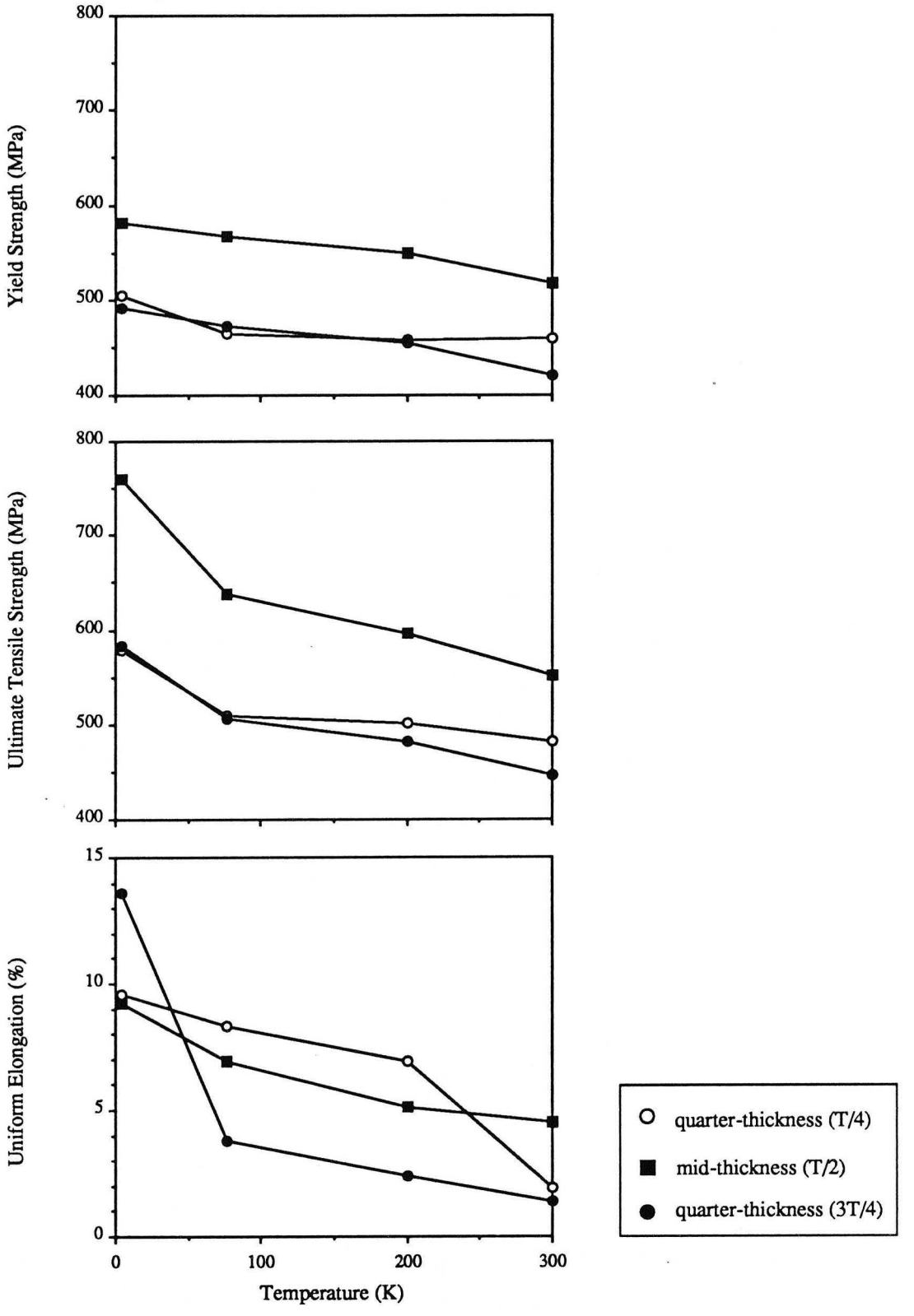

Figure 18: Comparison of the a) yield strength, b) ultimate tensile strength, and c) uniform elongation as a function of temperature for Vintage III 2090-T81 longitudinal tensile specimens taken at mid-thickness and quarter-thickness.

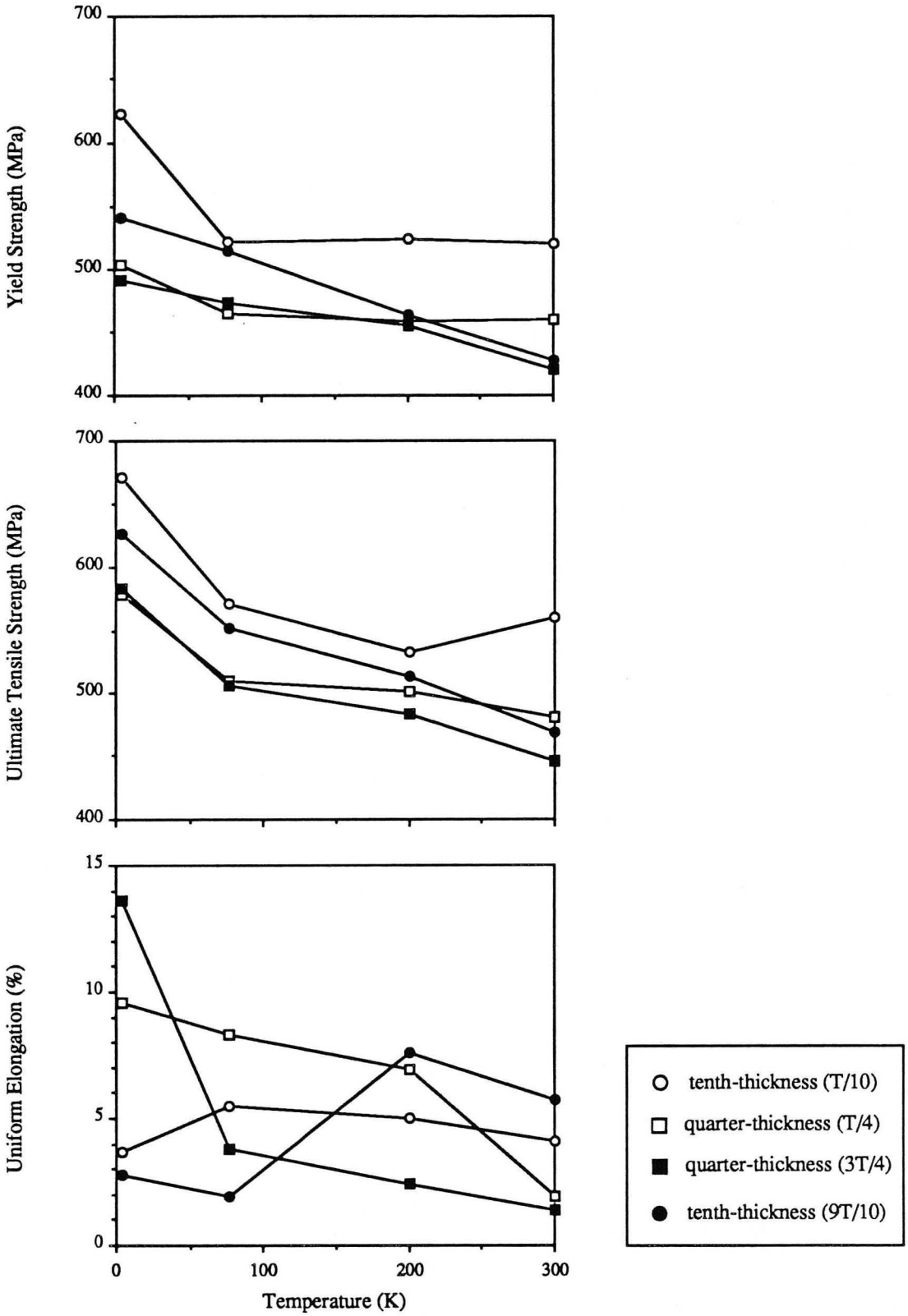

Figure 19: Comparison of the a) yield strength, b) ultimate tensile strength, and c) uniform elongation as a function of temperature for Vintage III 2090-T81 longitudinal tensile specimens taken at quarter-thickness and tenth-thickness.

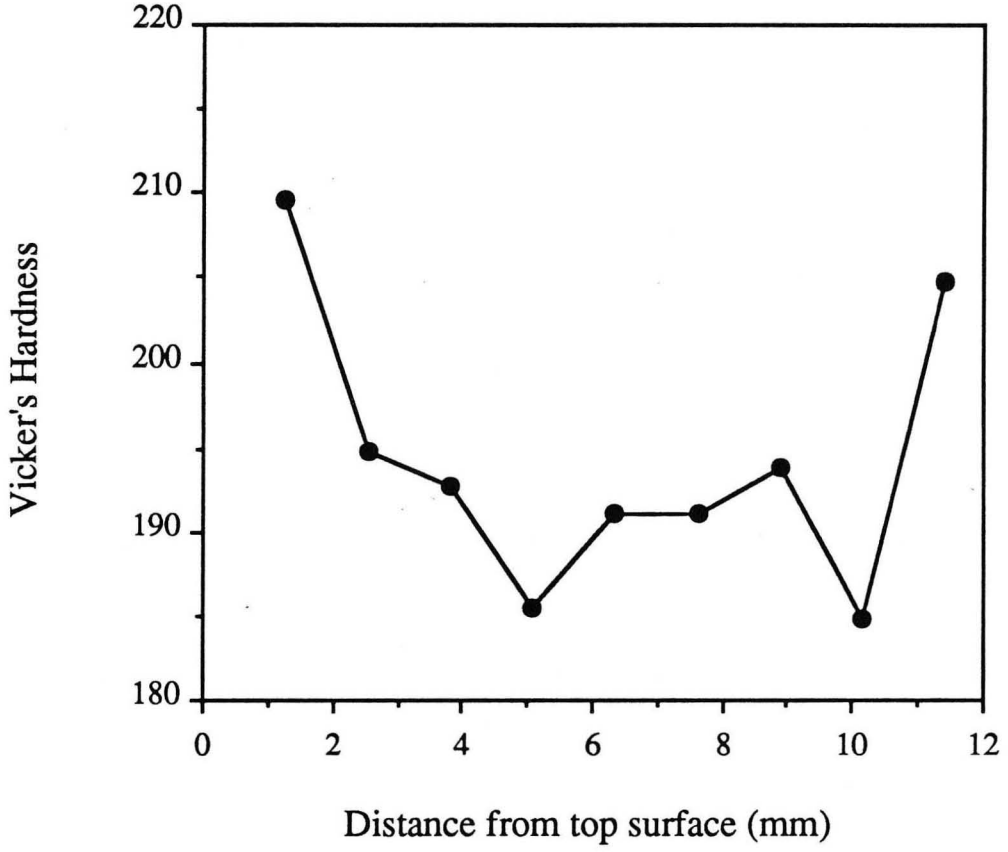

Figure 20: Variation of the microhardness with through-thickness position for Vintage III 2090-T81. Note that the apparent center of symmetry deviates from the geometric center of the plate.

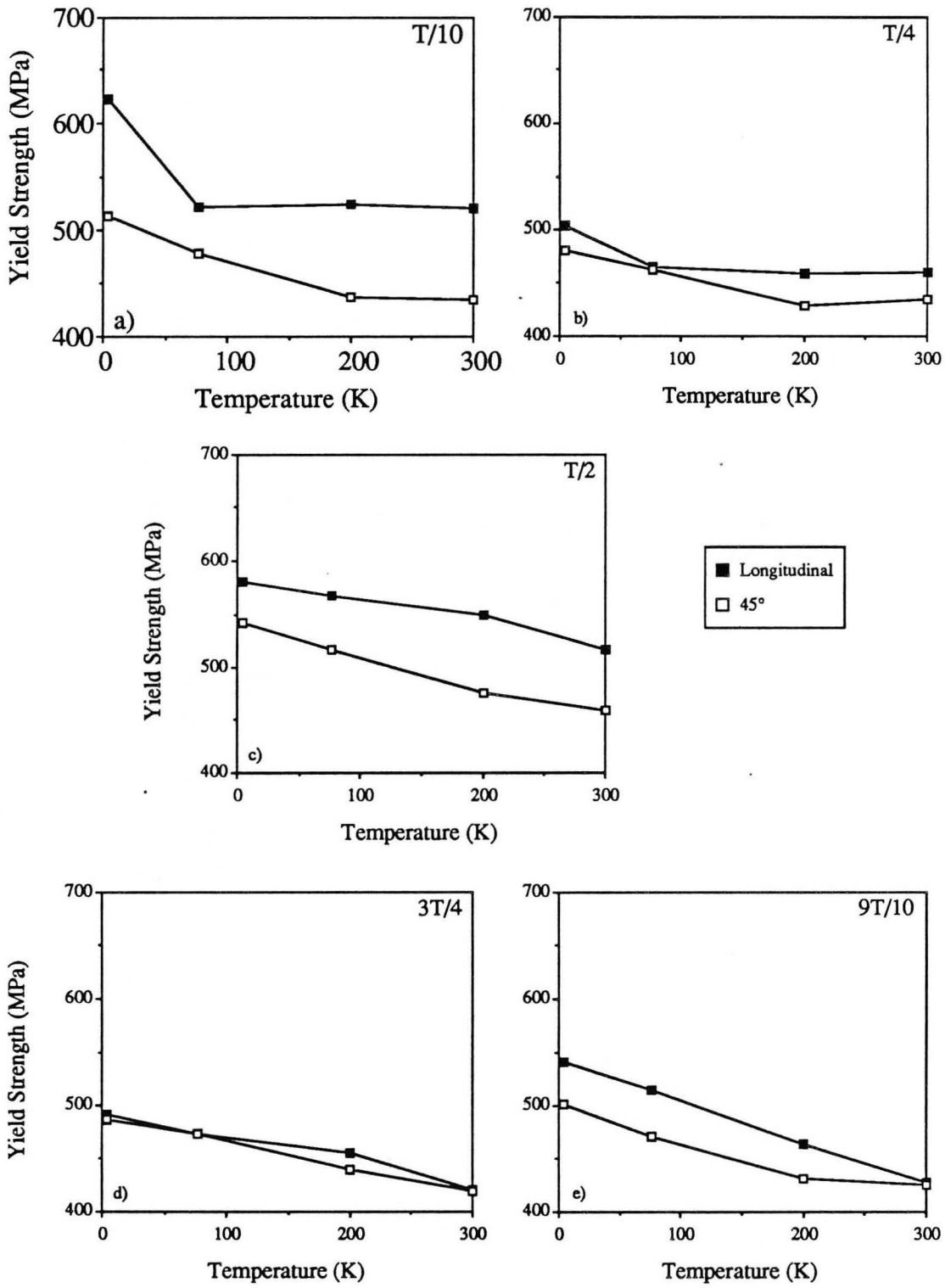

Figure 21: Comparison of the yield strength as a function of temperature for Vintage III 2090-T81 longitudinal and 45° tensile specimens taken at a) T/10, b) T/4, c) T/2, d) 3T/4, and e) 9T/10.

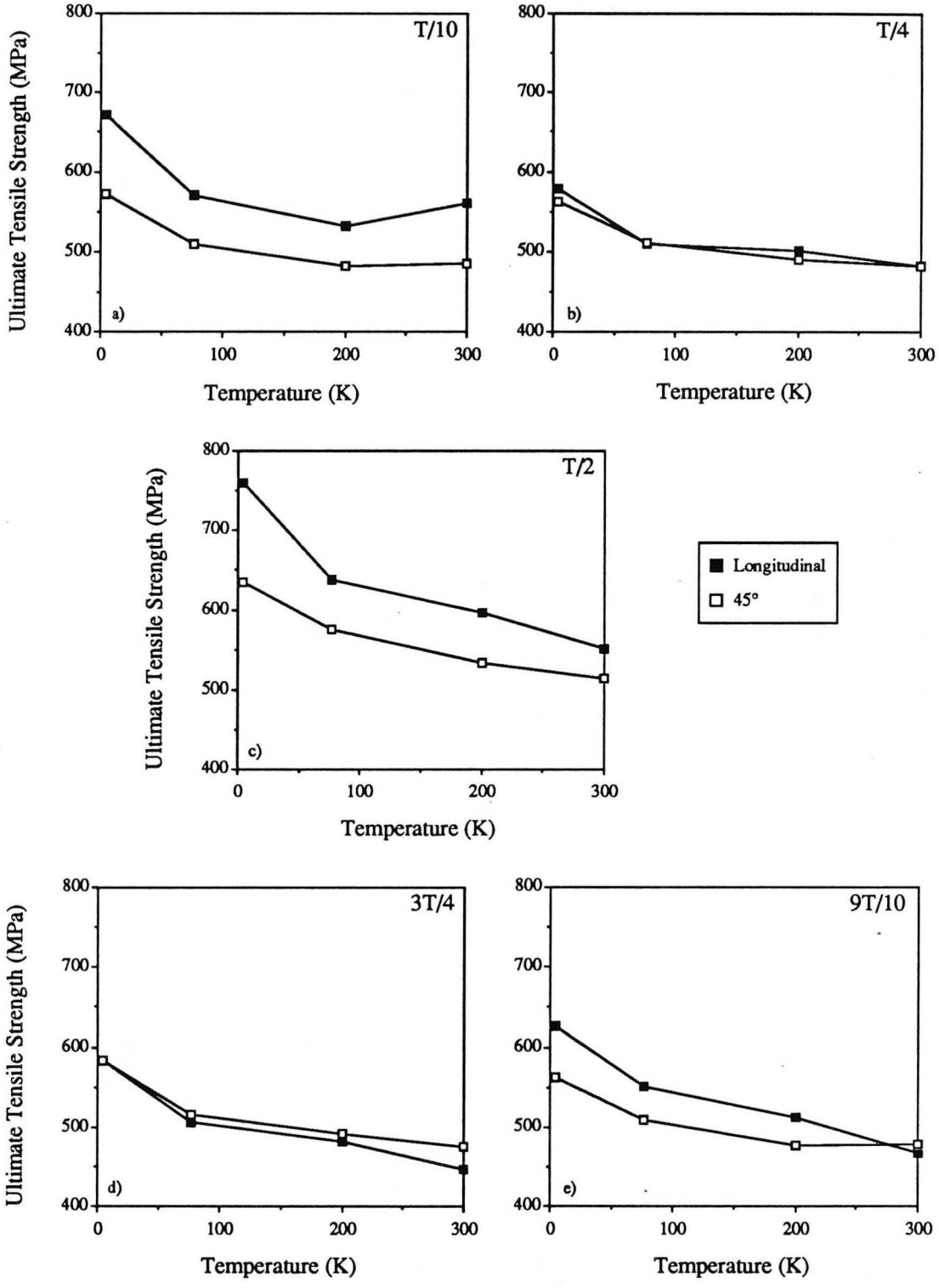

Figure 22: Comparison of the ultimate tensile strength as a function of temperature for Vintage III 2090-T81 longitudinal and 45° tensile specimens taken at a) T/10, b) T/4, c) T/2, d) 3T/4, and e) 9T/10.

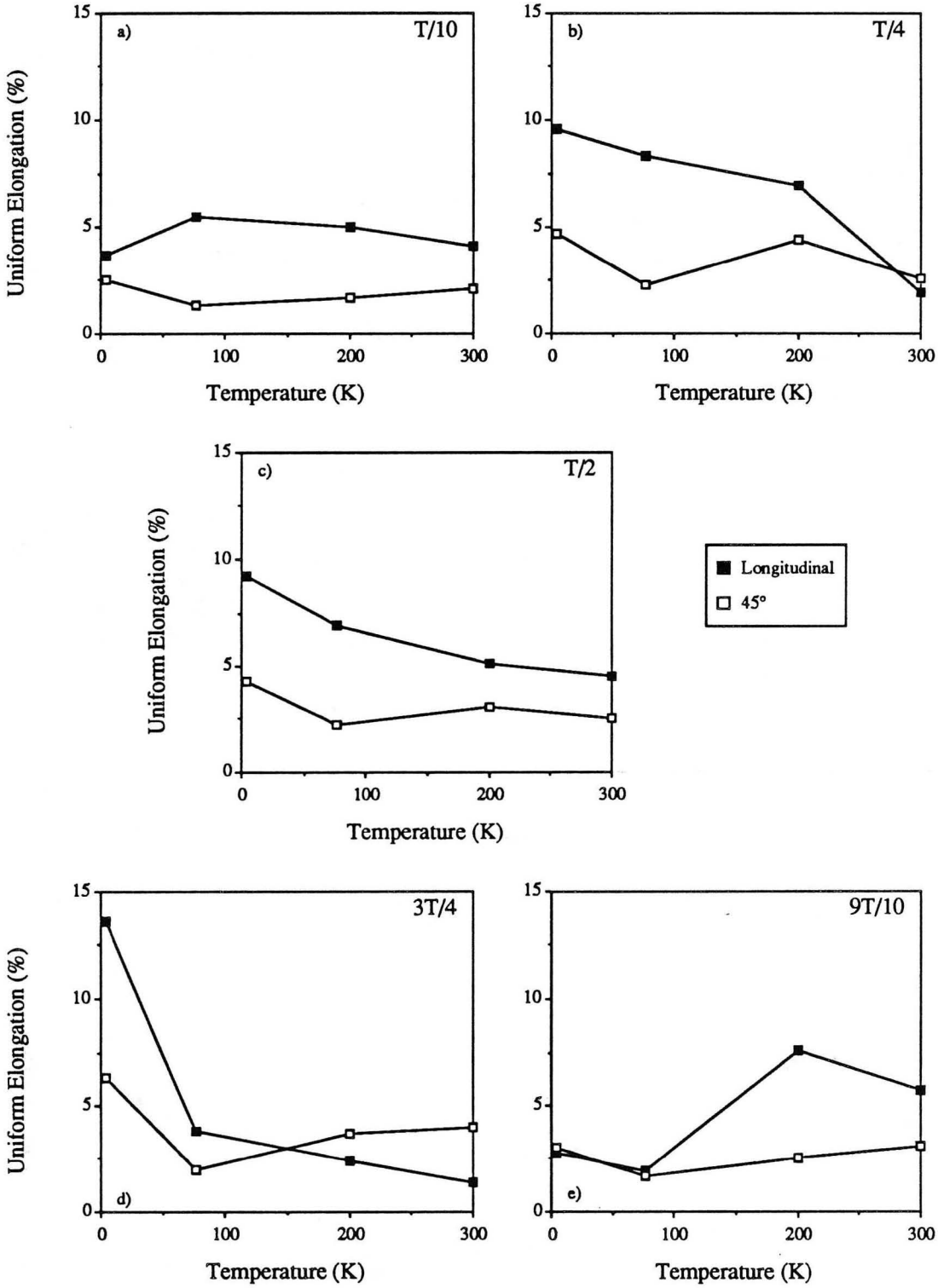

Figure 23: Comparison of the uniform elongation as a function of temperature for Vintage III 2090-T81 longitudinal and 45° tensile specimens taken at a) T/10, b) T/4, c) T/2, d) 3T/4, and e) 9T/10.

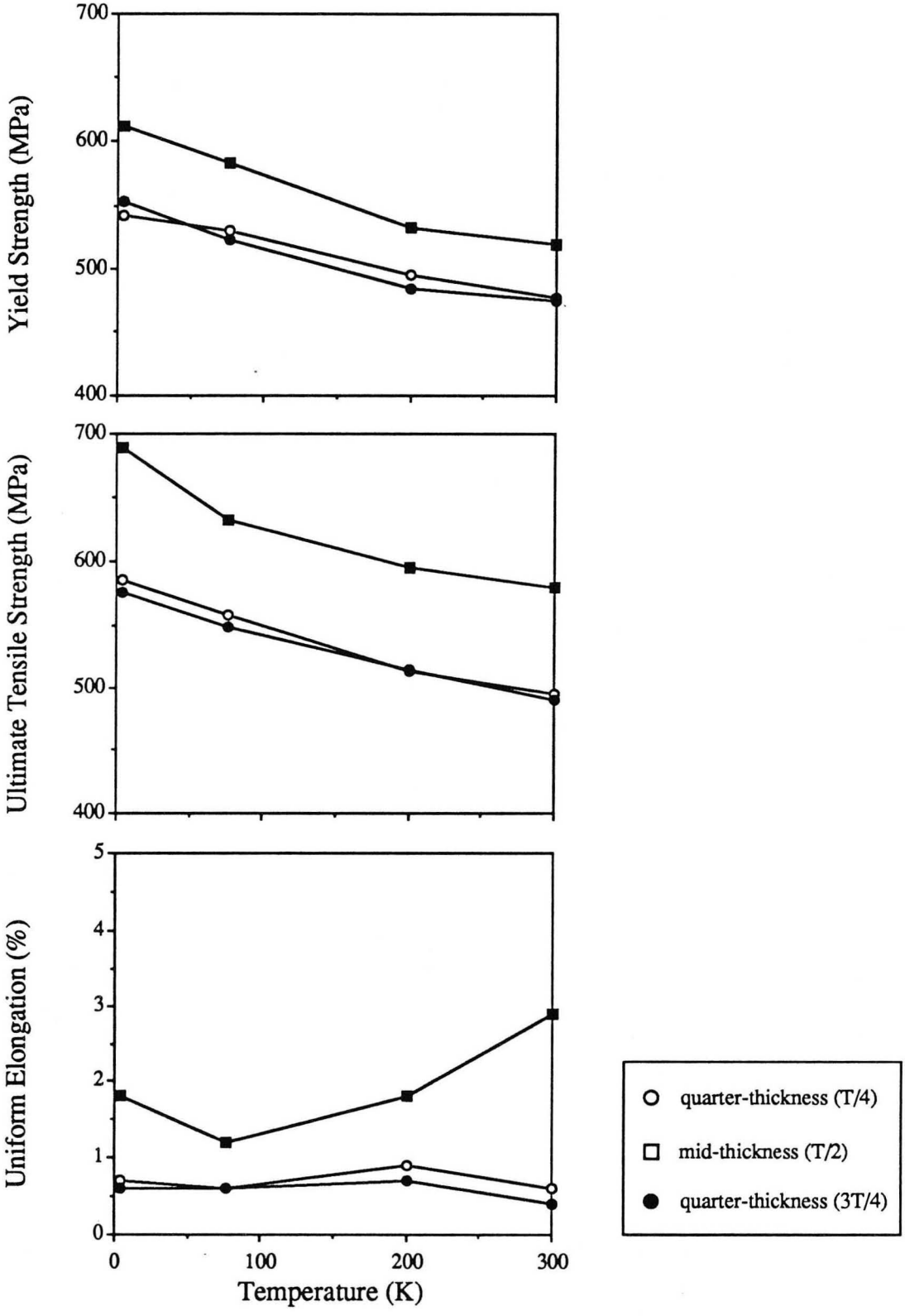

Figure 24: Variation of the a) yield strength, b) ultimate tensile strength, and c) uniform elongation as a function of temperature for Vintage III 2090-T81 long-transverse tensile specimens taken at mid-thickness and quarter-thickness.

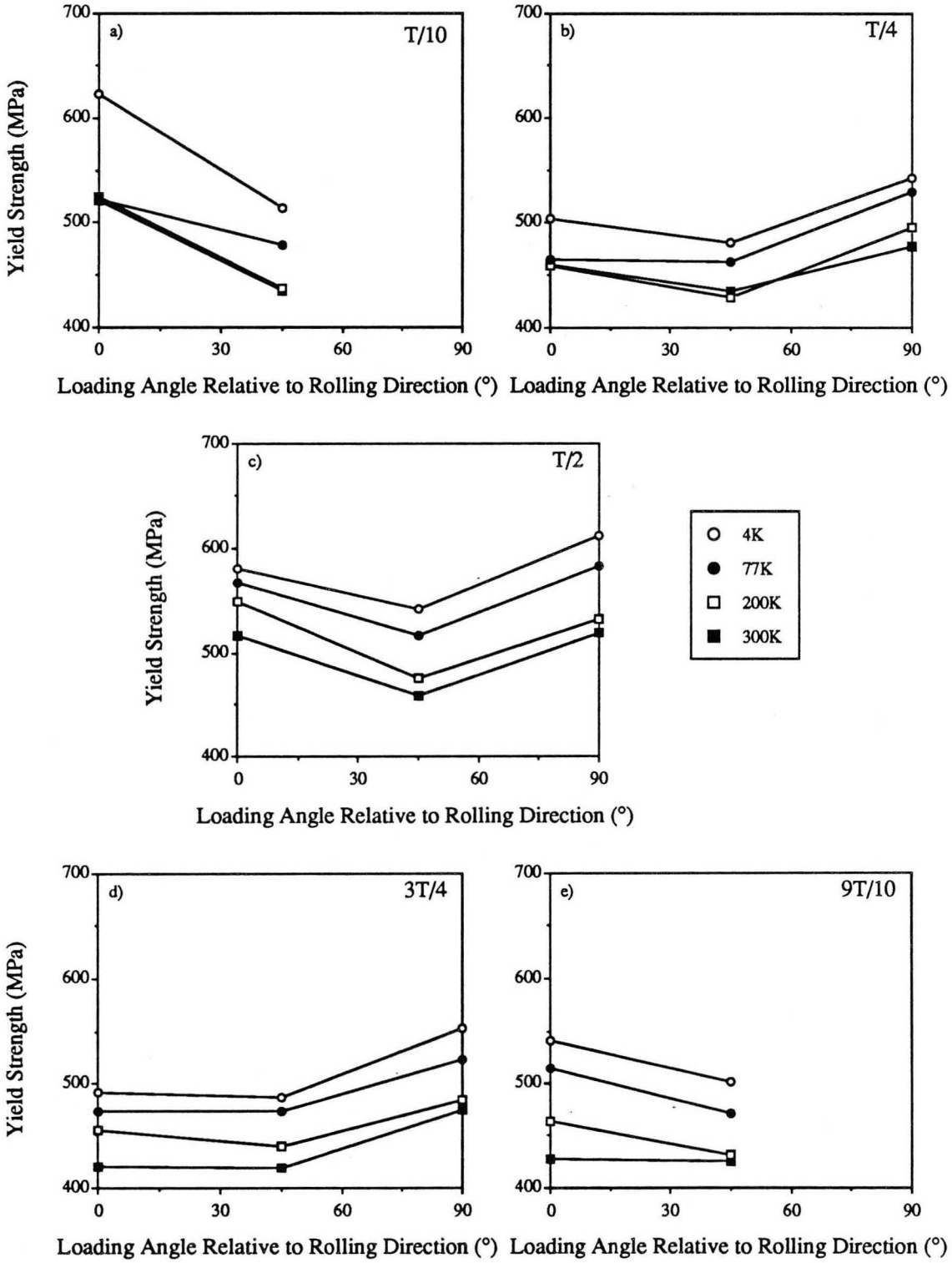

Figure 25: Variation of the yield strength with orientation for Vintage III 2090-T81 tensile specimens taken at a) T/10, b) T/4, c) T/2, d) 3T/4, and e) 9T/10 and tested at 300K, 200K, 77K, and 4K.

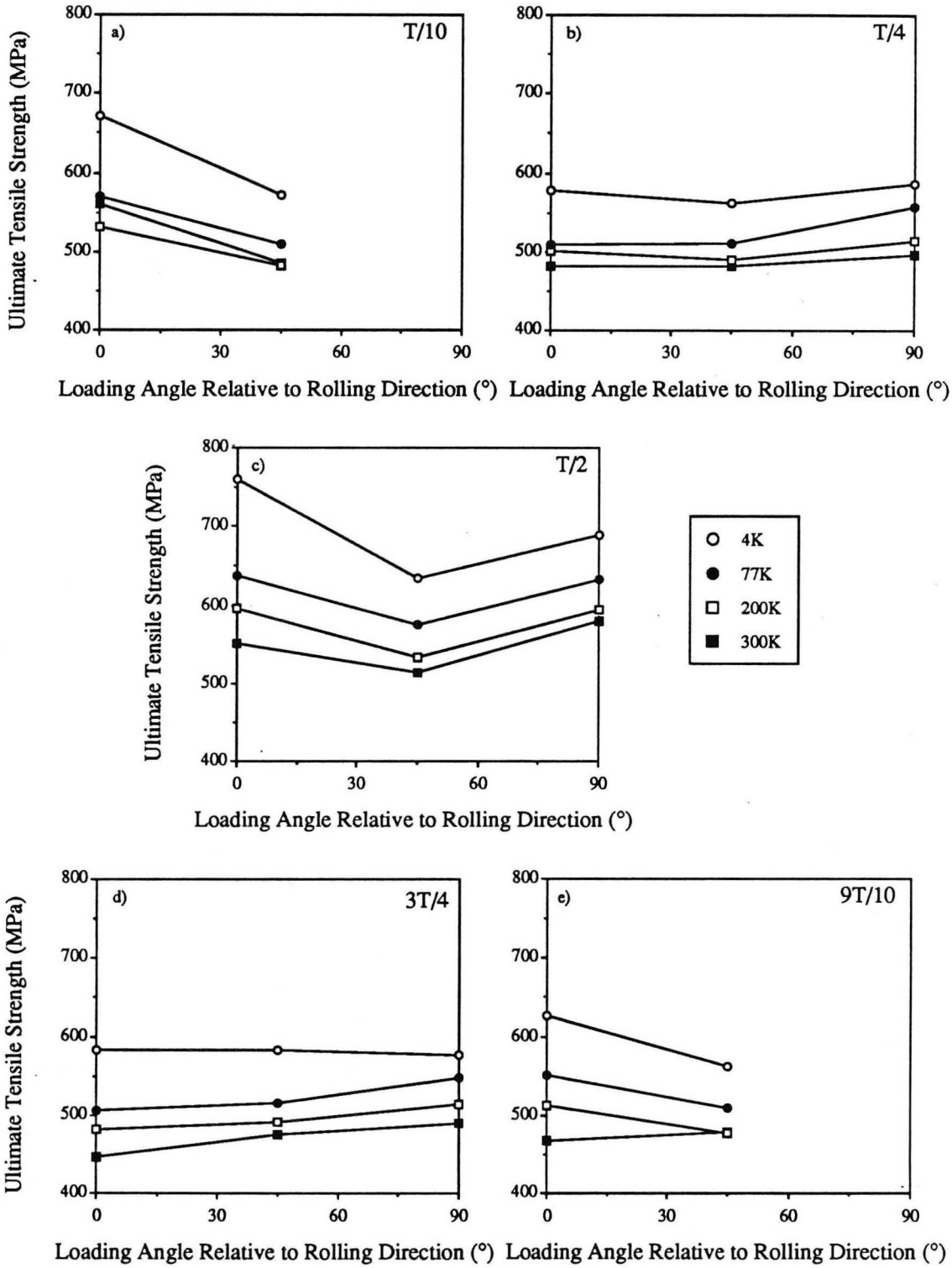

Figure 26: Variation of the ultimate tensile strength with orientation for Vintage III 2090-T81 tensile specimens taken at a) T/10, b) T/4, c) T/2, d) 3T/4, and e) 9T/10 and tested at 300K, 200K, 77K, and 4K.

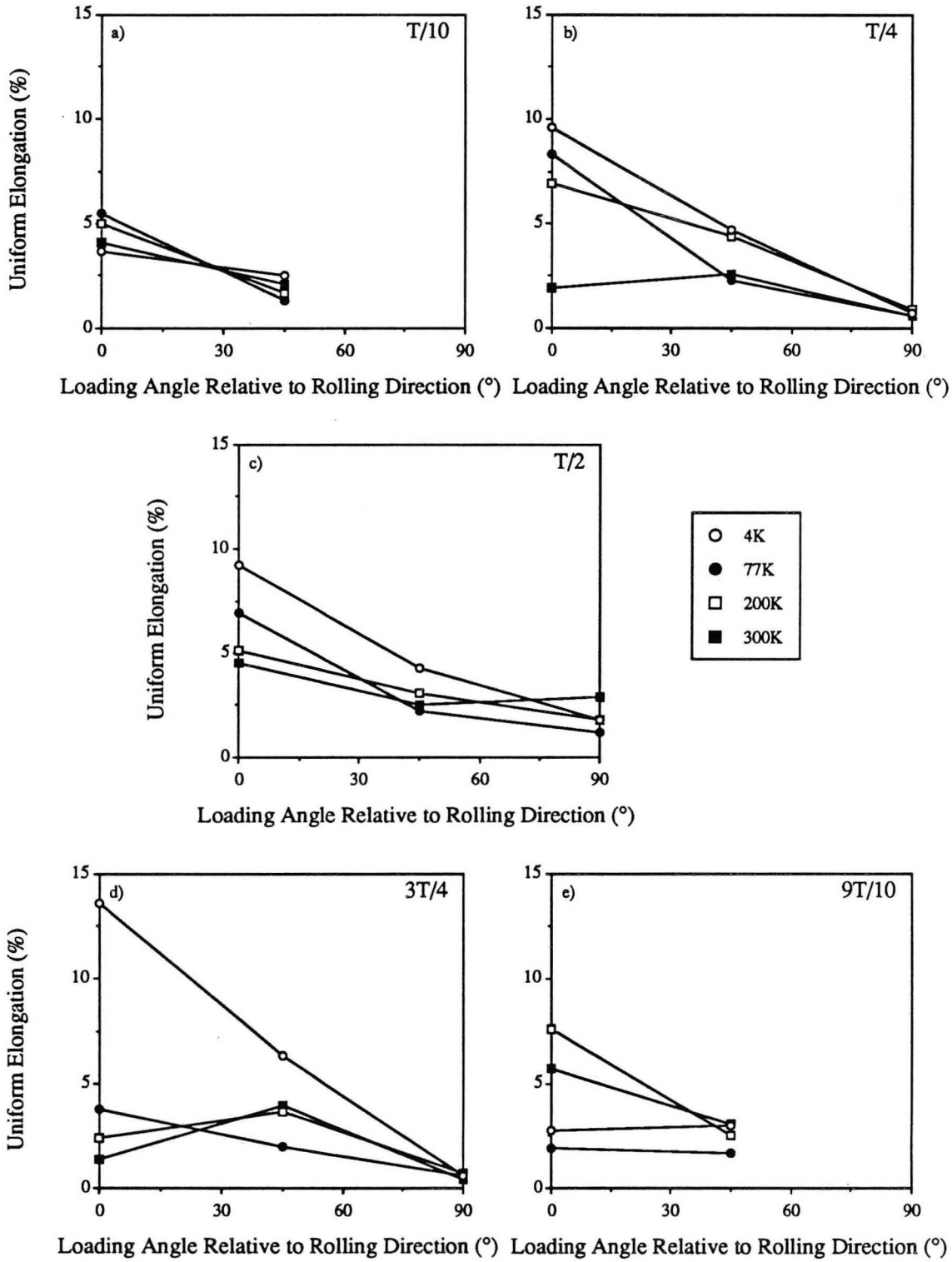

Figure 27: Variation of the uniform elongation with orientation for Vintage III 2090-T81 tensile specimens taken at a) T/10, b) T/4, c) T/2, d) 3T/4, and e) 9T/10 and tested at 300K, 200K, 77K, and 4K.

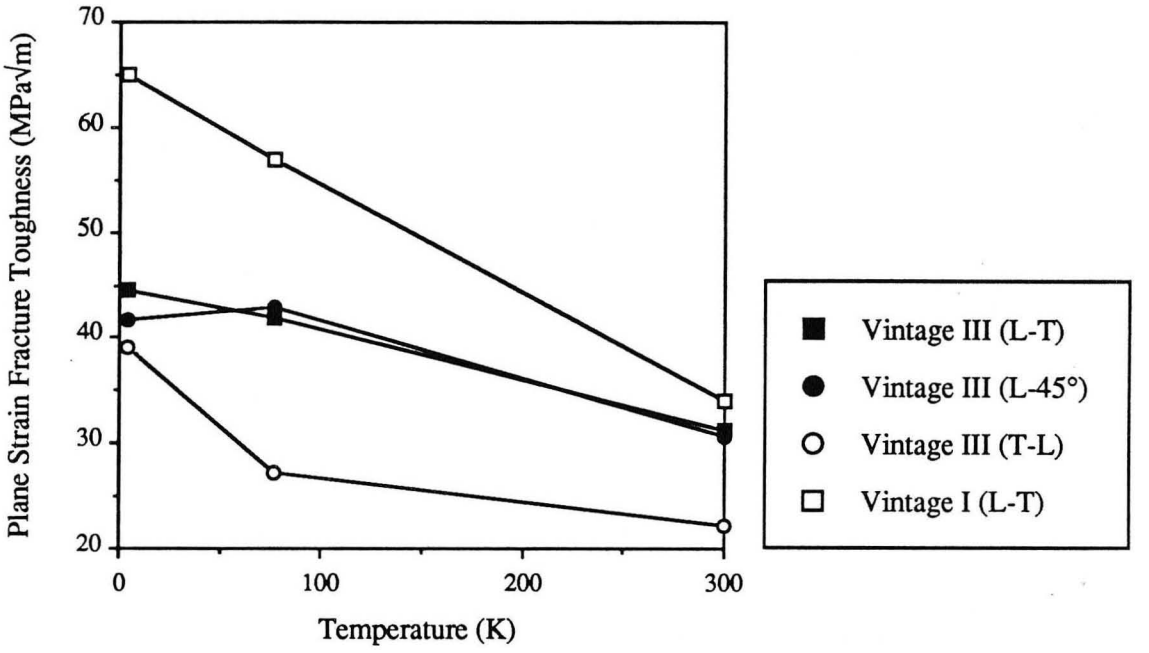

Figure 28: Variation of the fracture toughness with temperature for Vintage III 2090-T81 L-T, L-45°, and T-L J_{Ic} specimens. Values obtained for Vintage I 2090-T81 L-T J_{Ic} specimens are also shown for comparison.

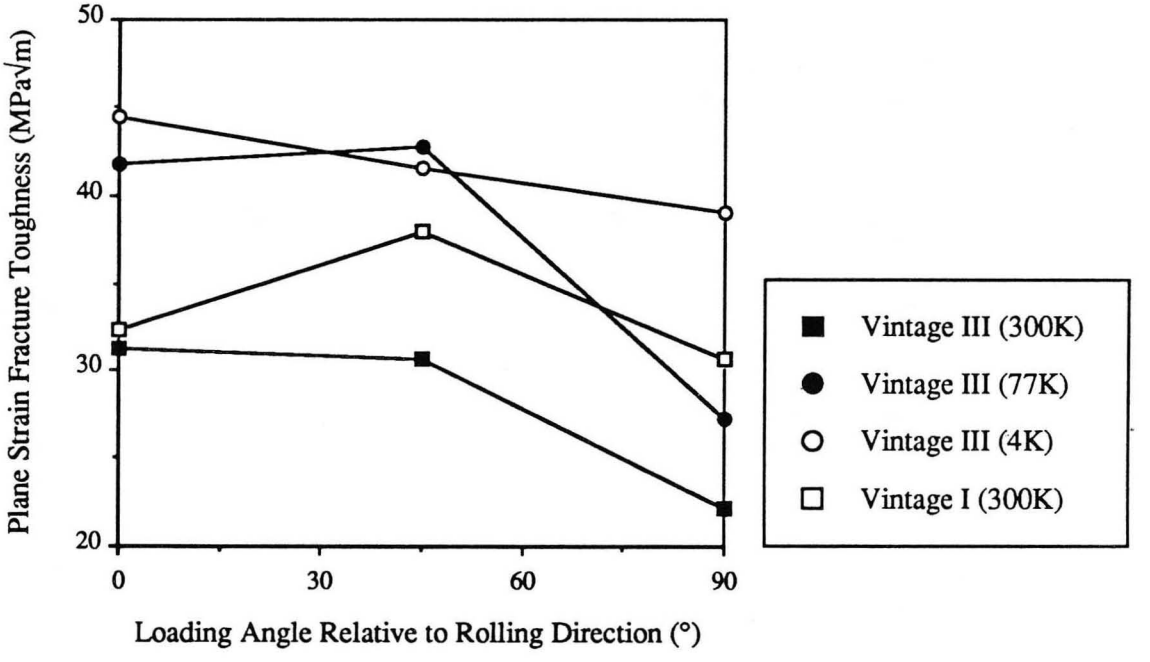

Figure 29: Variation of the fracture toughness with orientation for Vintage III 2090-T81 J_{Ic} specimens tested at 300K, 200K, 77K, and 4K. Values obtained for Vintage I 2090-T81 at 300K are also shown for comparison.

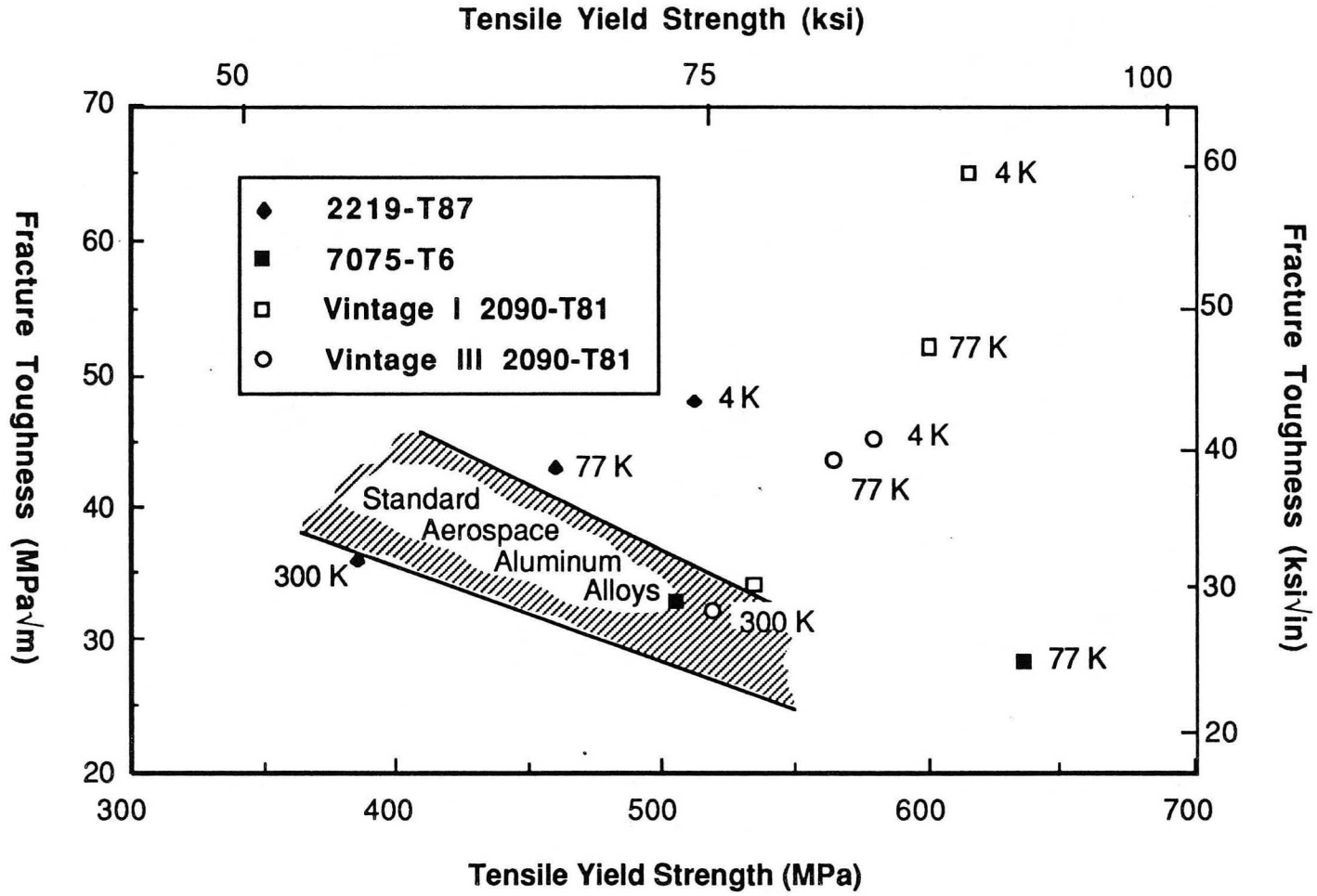

Figure 30: The strength-toughness-temperature relation of the aluminum alloys 7075-T6, 2219-T87, Vintage I 2090-T81, and Vintage III 2090-T81. The strength-toughness trend line for advanced aerospace aluminum alloys at room temperature is also shown for comparison.

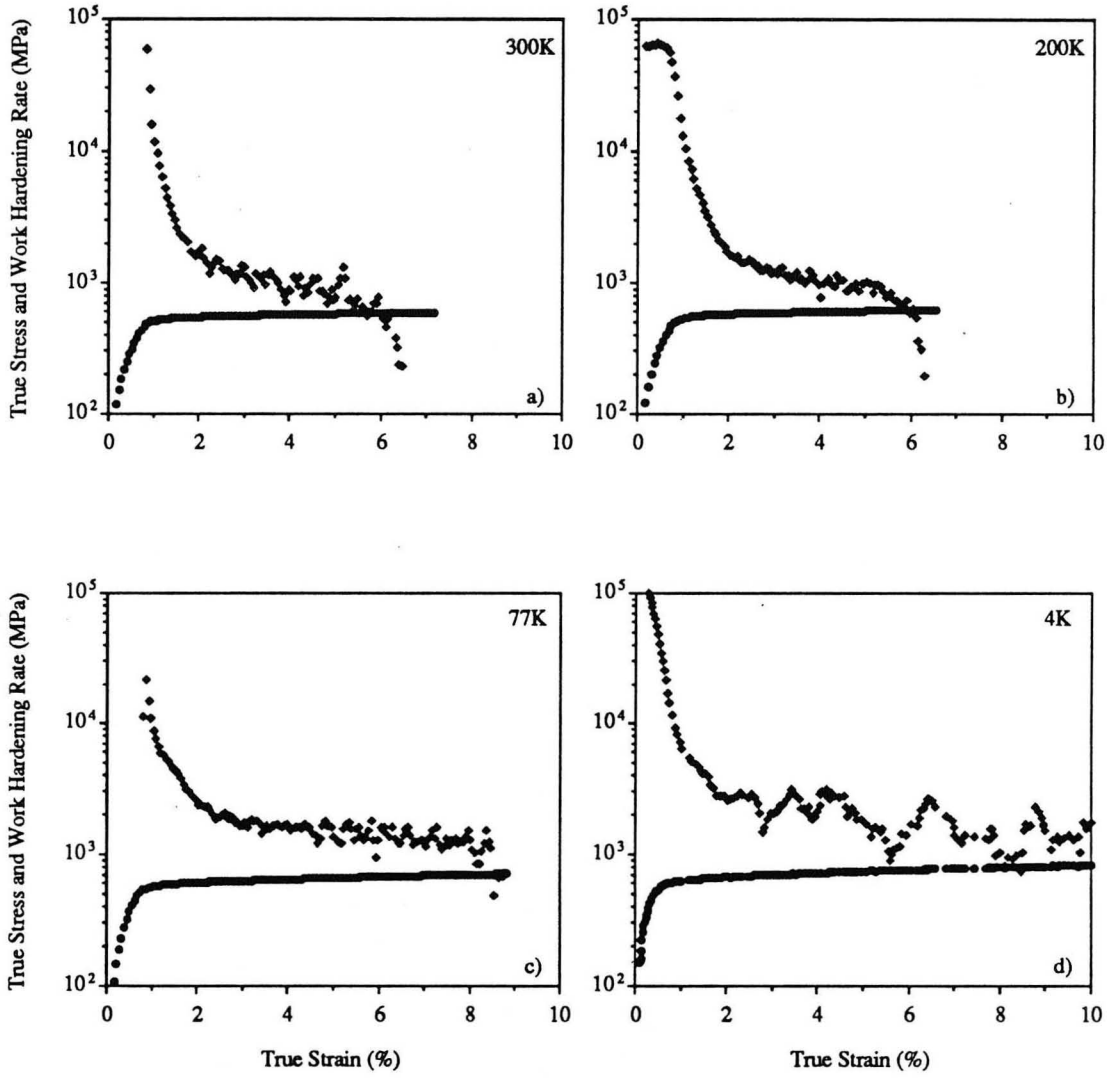

Figure 31: Comparison of the true stress and work hardening rate as a function of true strain for Vintage III 2090-T81 longitudinal tensile specimens taken at mid-thickness and tested at a) 300K, b) 200K, c) 77K, and d) 4K.

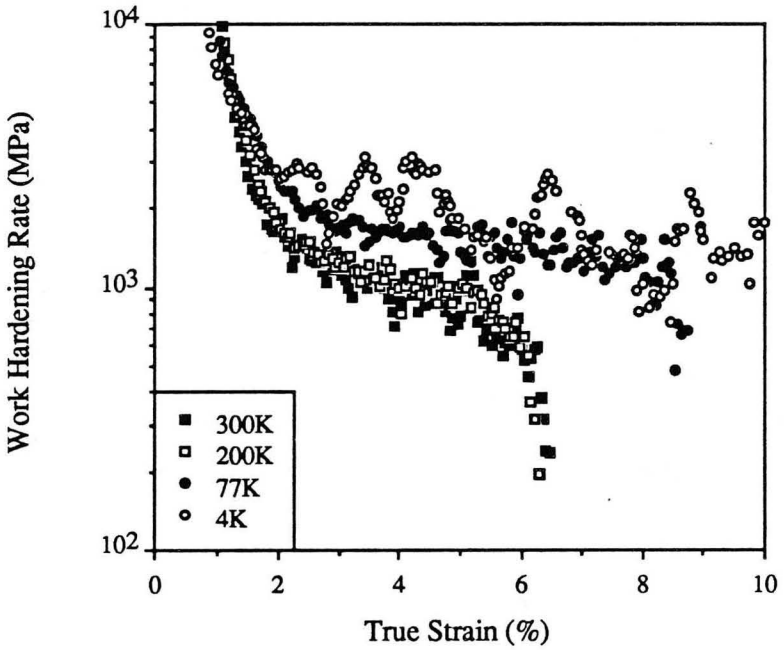

Figure 32: Temperature variation of the work hardening rate as a function of true strain for Vintage III 2090-T81 longitudinal tensile specimens taken at mid-thickness.

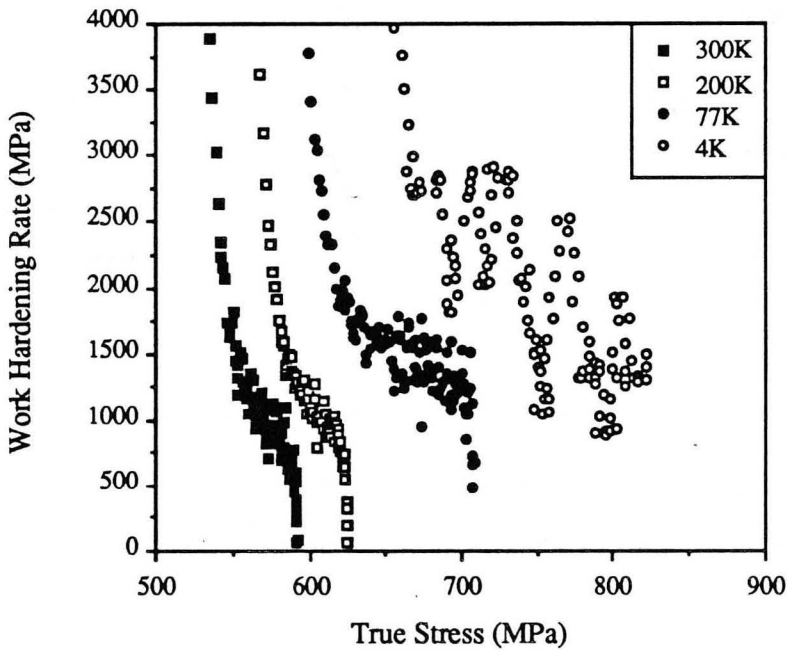

Figure 33: Temperature variation of the work hardening rate as a function of true stress for Vintage III 2090-T81 longitudinal tensile specimens taken at mid-thickness.

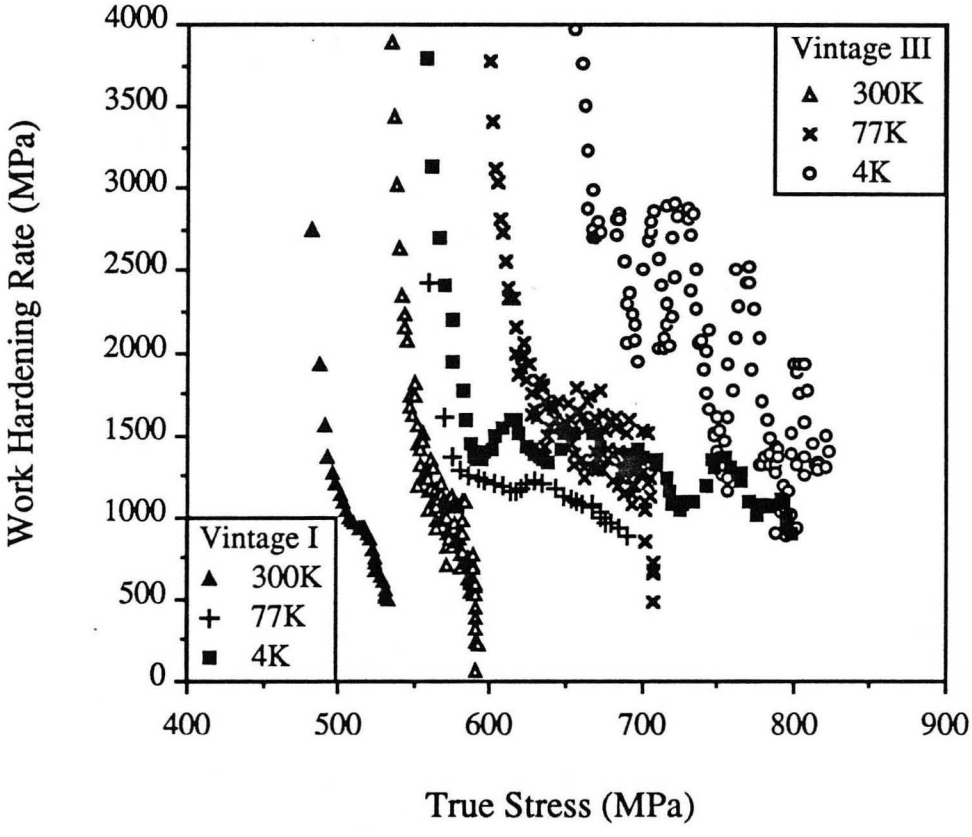

Figure 34: Comparison of the work hardening rate as a function of true stress for Vintage I 2090-T81 longitudinal tensile specimens taken at quarter-thickness (After Glazer, ref. 15) and Vintage III 2090-T81 longitudinal tensile specimens taken at mid-thickness.

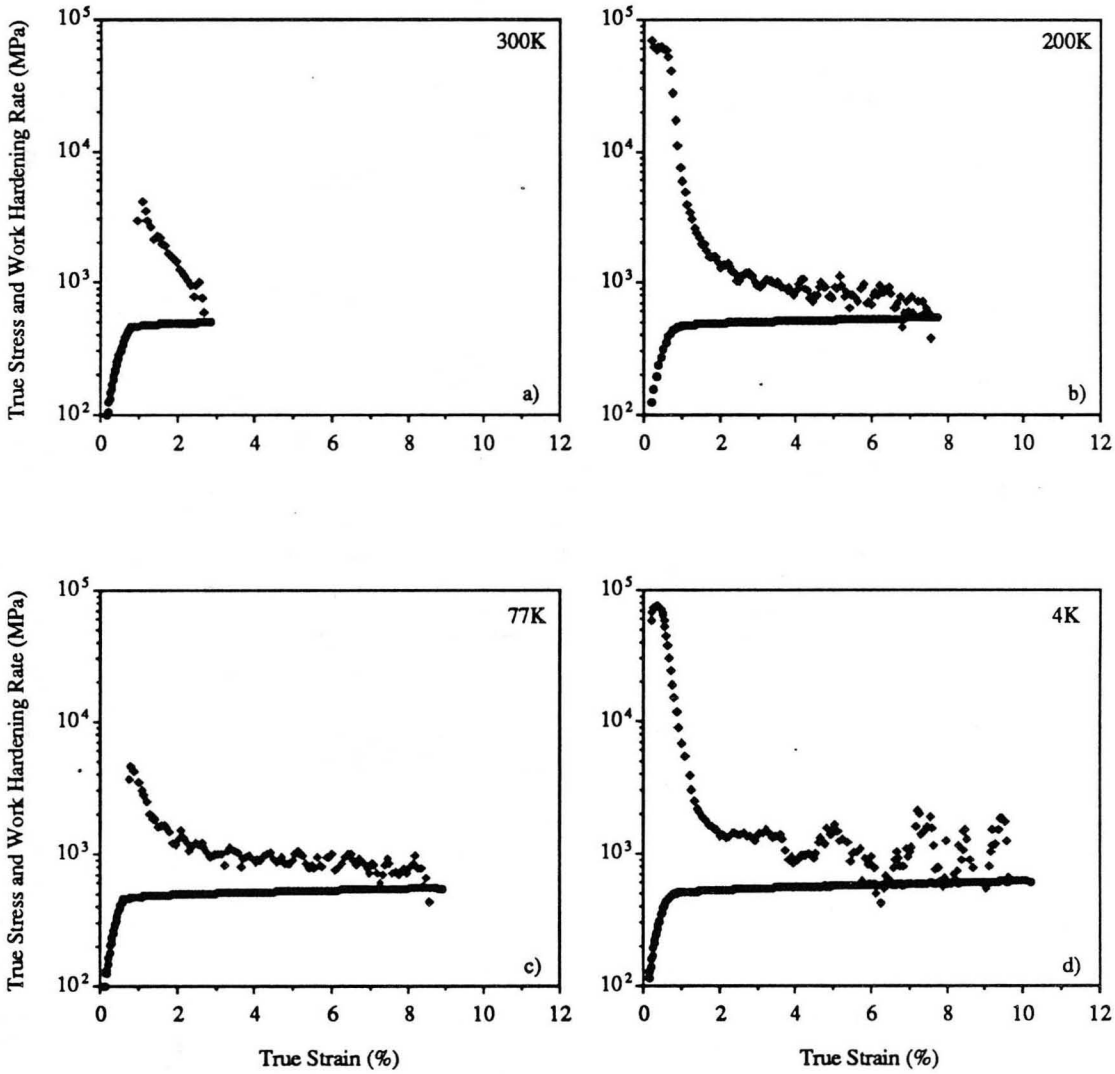

Figure 35: Comparison of the true stress and work hardening rate as a function of true strain for Vintage III 2090-T81 longitudinal tensile specimens taken at quarter-thickness and tested at a) 300K, b) 200K, c) 77K, and d) 4K.

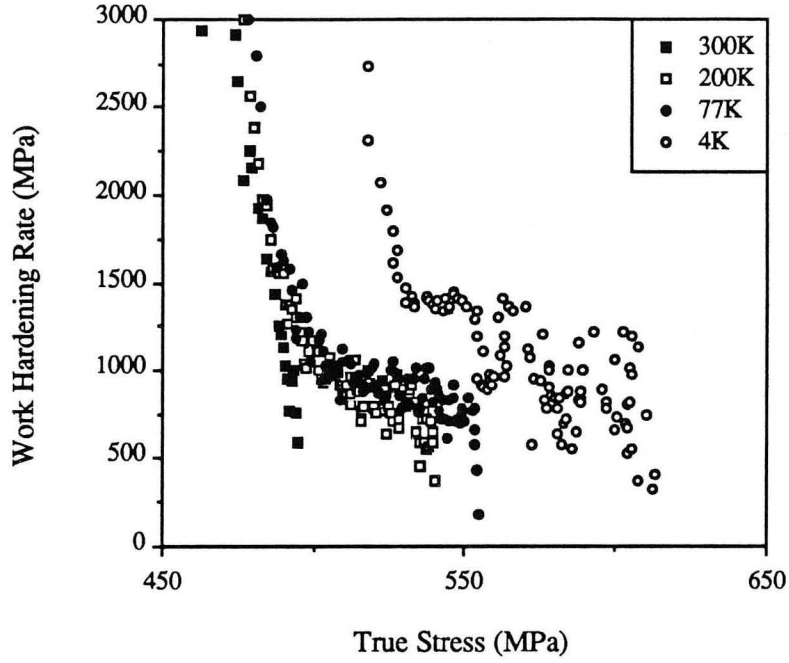

Figure 36: Temperature variation of the work hardening rate as a function of true stress for Vintage III 2090-T81 longitudinal tensile specimens taken at quarter-thickness. Note that the slope is constant at 300K indicating the absence of a region of stable deformation.

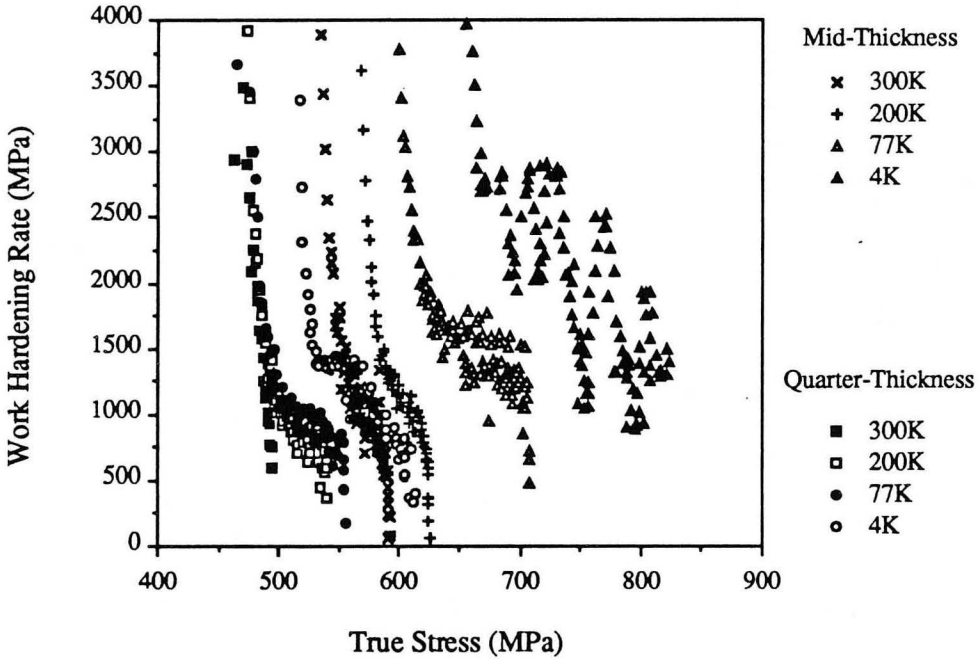

Figure 37: Temperature variation of the work hardening rate as a function of true stress for Vintage III 290-T81 longitudinal tensile specimens taken at mid-thickness and quarter-thickness.

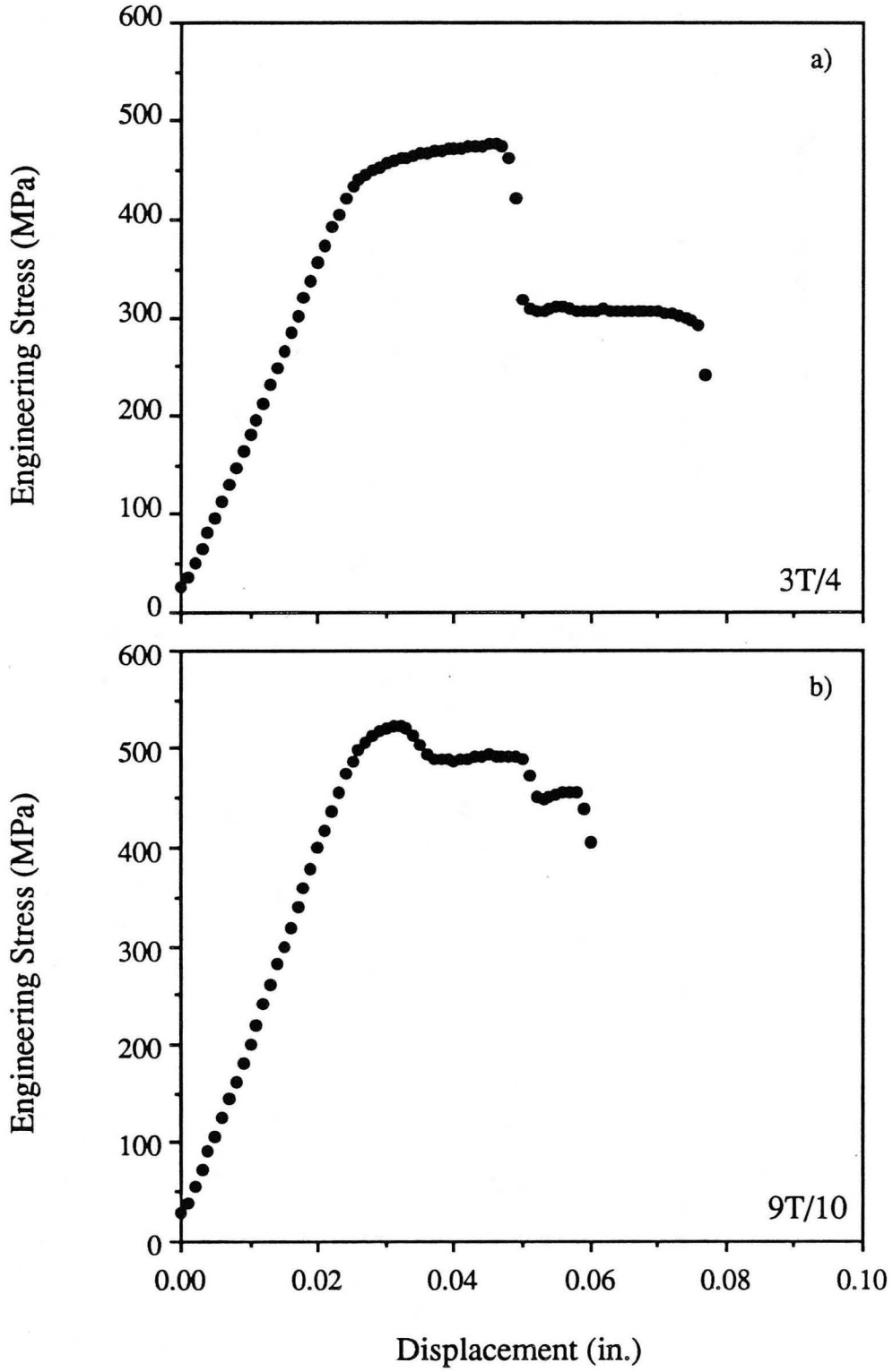

Figure 38: Plot of engineering stress versus stroke displacement for Vintage III 2090-T81 tensile specimens at a) 3T/4 and b) 9T/10 highlighting the effect of splitting. Note the extension of the curve following the partial fracture and load drop.

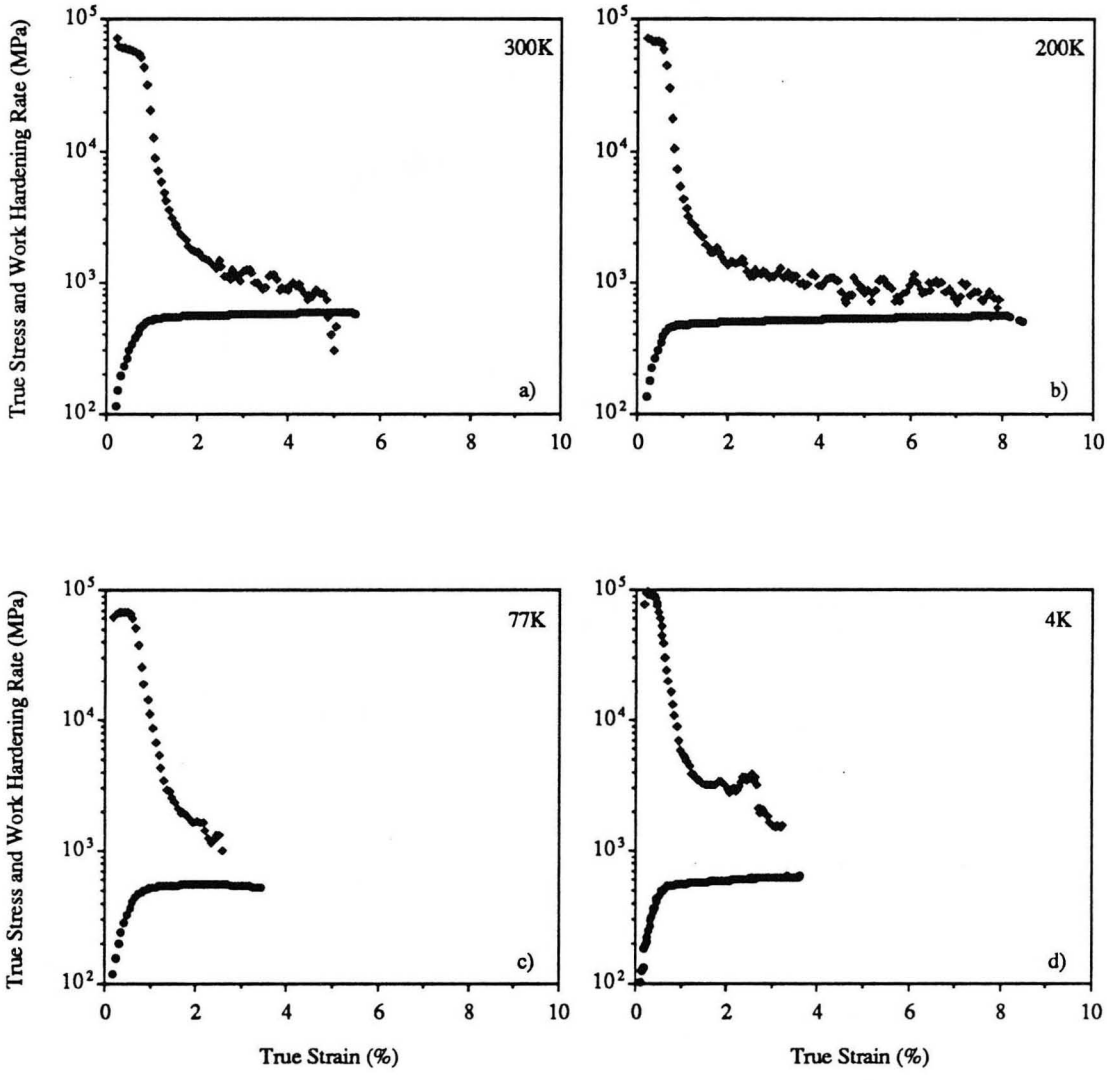

Figure 39: Comparison of the true stress and work hardening rate as a function of true strain for Vintage III 2090-T81 longitudinal tensile specimens taken at tenth-thickness and tested at a) 300K, b) 200K, c) 77K, and d) 4K.

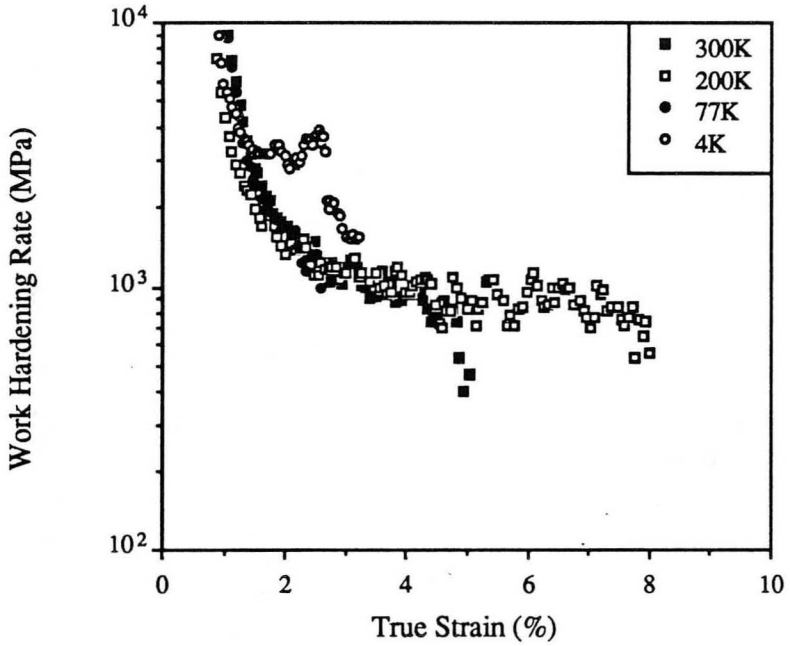

Figure 40: Temperature variation of the work hardening rate as a function of true strain for Vintage III 2090-T81 tensile specimens taken at tenth-thickness. Note the increase in the early work hardening rate at 4K.

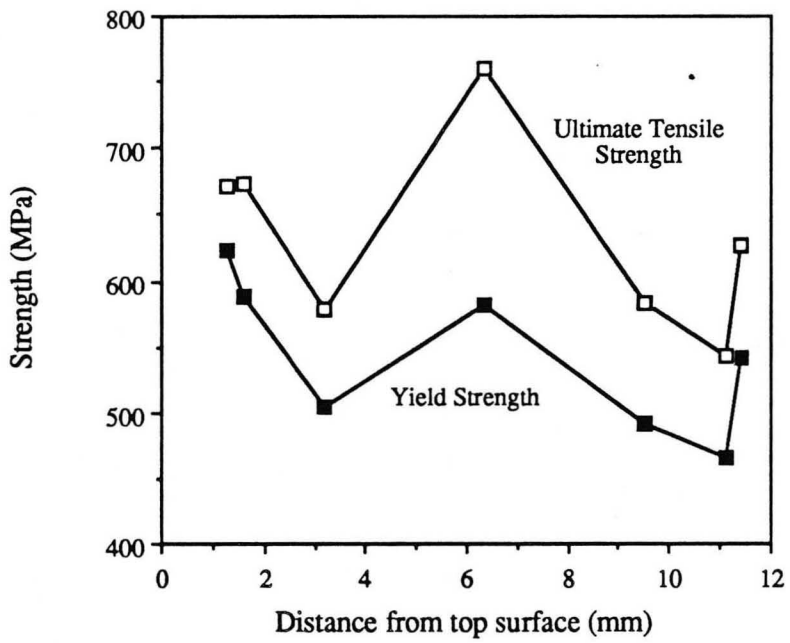

Figure 41: Variation of the yield strength and ultimate tensile strength with through-thickness position for Vintage III 2090-T81 longitudinal tensile specimens tested at 4K. Data points include those obtained from tensile specimens taken at T/8 and 9T/8.

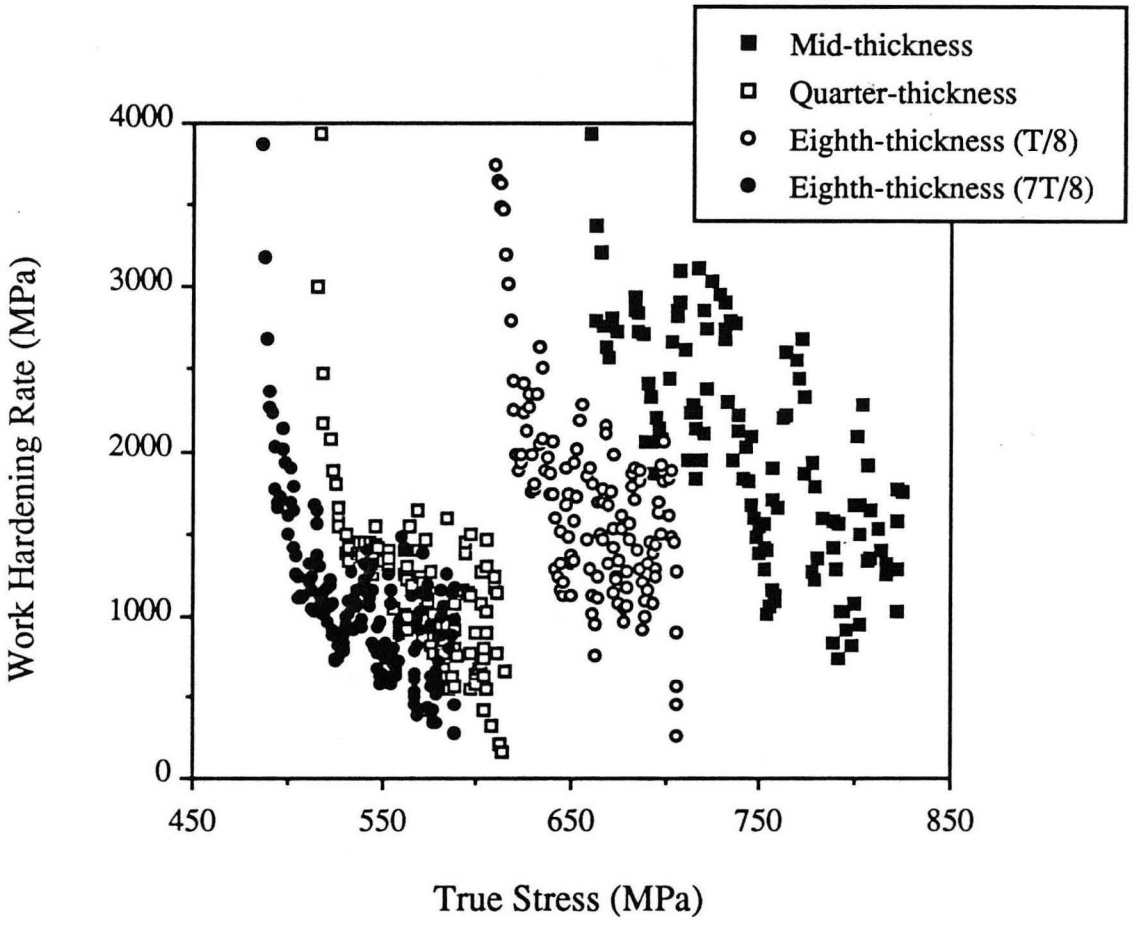

Figure 42: Comparison of the work hardening rate as a function of true stress for Vintage III 2090-T81 longitudinal tensile specimens taken at mid-thickness, quarter-thickness, and eighth-thicknesses and tested at 4K.

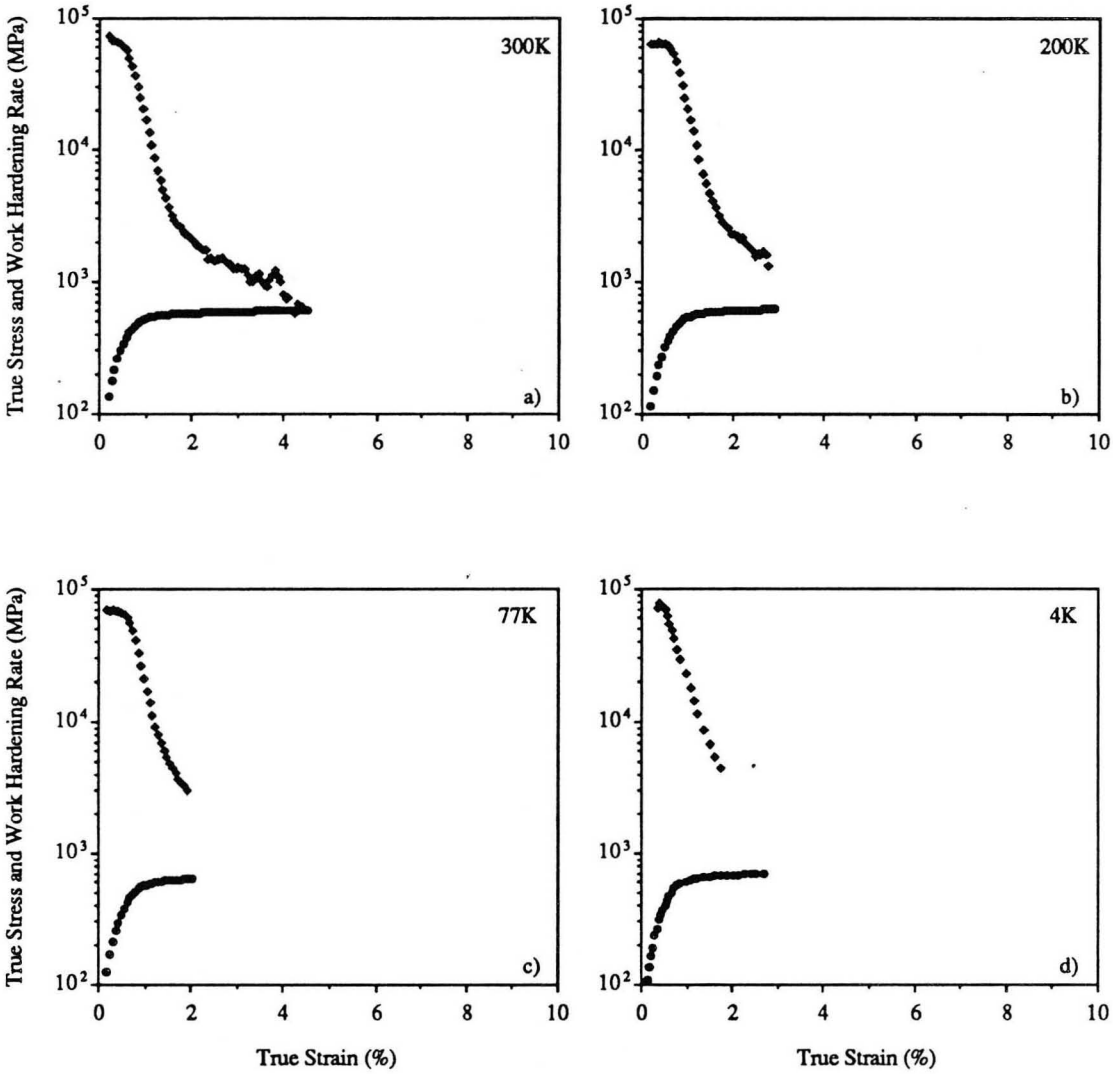

Figure 43: Comparison of the true stress and work hardening rate as a function of true strain for Vintage III 2090-T81 long-transverse tensile specimens taken at mid-thickness and tested at a) 300K, b) 200K, c) 77K, and d) 4K.

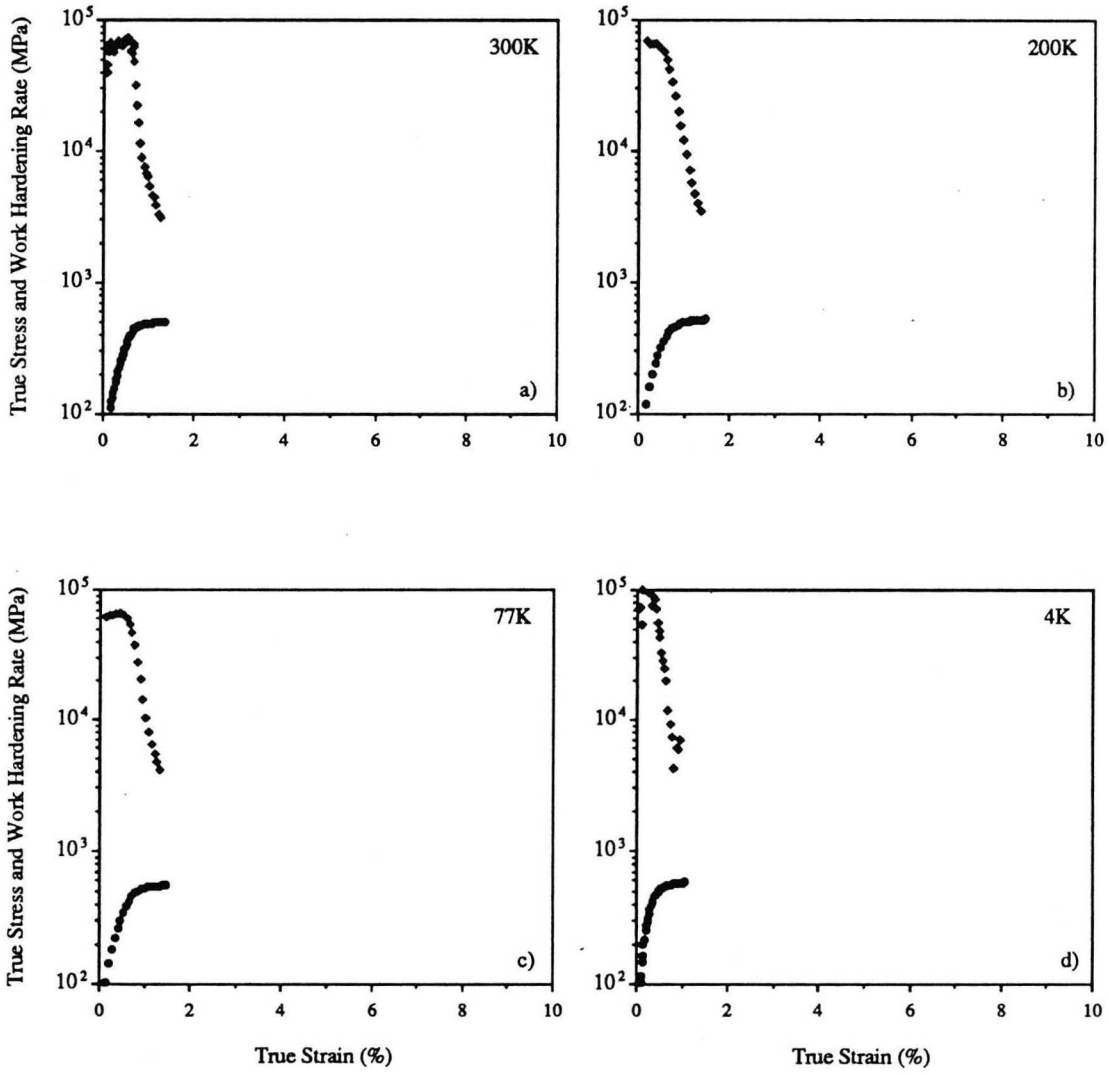

Figure 44: Comparison of the true stress and work hardening rate as a function of true strain for Vintage III 2090-T81 long-transverse tensile specimens taken at quarter-thickness and tested at a) 300K, b) 200K, c) 77K, and d) 4K.

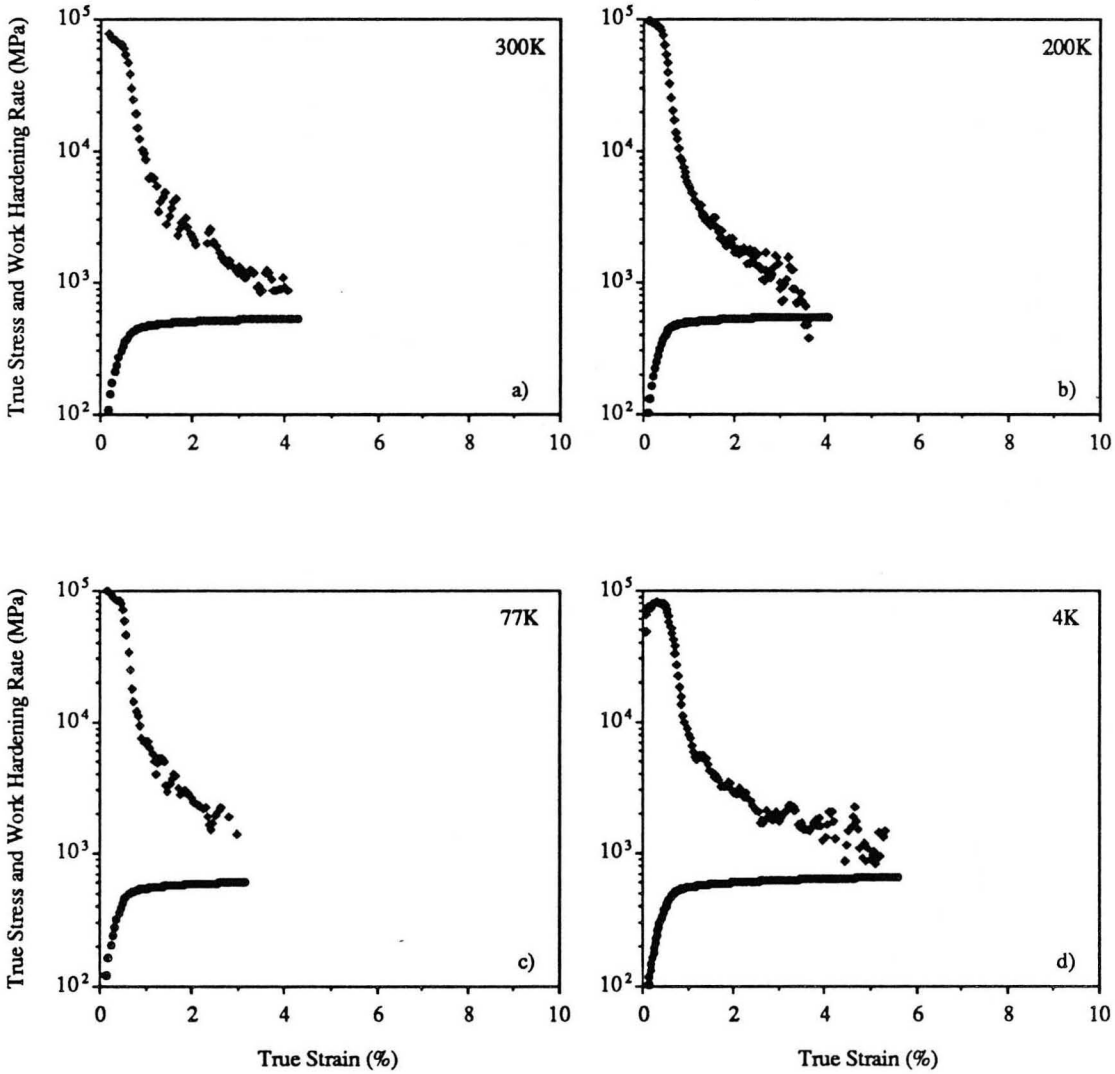

Figure 45: Comparison of the true stress and work hardening rate as a function of true strain for Vintage III 2090-T81 45° tensile specimens taken at mid-thickness and tested at a) 300K, b) 200K, c) 77K, and d) 4K.

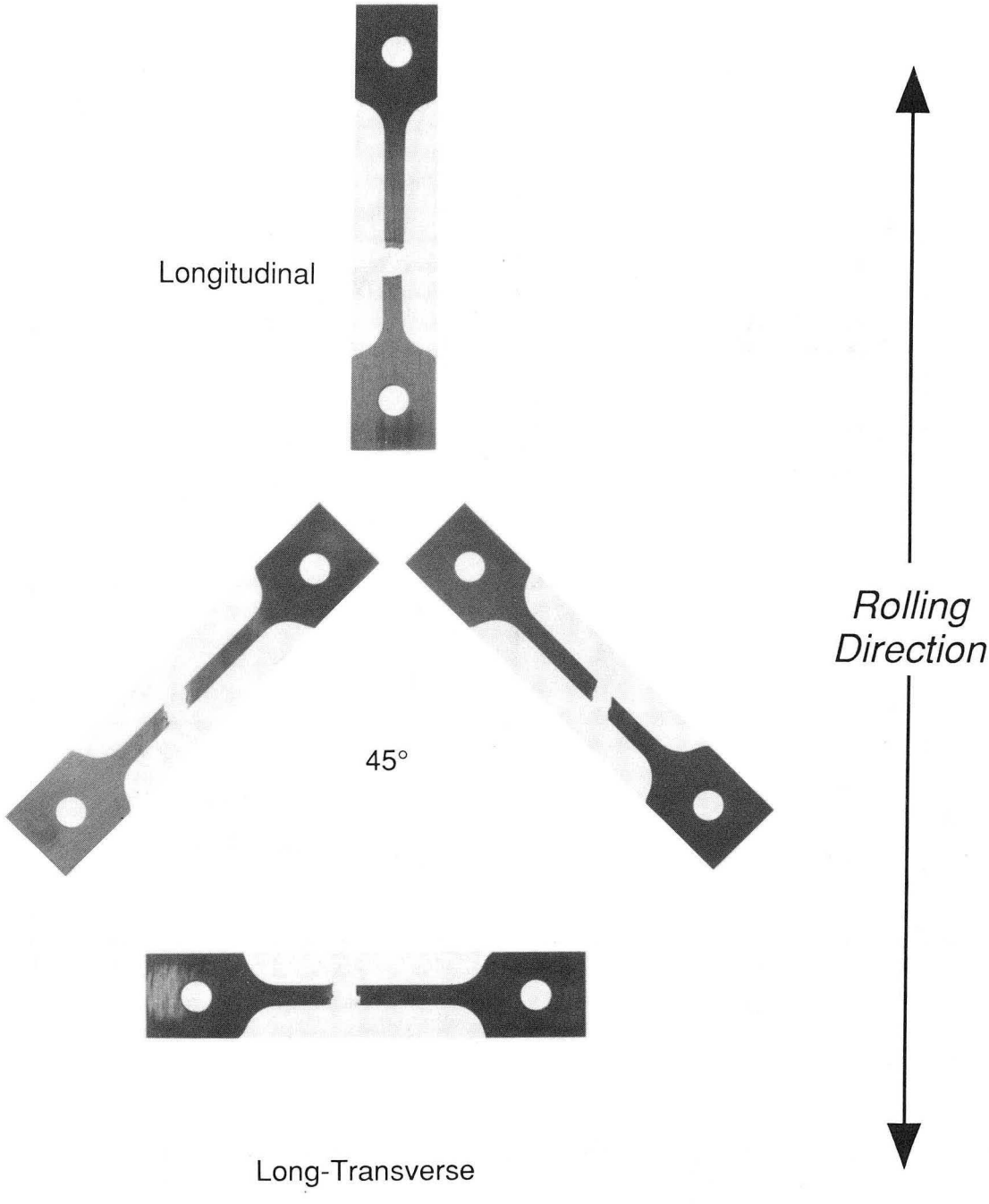

Figure 46: Optical micrograph showing the typical fracture profile of the longitudinal, 45°, and long-transverse tensile specimens. Note that the failure of the 45° tensile specimens occur along the grain boundaries normal to the transverse direction. (XBB 900-9800)

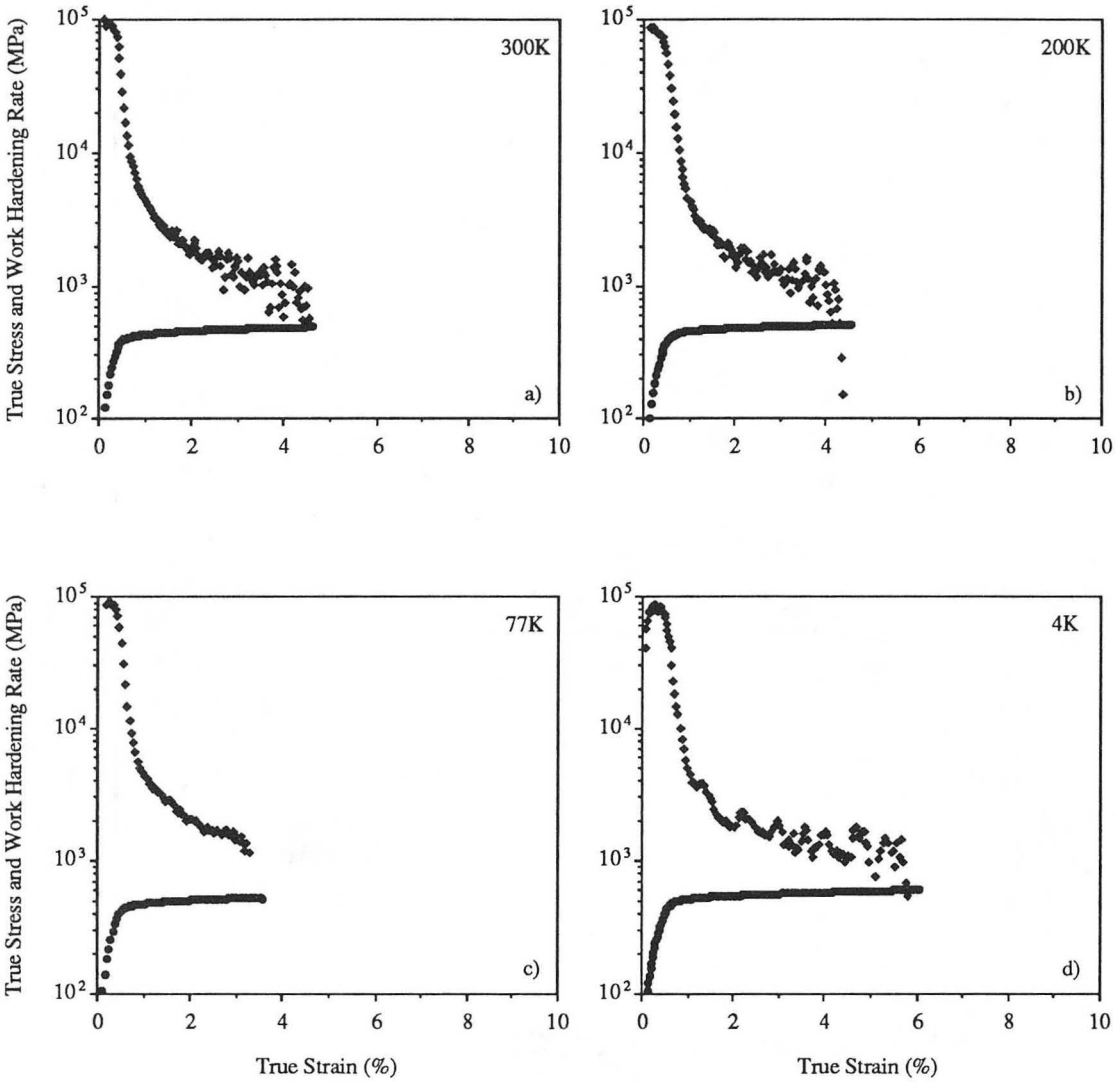

Figure 47: Comparison of the true stress and work hardening rate as a function of true strain for Vintage III 2090-T81 45° tensile specimens taken at quarter-thickness and tested at a) 300K, b) 200K, c) 77K, and d) 4K.

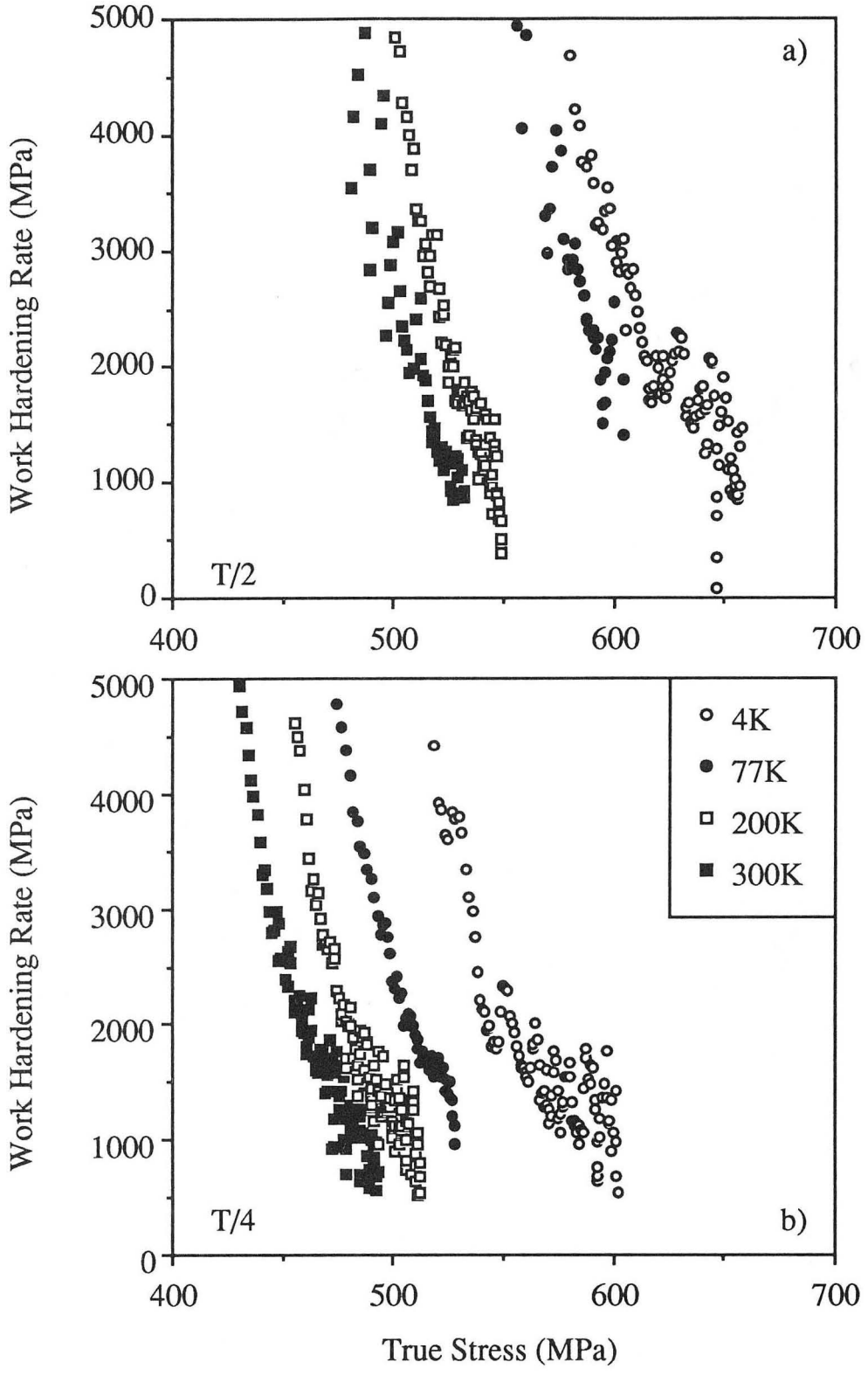

Figure 48: Temperature variation of the work hardening rate as a function of true stress for Vintage III 2090-T81 longitudinal and 45° tensile specimens taken at a) mid-thickness and b) quarter-thickness.

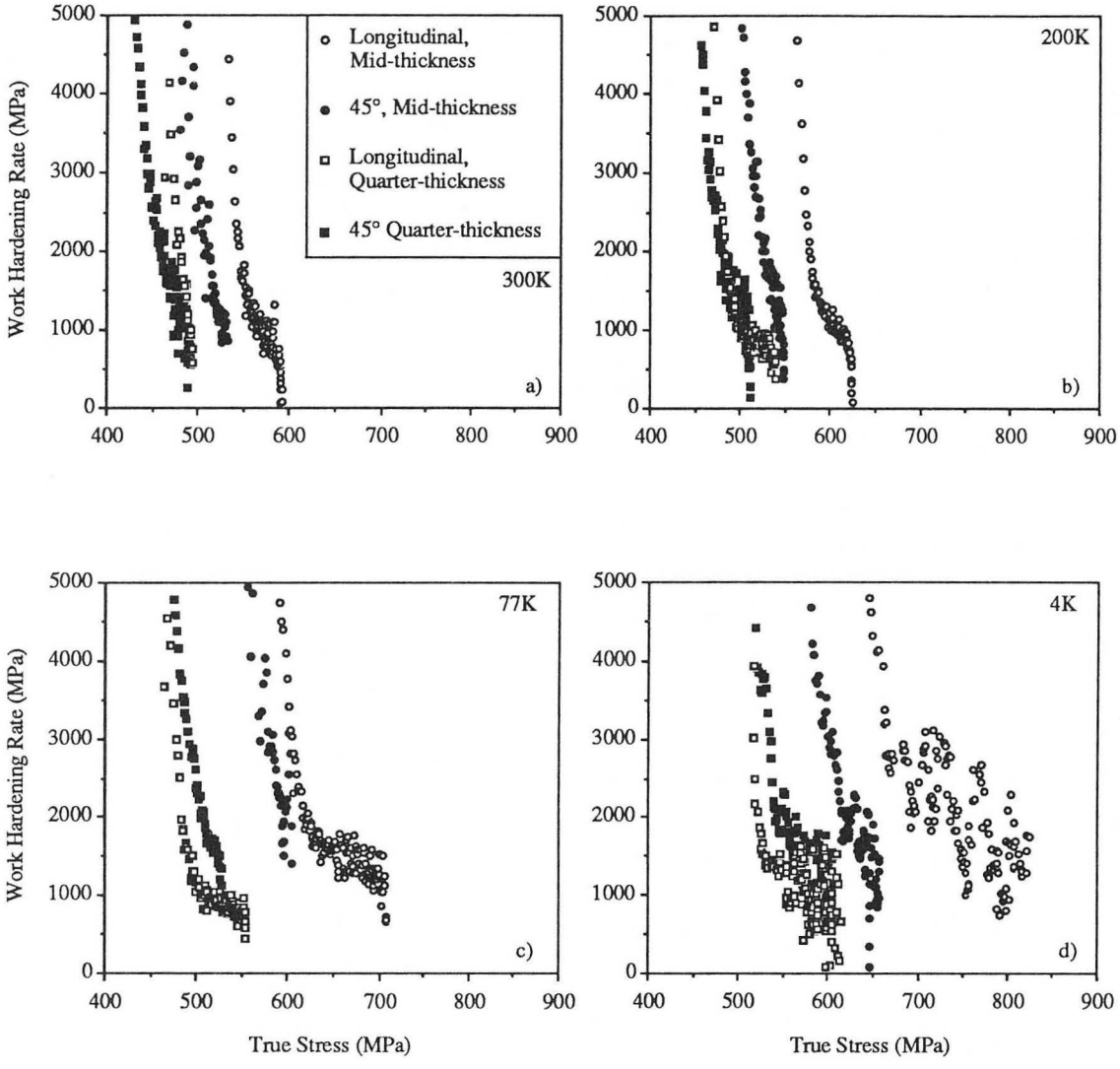

Figure 49: Comparison of the work hardening rate as a function of true stress for Vintage III 2090-T81 longitudinal and 45° tensile specimens taken at mid-thickness and at quarter-thickness and tested at a) 300K, b) 200K, c) 77K, and d) 4K.

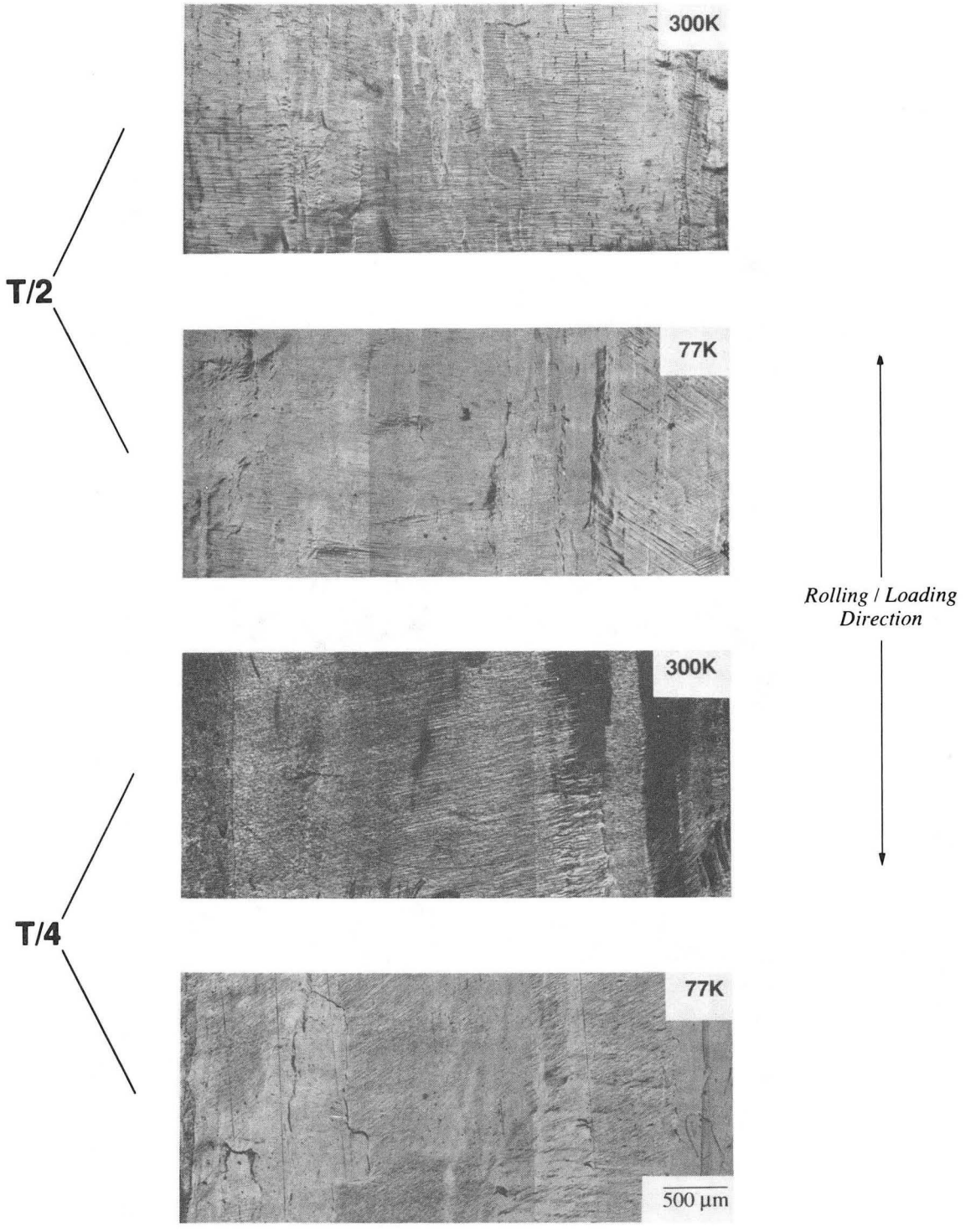

Figure 50: Optical micrographs using Nomarski interference contrast of pre-polished Vintage III 2090-T81 longitudinal tensile specimens after failure. (XBB 900-9409)

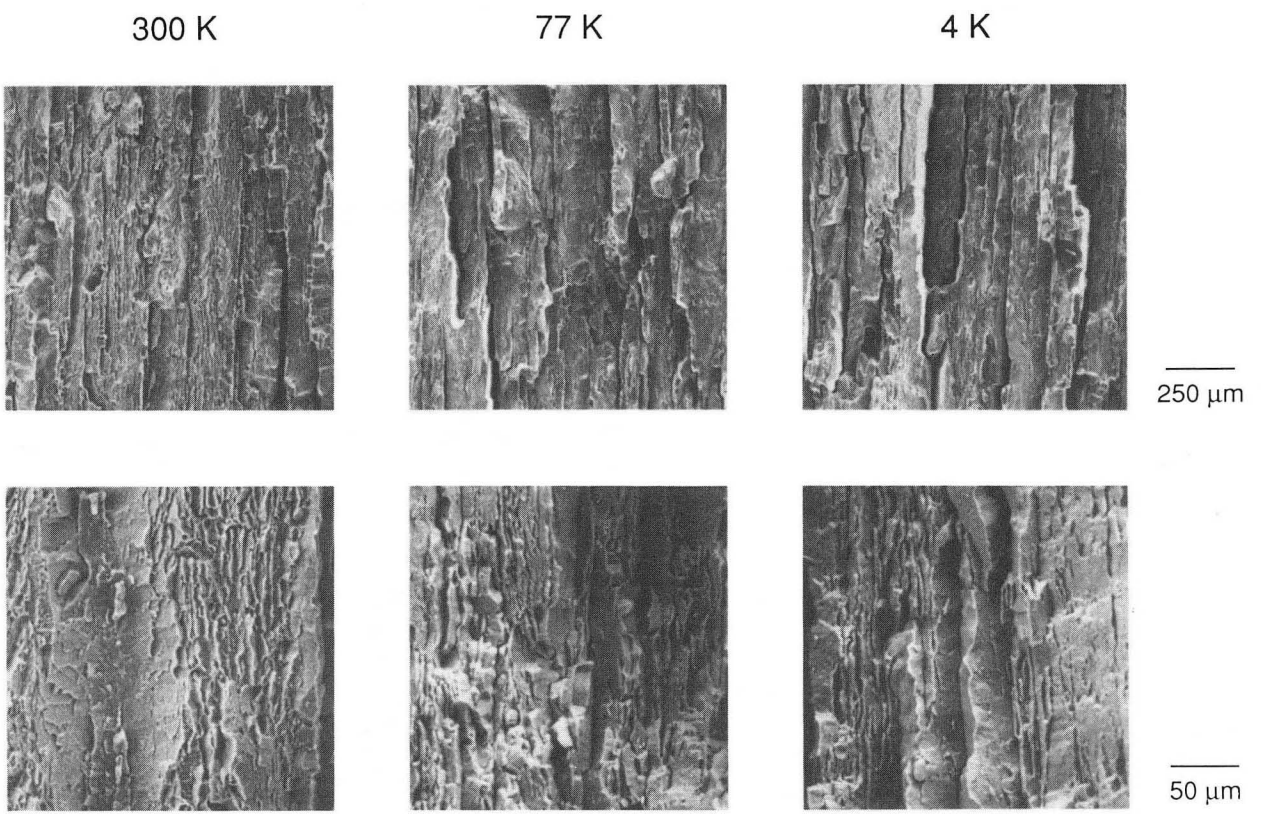

Figure 51: Scanning electron micrographs of the fracture surface at mid-thickness of Vintage III 2090-T81 L-T J_{Ic} specimens tested at 300K, 77K, and 4K. Note the absence of a fracture mode change. (XBB 902-1114)

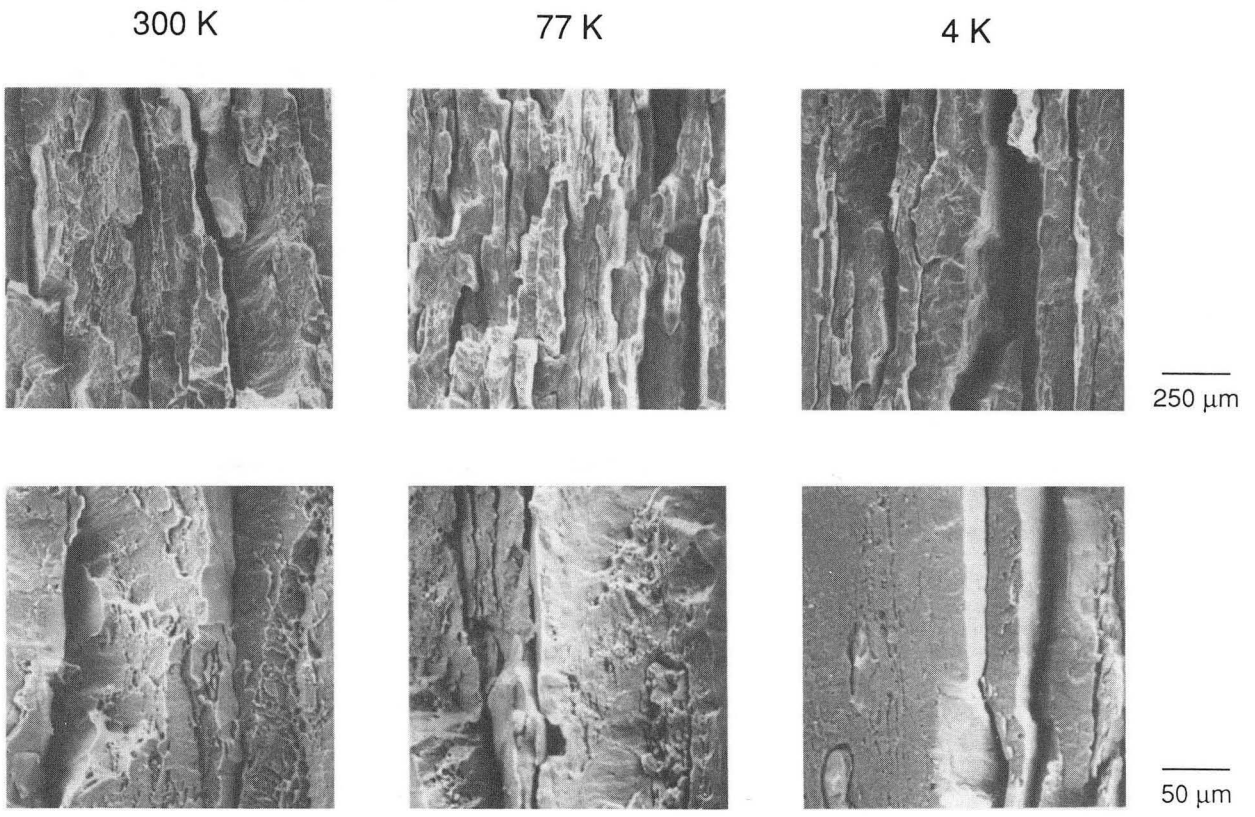

Figure 52: Scanning electron micrographs of the fracture surface at quarter-thickness of Vintage III 2090-T81 L-T J_{Ic} specimens tested at 300K, 77K, and 4K. (XBB 902-1113)

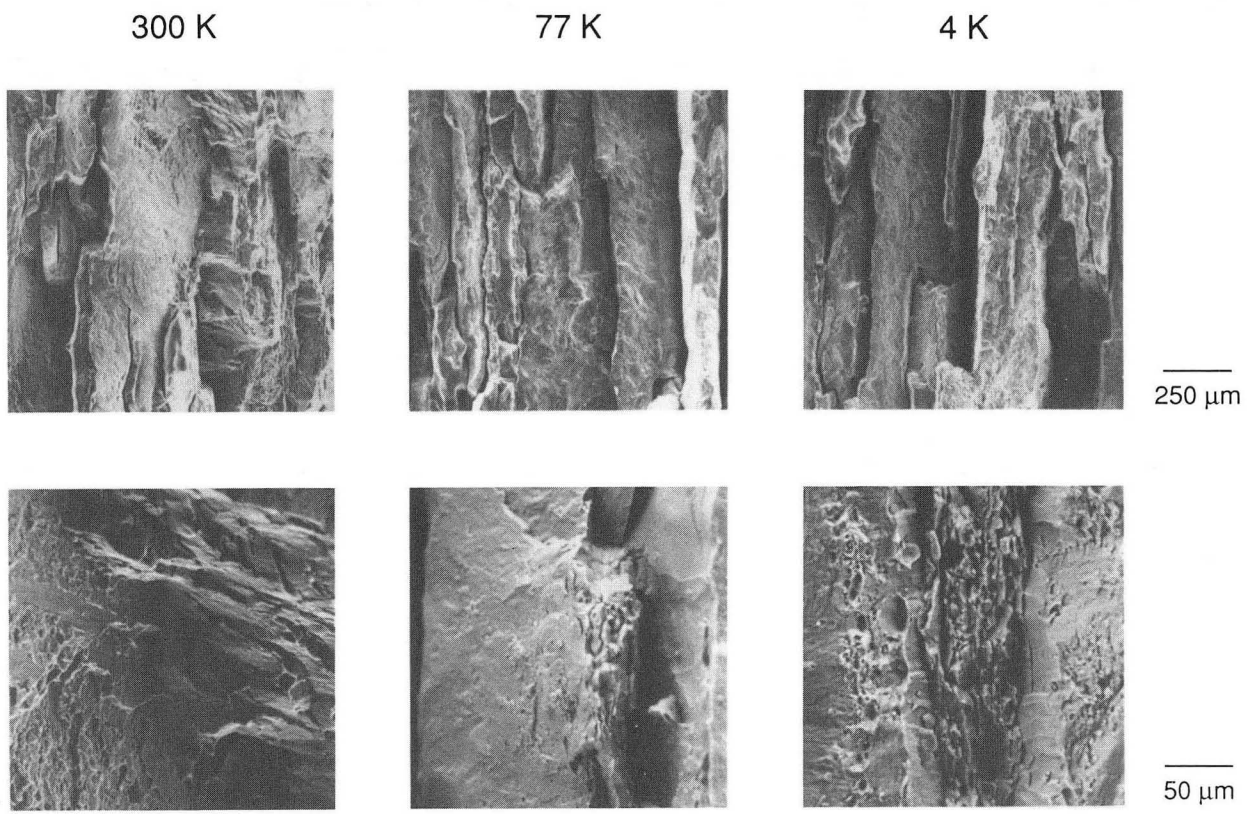

Figure 53: Scanning electron micrographs of the fracture surfaces at tenth-thickness (T/10) of Vintage III 2090-T81 L-T J_{Ic} specimens tested at 300K, 77K, and 4K. (XBB 902-1116)

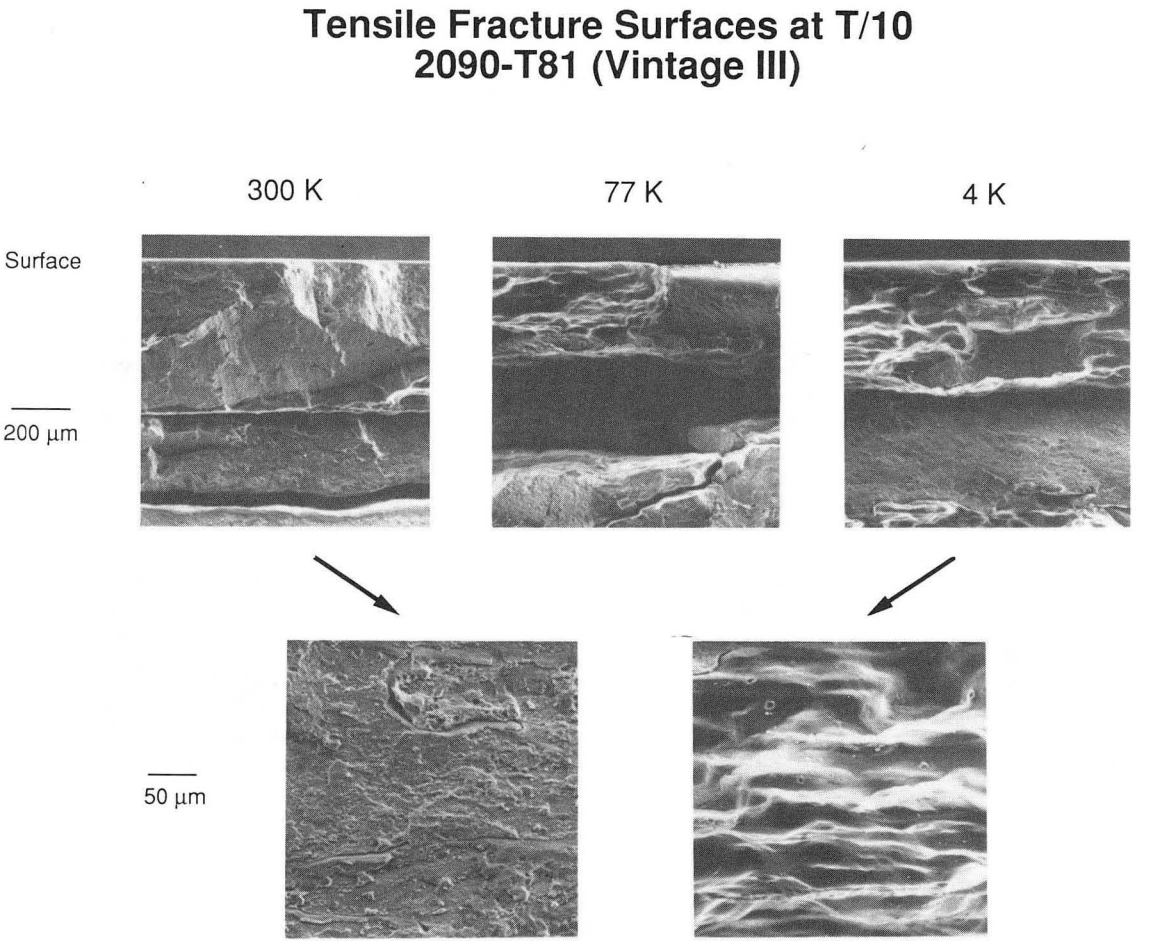

Figure 54: Scanning electron micrographs of the fracture surface at the near-surface region containing equiaxed grains of longitudinal Vintage III 2090-T81 tensile specimens tested at 300K, 77K, and 4K. (XBB 902-1119)

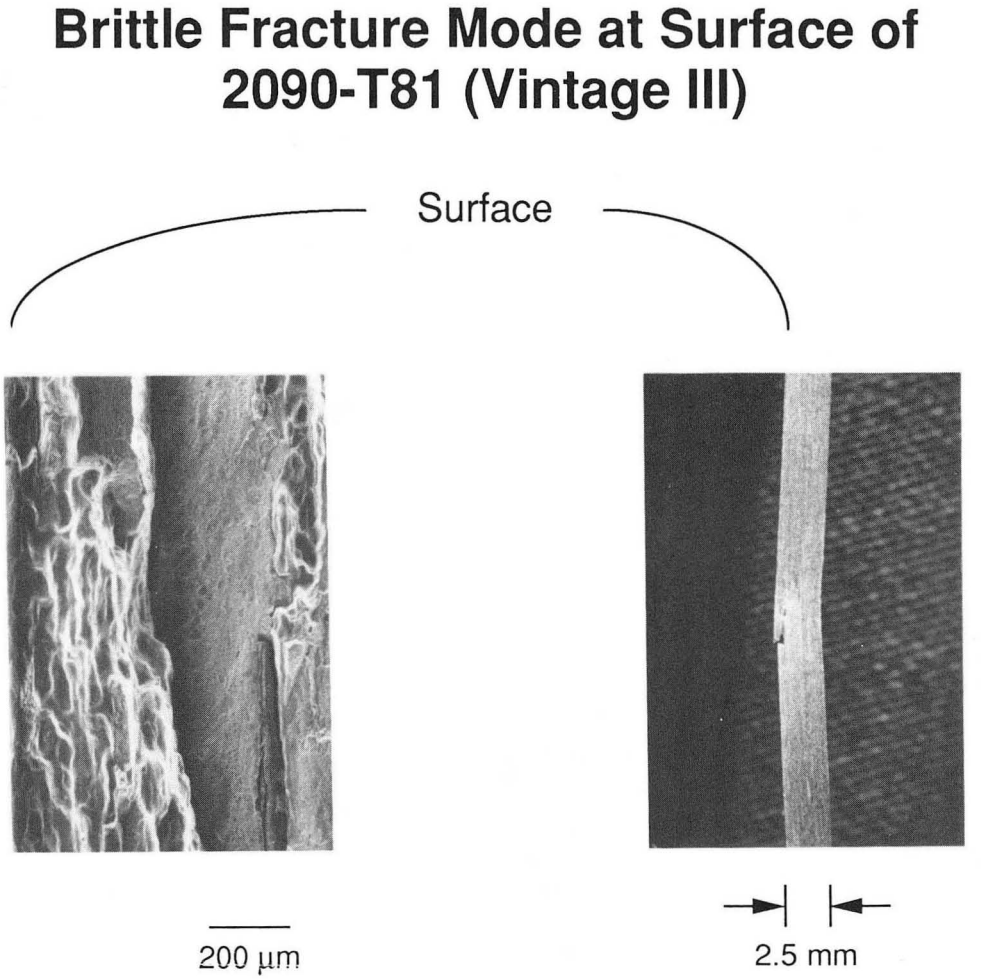

Figure 55: Effect of mode change at the near-surface region containing equiaxed grains on the tensile behavior of longitudinal Vintage III 2090-T81 tensile specimens. (XBB 902-1118)

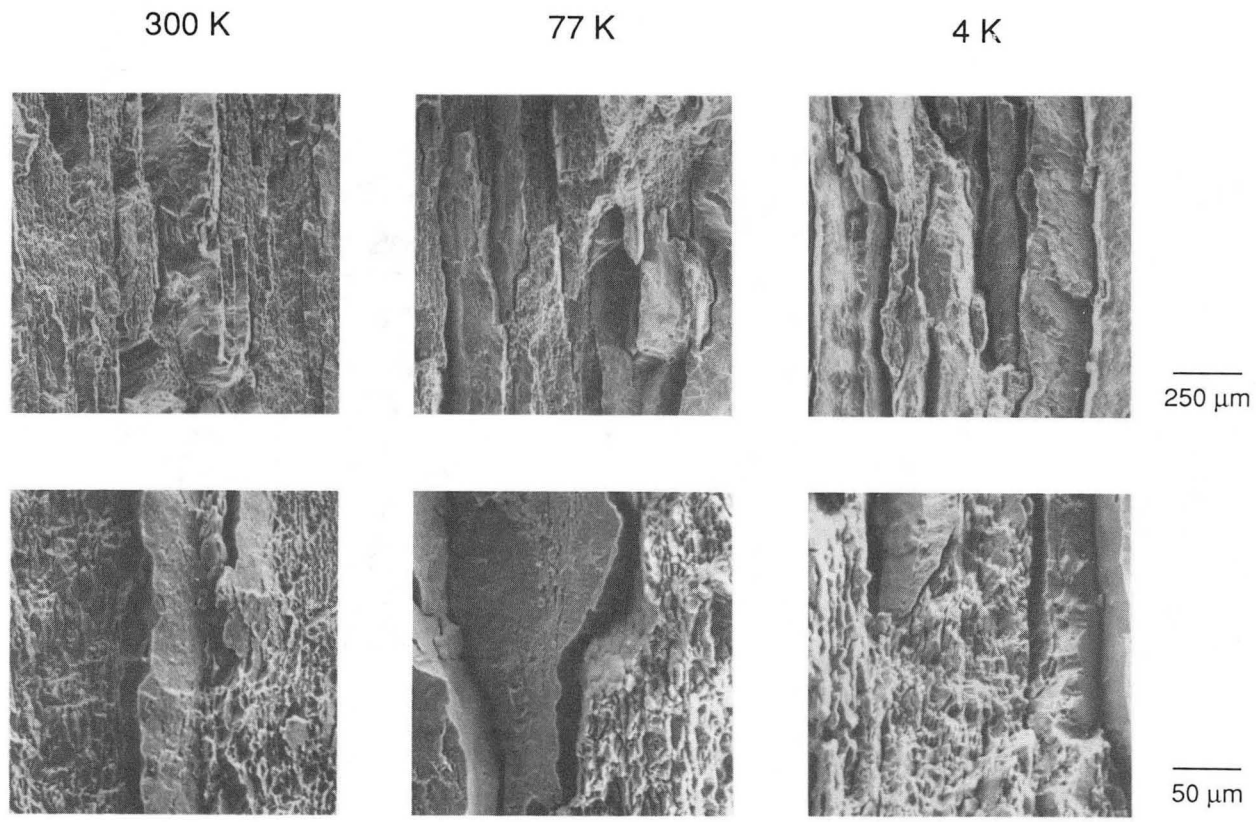

Figure 56: Scanning electron micrographs of the fracture surface at 9T/10 of Vintage III 2090-T81 L-T J_{Ic} specimens tested at 300K, 77K, and 4K. (XBB 902-1115)

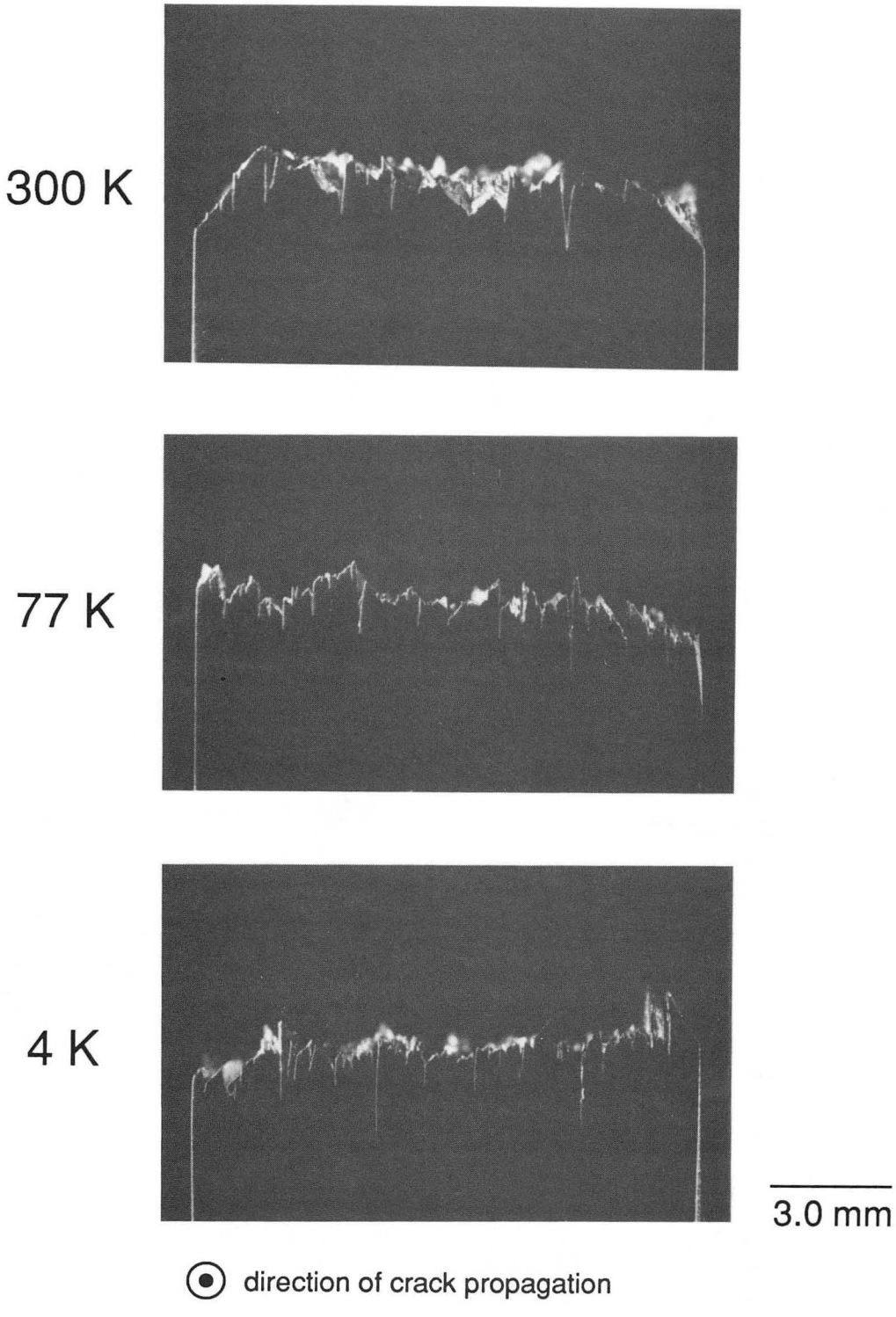

Figure 57: Optical micrographs of the fracture profile and splitting in Vintage III 2090-T81 L-T J_{Ic} specimens tested at 300K, 77K, and 4K. Specimens were sectioned perpendicular to crack path near the crack initiation point. Cross sections shown is the entire thickness of the specimen. (XBB 908-6889)

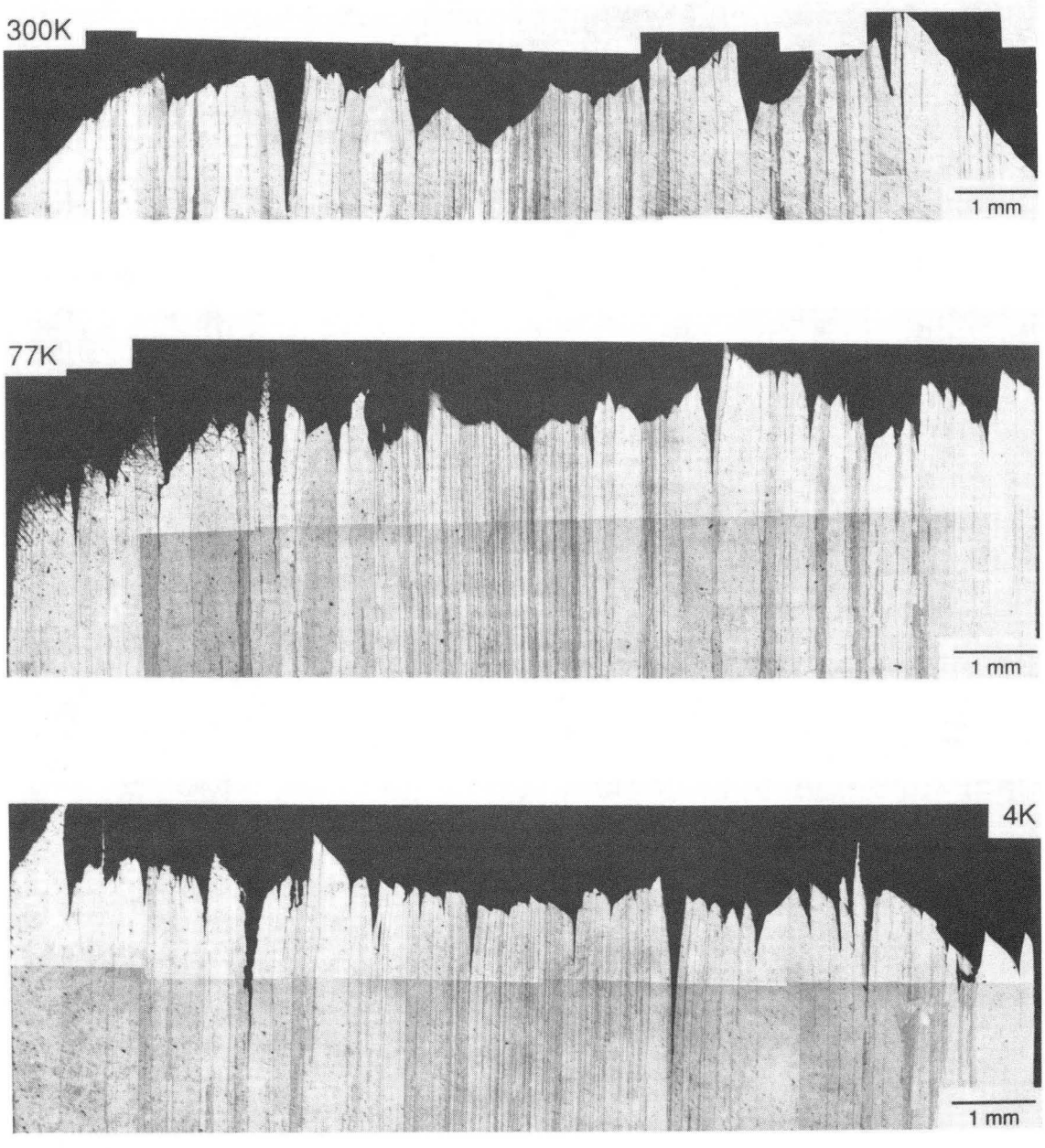

Figure 58: Optical micrographs of the fracture profile after etching for Vintage III 2090-T81 J_{Ic} specimens tested at a) 300K, b) 77K, and c) 4K. (XBB 900-9408)

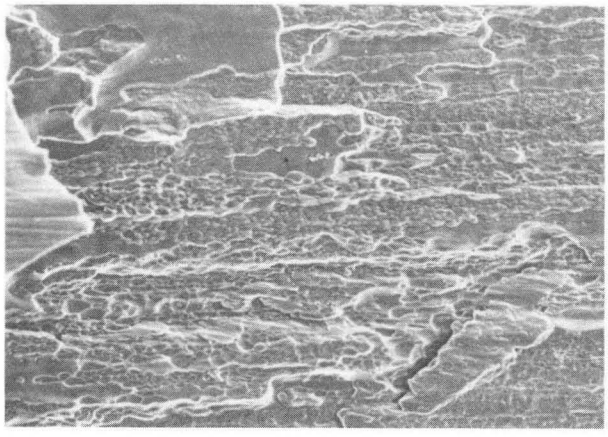

125 μm

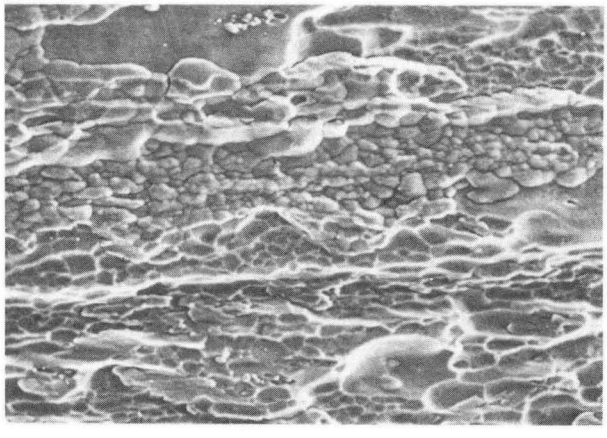

50 μm

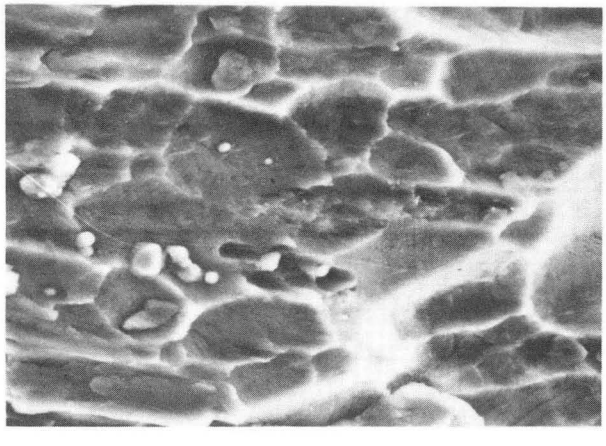

12.5 μm

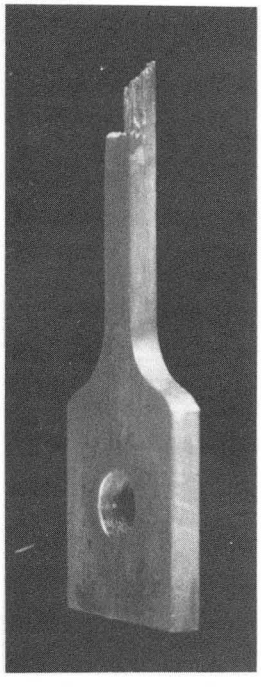

Figure 59: Scanning electron micrograph of the surface revealed by splitting in a Vintage III 2090-T81 longitudinal tensile specimen. (XBB 900-9415)

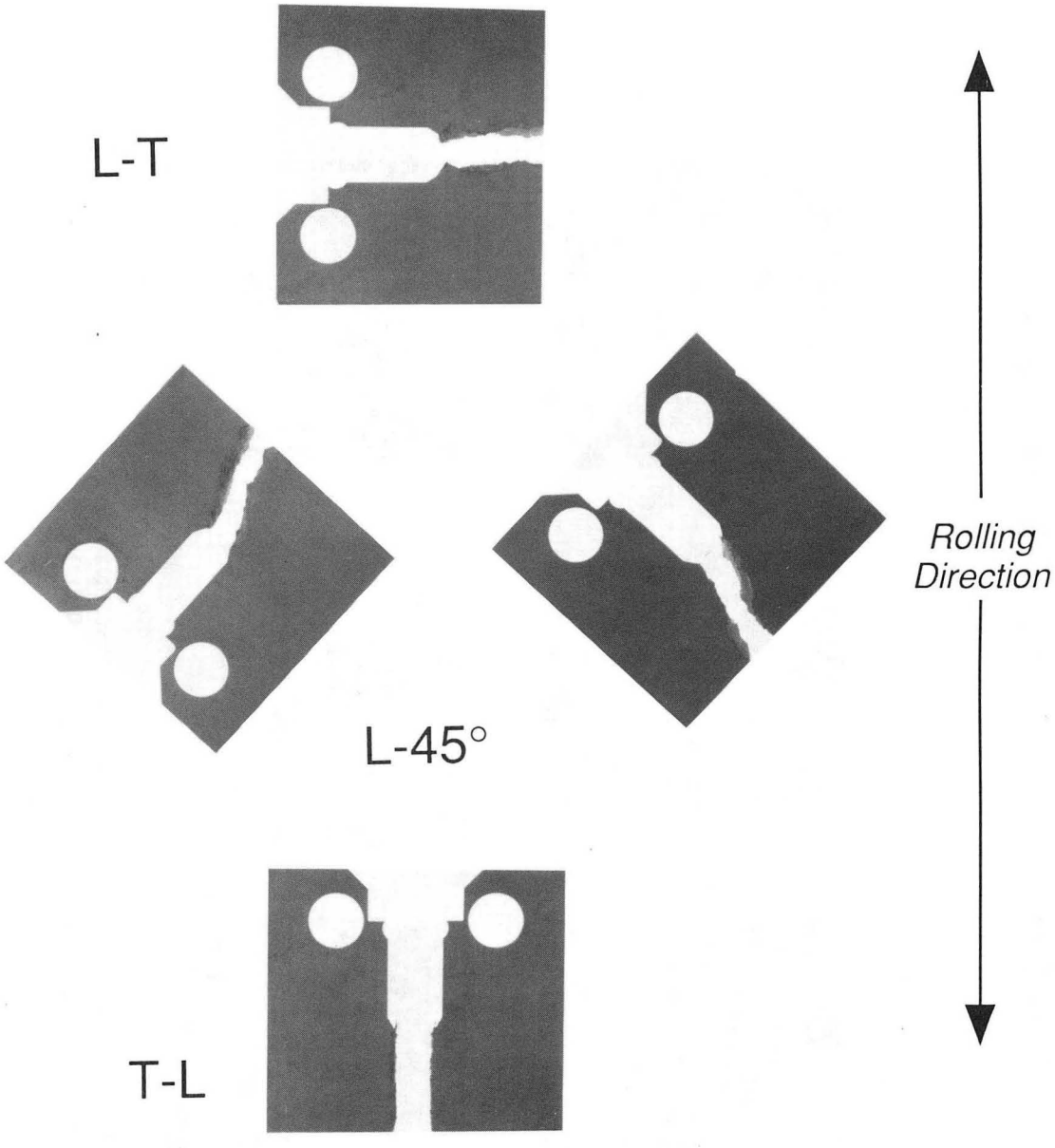

Figure 60: Optical micrograph of failed J_{Ic} specimens tested in the L-T, L-45°, and T-L orientation. (XBB 900-9799)

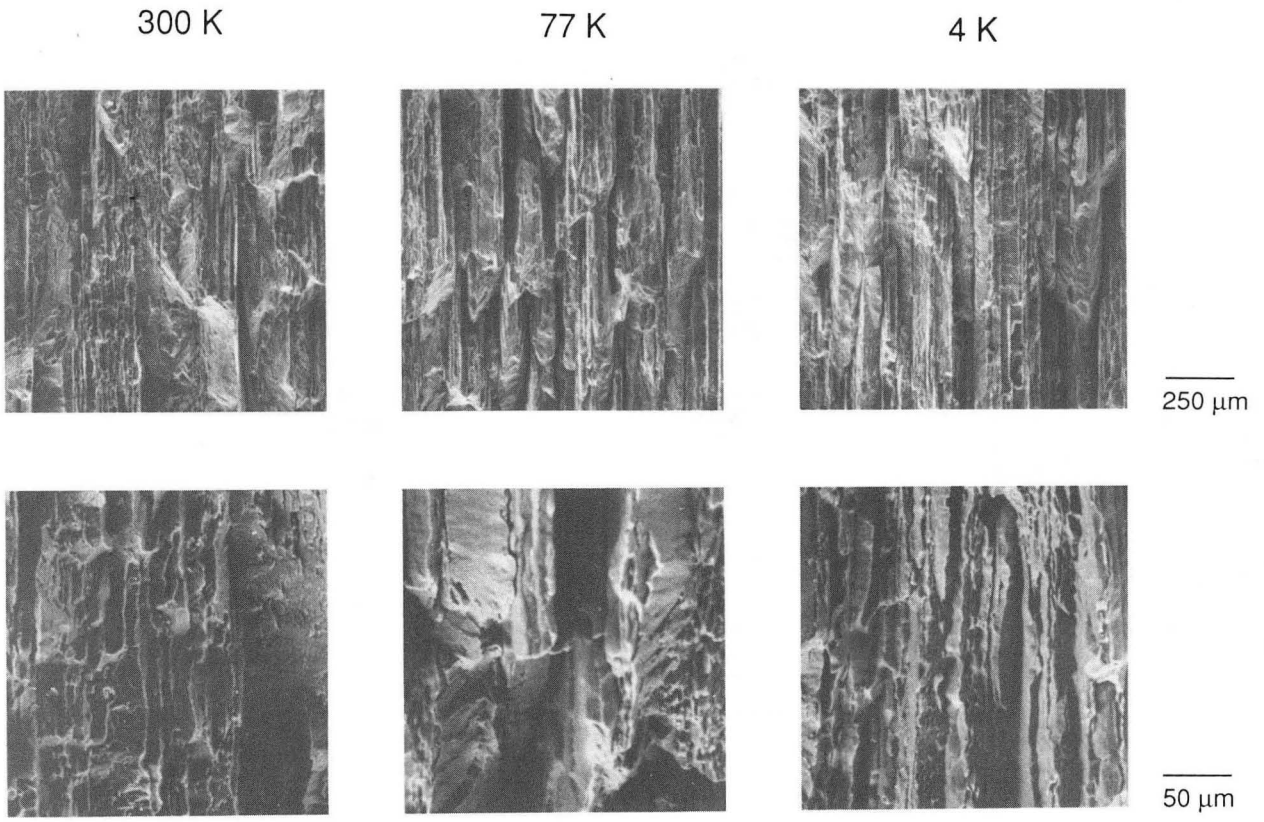

Figure 61: Scanning electron micrographs of the fracture surface at mid-thickness of Vintage III 2090-T81 L-45° J_{Ic} specimens tested at 300K, 77K, and 4K. (XBB 900-9406)

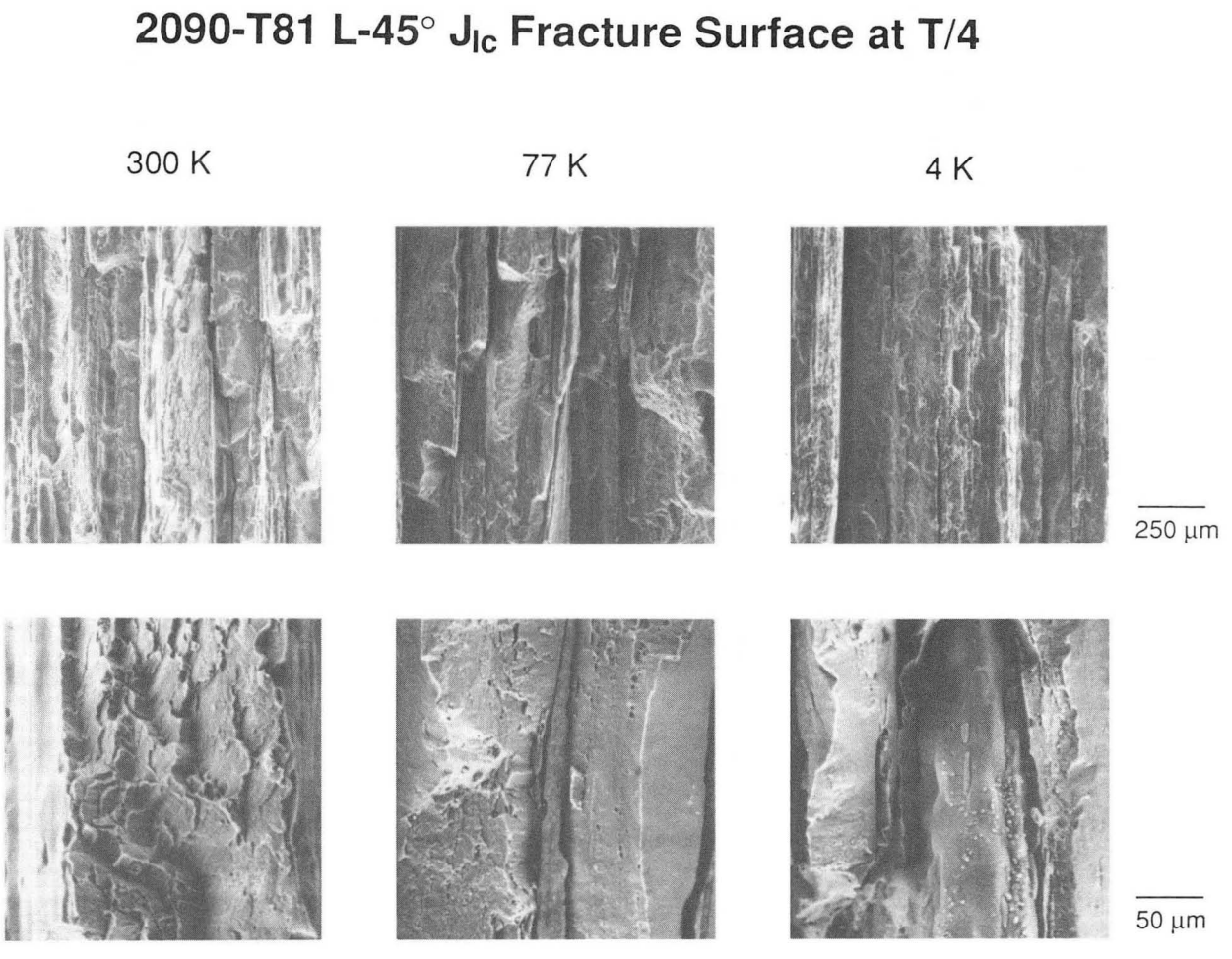

Figure 62: Scanning electron micrographs of the fracture surface at quarter-thickness of Vintage III 2090-T81 L-45° J_{Ic} specimens tested at 300K, 77K, and 4K. (XBB 900-9407)

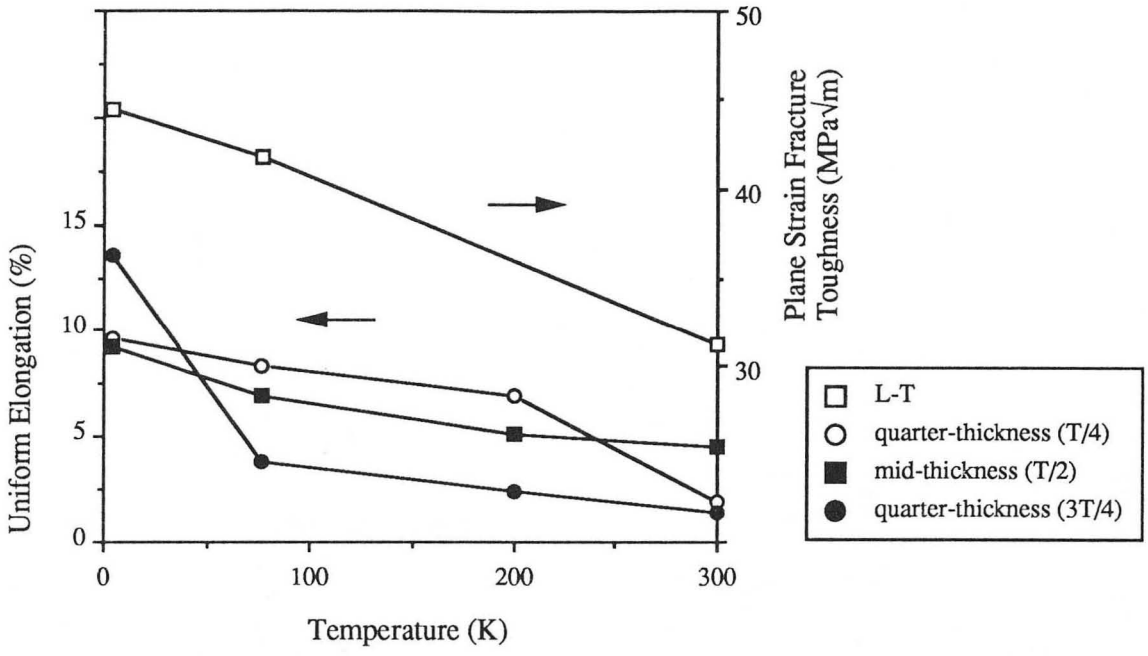

Figure 63: Comparison of the fracture toughness and uniform elongation as a function of temperature for Vintage III 2090-T81 L-T J_{Ic} specimens and longitudinal tensile specimens.

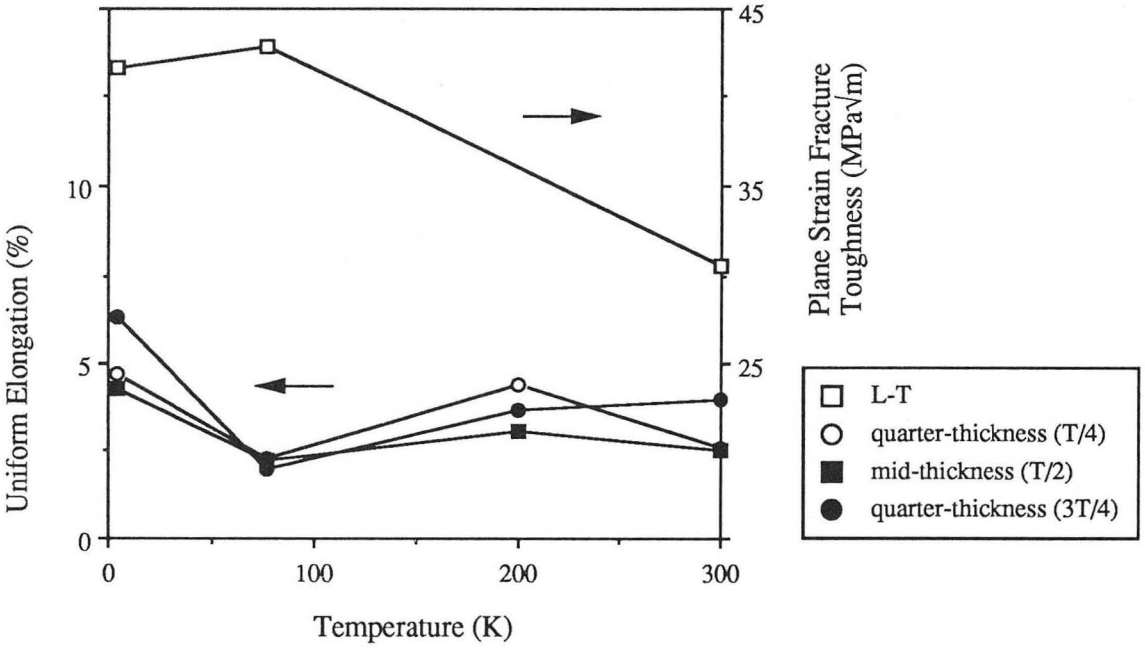

Figure 64: Comparison of the fracture toughness and uniform elongation as a function of temperature for Vintage III 2090-T81 L-45° J_{Ic} specimens and 45° tensile specimens.

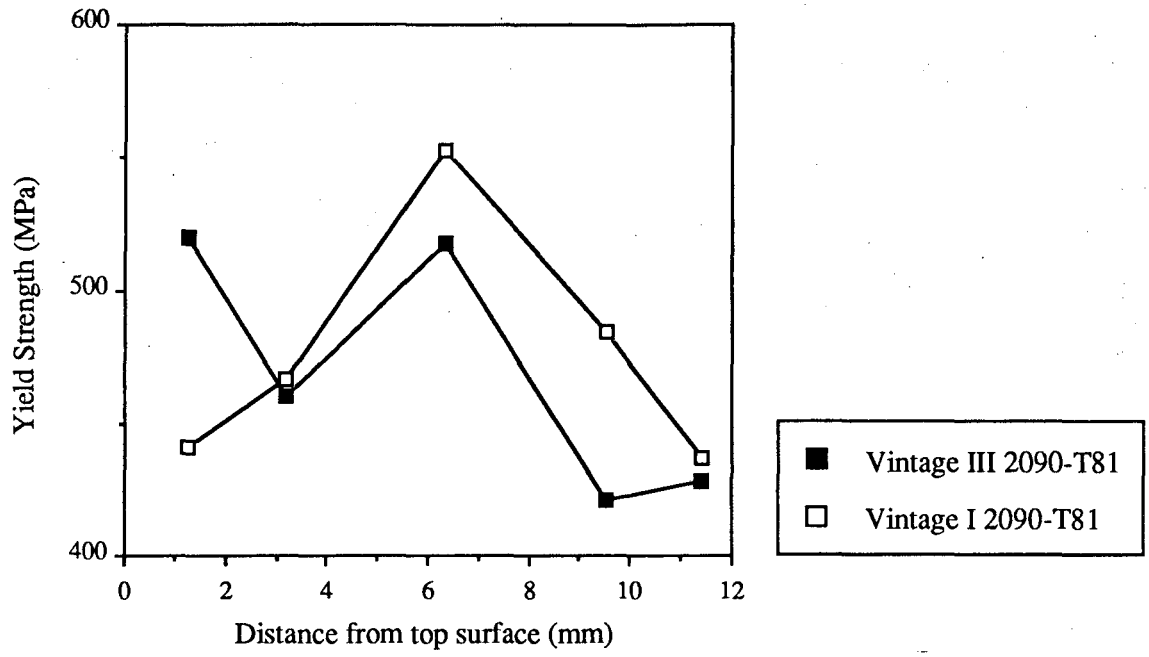

Figure 65: Comparison of the yield strength as a function of the through-thickness position for Vintage I and Vintage III 2090-T81 longitudinal tensile specimens tested at 300K.

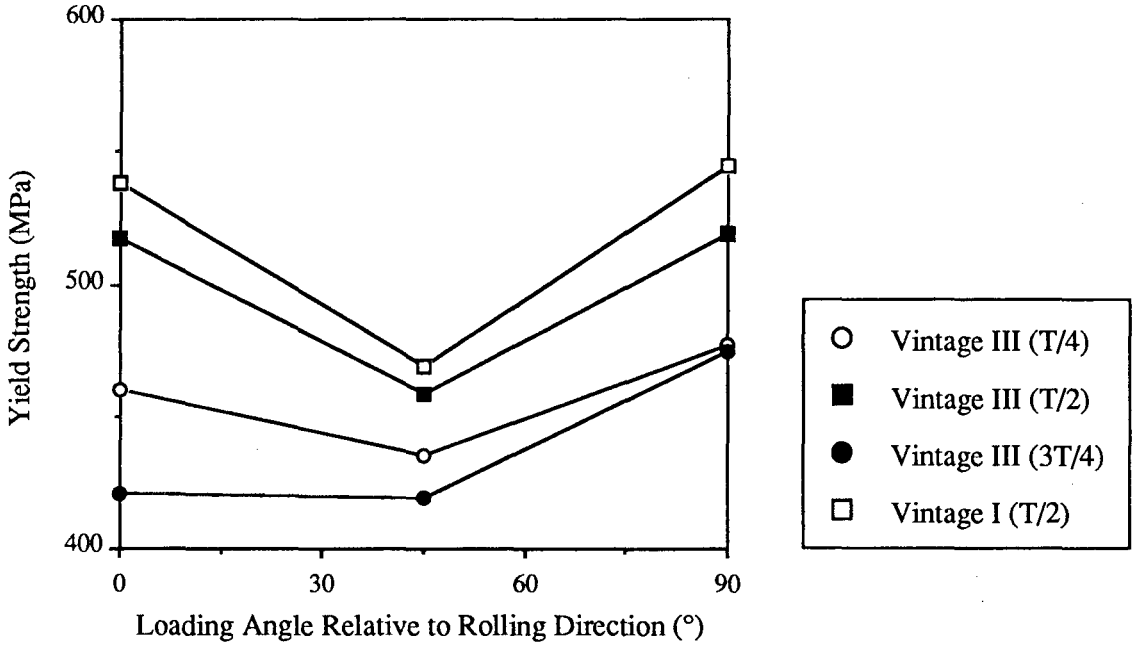

Figure 66: Comparison of the yield strength as a function of the in-plane orientation for Vintage I 2090-T81 tensile specimens taken at mid-thickness and Vintage III 2090-T81 tensile specimens taken at mid-thickness and quarter-thickness.

LAWRENCE BERKELEY LABORATORY
CENTER FOR ADVANCED MATERIALS
1 CYCLOTRON ROAD
BERKELEY, CALIFORNIA 94720